The Dissertation Committee for Dewei Xu Certifies that this is the approved version of the following dissertation:

SCALE DEPENDENCE IN FRICTION: THE TRANSITION FROM INTIMATE CONTACT TO MONOLAYER LUBRICATED CONTACT

Committee:

Kenneth M. Liechti, Supervisor

K. Ravi-Chandar, Co-Supervisor

Stelios Kyriakides

Gregory J. Rodin

Michael Marder

SCALE DEPENDENCE IN FRICTION: THE TRANSITION FROM INTIMATE CONTACT TO MONOLAYER LUBRICATED CONTACT

by

Dewei Xu, B.S.

Dissertation

Presented to the Faculty of the Graduate School of
The University of Texas at Austin
in Partial Fulfillment
of the Requirements
for the Degree of

Doctor of Philosophy

The University of Texas at Austin

December 2007

Dedication

To my wife, Mei Wu.

To my daughter, Sophie Y. Xu.

To my mother, Jiazhen Xiang.

To the memory of my father, Xinquan Xu, who died suddenly of Cerebral Apoplexy eight years ago when I was thousands of miles away from him.

Acknowledgements

The author would like to express his sincere gratitude to his advisor, Professor Kenneth M. Liechti, for his teaching, guidance and support throughout the graduate study. His profound contributions to my development, both professional and personal, are mostly appreciated. The author would like to extend his sincere appreciation especially to Dr. K. Ravi-Chandar for his guidance and support through this research. The author benefited from his advice, knowledge and experience. The author would like to thank the other members of his supervisory committee for reviewing this dissertation and the faculty of the Department of Aerospace Engineering and Engineering Mechanics.

Special thanks go to Dr. Mingji Wang, who initiated and developed the meso-scale friction tester (MFT) and Professor Lloyd Brown at the Naval Acadamy, who introduced modifications to the MFT for conducting friction experiments with electric current. The author is also grateful to Professor Lew Rabenberg in Mechanical Engineering Department and Mr. Junwei Huang, a graduate student in Physics Department, for their generous assistance in electrochemical etching/polishing.

The author would like to thank the staff and his fellow graduate students in the Department of Aerospace Engineering and Engineering Mechanics. The author cherishes the knowledge he gained from them, the help he received from them and their friendship.

Finally, the author wishes to acknowledge the financial support of the Office of Naval Research (MURI Grant # N00014-04-1-0599) and of the Department of Aerospace Engineering and Engineering Mechanics.

Dewei Xu

SCALE DEPENDENCE IN FRICTION: THE TRANSITION FROM INTIMATE CONTACT TO MONOLAYER LUBRICATED CONTACT

Publication No._____________

Dewei Xu, Ph. D.
The University of Texas at Austin, 2007

Supervisor: Kenneth M. Liechti
Co-Supervisor: Krishnaswa Ravi-Chandar

Over the years, nonwear friction with single asperity contact has been examined through experiments using the Surface Force Apparatus (SFA) and the Atomic Force Microscope (AFM). The contact radii in SFA and AFM friction experiments ranged in the order of tens of μm ($>10^{-5}$ m) and several nm ($<10^{-8}$ m), respectively. In spite of the fact that the contact radii in these experiments differ by several orders of magnitude, the data from both experiments obey Bowden and Tabor's friction law $F=\tau A$, where F is the friction force, τ is the frictional shear strength and A is the real contact area. However, there is a crucial difference between the results obtained with the two instruments. The shear strength from the SFA experiments in dry environment is in the tens of MPa, while the shear strength from the AFM measurement is several hundreds of MPa. In the intervening mesoscales, with contact radii ranging from $10^{-8}<a<10^{-5}$ m, the frictional shear strength must be dependent on contact area in order to link these two extremes. Some models based on dislocation motions have recently been developed to bridge the gap (Hurtado and Kim, 1999a; b). Hitherto, no systematic mesoscale friction experiments to bridge the shear strengths obtained from AFM and SFA have been provided. In addition, this is precisely the range in which MEMS and potential NEMS devices are expected to operate. Therefore, apart from the fundamental challenges involved in resolving the scale dependence of friction, there is a strong technological motivation for studying friction at this scale.

In the present work, this transition in shear strength is bridged using a newly-developed Mesoscale Friction Tester (MFT) over a wide range of contact radii and relative humidity levels. Since a nonwear and single asperity contact is of interest, novel procedures to fabricate tungsten probes with subnanometer (<0.3nm) surface roughness are initiated. In order to choose an appropriate contact mechanics theory in an ambient environment to obtain the true contact area, a modified Tabor parameter for JKR-DMT transition for capillary force dominant contact is employed. Results from friction experiments show that the transition in shear strength occurred over contact radii of only 20~30nm in both ambient and dry environments. It is hypothesized that shear strengths in the tens of MPa resulted from contact separated by a monolayer of interfacial molecules and shear strengths in hundreds of MPa resulted from intimate contact (no interfacial molecules inside the contact zone). It was the interfacial condition inside the contact zone that governed the transition. Furthermore, there is no continuous spectrum of shear strength, but a “quantized” behavior. A continuum analysis based on Lifshitz theory, which related the shear strength to the estimated strength of van der Waals bonds is proposed to explain the quantized shear strengths obtained from current experiments and both previous AFM and SFA friction experiments.

Table of Contents

List of Tables

List of Figures

Chapter 1 Introduction

1.1 Overview and Motivation

The science of *tribology* (friction) originated from the Greek word *tribos* (meaning rubbing) concentrates on *interacting surfaces in relative motion* or *the contact mechanics of moving interfaces* that involve energy dissipation (Dowson, 1979). Pioneers in *tribology* that one salutes are: Leonardo da Vinci (1452-1519), Guillaume Amontons (1663-1705), John Theophilius Desanguliers (1683-1744), Leonard Euler (1707-1783) and Charles-Augustin Coulomb (1736-1806). The classical Amontons and Coulomb's laws of friction are summarized as

I. The force of friction is directly proportional to the applied load (Amontons 1st law);

II. The force of friction is independent of the apparent area of contact (Amontons 2nd law);

III. Kinetic friction is independent of the sliding velocity (Coulomb's law).

In addition, Amontons laws could be easily attributed to Leonardo da Vinci since his manuscripts were hidden or lost for centuries (Dowson, 1979). Although these friction laws still apply to many engineering problems today, they were born from empirical observations and one immediately counterexample is that geckos are able to climb up vertical surfaces and even move with their heads downwards (Maderson, 1964; Autumn et al., 2002).

However, many current and potential technological applications, such as computer hard disk drives and micro/nanoelectromechanical systems (MEMS/NEMS), require an understanding of the fundamental mechanisms and detailed models of contact and friction between surfaces. Furthermore, since the advent of the surface force apparatus (SFA) (Tabor and Winterton, 1969; Israelachvili and Tabor, 1972), the interfacial force microscope (IFM) (Joyce and Houston, 1991), the atomic force microscope (AFM) (Binnig et al., 1986) and its variant, the mesoscale friction tester (MFT) (Wang et al., 2007), the shear-force microscope (Betzig et al., 1992) and etc., interpreting data from these apparati also requires such mechanisms and detailed models.

The adhesion origin of friction was first proposed by Desanguliers and later reconsidered by Prandtl and Tomlinson (Dowson, 1979). The correlation between friction and adhesion - that the stronger the adhesion, the larger the friction force - is clearly shown in recent work where friction forces were able to distinguish different chemical groups (Overney et al., 1992; Frisbie et al., 1994; Green et al., 1995; Noy et al., 1997; Burns et al., 1999; Kim and Houston, 2000; Kim et al., 2001; Noy, 2006). Furthermore, the physical contact condition is even not necessary for the appearance of friction originating from long range of adhesive interactions (Dorofeyev et al., 1999; Stipe et al., 2001; Kuehn et al., 2006). Perhaps the strongest connection between friction and adhesion comes from experiments and simulations of the contact of an adsorbed monolayer or bilayer thin film sliding on a metal substrate (Krim et al., 1991; Cieplak et al., 1994; Daly and Krim, 1996; Tomassone et al., 1997). Based on the ingenious work dealing with metal-on-metal sliding, Bowden and Tabor proposed that the friction force (Bowden and Tabor, 1950)

$$F = \tau A, \tag{1.1}$$

where τ is the shear strength and A is the true contact area, is more appropriate than the Amonton-Coulomb friction law. The true contact area is the continuum representation of the number of atoms involved in the adhesive or cohesive interactions between two sliding surfaces. Eq. (1.1) is considered to be the cornerstone of most current friction theories (Hurtado and Kim, 1999a). In addition, the results from molecular dynamics simulations suggest that τ weakly depends on the normal pressure (He et al., 1999; He and Robbins, 2001). As a matter of fact, this assumption hints that the general rule describing friction forces should not have been regarded differently from the one for bulk materials since a similar mechanism is involved. The “evil” interface should be blamed for the complexity involved in modeling friction since the continuum descriptions or mechanics of contact and friction are based on the fundamental progress of surface and interface science. However, compared to the two extremes: the area of bulk materials and at the molecular, atomic and subatomic level, the surface and interface science after much neglect over years is called the “twilight zone” (Drew, 1999) or “world of neglected dimensions" by Wolfgang Ostwald in 1915. Furthermore, tribology or friction faces a *moving real interface*; moving itself may mean beyond statics or equilibrium (maybe accompanied with wear) and any real interface with asperities and inhomogeneities is much worse than the ideal interface that surface and interface science deals with. As a result, it is extremely difficult to gain good, well-characterized systems which give consistent and reproducible results in the hands of different investigators and so far there is no quantity to describe friction at the macroscopic level better than the friction coefficient (the ratio of friction force to normal force). The asperities and the resulting wear really plague fundamental studies of friction. Thus, this may be the reason why " mainstream scientists seemed to have no interest in the topic" (Krim, 1996) since a universal solution is not likely and friction itself is called "one of the most common, yet least understood physical phenomena" (Carpick and Salmeron, 1997).

Nevertheless, the advent of novel apparati, such as, SFA, AFM, IFM, etc. provides an opportunity to study the quasi-ideal case of nonwear and single asperity contact. The introduction of the quartz-crystal microbalance (QCM) enabled the study of friction at the atomic scale (Krim and Widom, 1988; Watts et al., 1990). Since then Bowden and Tabor's assumption $F = \tau A$ has been examined extensively using the surface force apparatus (SFA) (Israelachvili et al., 1988; Homola et al., 1989; Homola et al., 1990) and the atomic force microscopy (AFM) (Carpick et al., 1996; Meyer et al., 1996; Carpick et al., 1997; Lantz et al., 1997; Enachescu et al., 1998). There are two review papers (Carpick and Salmeron, 1997; Gnecco et al., 2001) on AFM friction experiments. However, there is a crucial difference between the shear strengths obtained by these two instruments. A shear strength of about 25MPa in dry environment with contact radii on the order of tens of micrometers was obtained in SFA experiments when two mica surfaces were separated by a 0.3-0.5Å layer of physisorbed interfacial molecules (Homola et al., 1989; Homola et al., 1990). On the other hand, shear strengths obtained from AFM experiments range over several hundreds of MPa with contact radii of a few to just more than ten nanometers irrespective of environments such as UHV, dry N_2 and ambient. In the intervening mesoscales, with contact radii ranging from $10^{-8} < a < 10^{-5}$ m, the frictional stress must be dependent on contact area in order to link these two extremes. Some models based on dislocation motions have recently been developed to bridge the gap (Hurtado and Kim, 1999a; b). However, the authors assumed that the shear strength of 25MPa resulted from an intimate contact (no interfacial molecules between two sliding mica surfaces) and regarded it as the Peierls stress for mica. Furthermore, the role of the dislocation movement at the interface in friction remains an open issue. As a result, such models may more appropriately apply to the scale dependence for bulk material. Hitherto no systematic friction experiments (in mesoscale) to bridge the shear strengths obtained from AFM and SFA have been provided. In addition, this is precisely the range in which MEMS and potential NEMS devices are expected to operate. Therefore, apart from the fundamental challenges involved in resolving the scale dependence of friction, there is a strong technological motivation for studying friction at this scale.

On the other hand, contact mechanics as a " brother" of friction combining continuum mechanics and surface physics studies the contact area, the relative approaching displacement and the relationship between the pull-off force and the adhesive energy. Compared to friction, as mentioned at the beginning, *contact mechanics of moving interfaces*, contact mechanics which only concentrates on static interfaces is nevertheless mature and well-established.

Hertz (Hertz, 1882) established his famous theory of contact in 1882 by assuming a continuous pressure distribution for non-adhesive contact between two surfaces. Adhesive interactions between the surfaces were brought into consideration when Johnson et al. (Johnson et al., 1971) in 1971 proposed their now-famous model (JKR) that brings about a balance between elastic energy, potential energy and surface energy. This model was followed by Derjaguin et al. (Derjaguin et al., 1975) (DMT) who assumed that molecular force interactions exist outside the contact zone (subsequently corrected in (Müller et al., 1983a; Pashley, 1984)). Tabor (Tabor, 1977) defined a dimensionless parameter μ_T representing the ratio between the gap outside the contact zone and the equilibrium distance between atoms. This parameter established the range of applicability of the two models and suggested that interactions within and outside the contact zone needed to be accounted for. Müller et al. (Müller et al., 1980; 1983b) solved this problem numerically by using a Lennard-Jones-type potential, thereby demonstrating a continuous transition from DMT to JKR, as the Tabor parameter μ_T increased. Maugis

(Maugis, 1992) provided a semi-analytical solution to the contact problem with interactions inside and outside the contact zone using the Dugdale approximation and showed the transition from DMT to JKR behavior to be two opposite ends of a continuous spectrum based on a parameter λ (the Maugis parameter), which is equivalent to the Tabor parameter ($\lambda = 1.16\mu_T$). Since then, an alternative with simple algebraic equations and convenient extension to viscoelastic contact has been developed by Greenwood and Johnson (Greenwood and Johnson, 1998). Barthel (Barthel, 1998) pointed out that the transition from DMT to JKR is quite insensitive to the nature of the interaction potential. A more complicated numerical solution (Greenwood, 1997) was repeated based on Müller's work. Recently, an adhesion map was generated by Johnson and Greenwood (Johnson and Greenwood, 1997) based on the Maugis model: if λ or $\mu_T > 5$, the JKR analysis becomes appropriate because both numerical and the Maugis calculations become ill-conditioned; when λ or $\mu_T < 0.1$, the DMT model should be applicable for simplicity; in the intermediate range the Maugis model has to be applied. However, when μ_T is very small (~0.02), the DMT model cannot be recovered from the solution given in (Johnson and Greenwood, 1997) and the Bradley model (Bradley, 1932) applies. Hughes and White developed solutions for "soft" contact (Hughes and White, 1979) when the surfaces distorted due to surface interactions without actually making contact. Bounds on the surface displacements were developed for a wide range of attractive and repulsive interactions. The Hertz solution was recovered for strong short range interactions. Barthel (Barthel, 1998) suggested that a third axis in the adhesion map is necessary to separate this soft contact problem from the Hertz regime. The models discussed so far did not include the effect of friction during contact. This has been discussed in more detail in (Johnson, 1997; Kim et al., 1998; Yao and Gao, 2006) where friction and adhesion effects were combined.

The well-established contact mechanics models incorporating adhesive interactions as discussed above are based on solid-solid adhesion where the two surfaces are in true molecular or intimate contact. The resulting van der Waals interaction can be represented by a Lennard-Jones potential. Ideally this situation exists in vacuum. Such conditions are not realized in applications where two hydrophilic surfaces are in contact in a humid environment; then the capillary force resulting from the Laplace pressure in the liquid annulus that forms as a result of capillary condensation or diffusion from surrounding adsorbed liquid on the surface (Zimon, 1982; Christenson, 1985; Israelachvili and McGuiggan, 1988; Israelachvili, 1992a; Scherge and Gorb, 2001) will dominate. The adhesive contact models of JKR, DMT, Maugis are not sensitive to the origin or mechanism of the adhesive interactions but only to their representation. However, the length scale where adhesive interactions appear is certainly dependent on the origin of the adhesion. Capillary forces are long range forces with a characteristic length given by the Kelvin radius, while solid-solid adhesion is a shorter range interaction with characteristic length given by the equilibrium interatomic distance. This was recognized by Fogden and White (Fogden and White, 1990) and Maugis and Gauthier-Manuel (Maugis and Gauthiermanuel, 1994) who introduced parameters that can be viewed as a modified Tabor parameter (Xu et al., 2007a) in the sense that they still represent the competition between the gap outside the contact zone and the characteristic length of the interactions between the surfaces.

1.2 Objective and Organization

The purpose of the present work is to study the transition in shear strengths from several hundreds of MPa obtained from AFM friction experiments to several tens of MPa obtained from SFA experiments. In addition, it is expected that during this study of scale dependence, the mechanism for the transition could be revealed and a quantitative analysis to predict the shear strengths could be developed.

This transition is bridged using the newly-developed Mesoscale Friction Tester (MFT) over a wide range of contact radii in both an ambient environment and a dry environment. In the following, the MFT apparatus and its calibration and novel procedures to fabricate ultrasmooth (RMS <0.3nm) probes which are crucial to form single asperity contacts with a wide range of radii are introduced in Chapter 2; contact mechanics theories and their selections using the classical and modified Tabor parameters are summarized in Chapter 3; the details of the friction experiments, results and analysis are given in detail in Chapter 4; Chapter 5 presents a few results from friction experiments with electric current.

Chapter 2 Experimental Techniques

This chapter first introduces the MFT apparatus and then describes the calibration process. Finally, novel procedures for fabricating ultrasmooth (RMS <0.3nm) probes with a wide range of radii are proposed.

2.1 MFT Apparatus

The MFT apparatus is essentially a scale-up of an optical-beam-deflection atomic, friction or lateral force microscope (AFM, FFM or LFM) (Meyer and Amer, 1988; Marti et al., 1990; Meyer and Amer, 1990) where the normal force and friction force are measured independently and simultaneously. The MFT apparatus (Fig. 2.1a) and its operation have been described in detail by Wang et al. (Wang et al., 2007). It consists of a sensor cantilever beam, laser diode, two-dimensional, position-sensitive detector (PSD), and a piezo XYZ positioning and scanning stage. All these components are mounted (Fig. 2.1b) on the MFT base. A rotation stage underneath is used to adjust the scanning direction and ensure its perpendicularity to the axis of sensor beam. The whole device is mounted on a vibration isolated table to minimize ground vibration and surrounded by an enclosure for environmental control. A thermo-hygrometer is installed inside the enclosure to monitor the humidity and temperature. In the experiments reported here, the ambient environment was monitored and found to be constant for the duration of the experiment. The operation of the device is very similar to the AFM but with larger sensor beams, which are made of steel shim stock and changeable probe tips. The probe is glued on the sensor beam and there is potentially a lot of choice in probe material and dimensions. The length of the probe may be up to 1/4~1/5 of the length of the sensor beam and hence provides comparable resolution in measuring friction and normal forces; in contrast, in the AFM, the resolution of the friction force is usually two orders of magnitude less than that of the normal force. By varying the thickness of the sensor beams, forces ranging from several nN to mN can be measured.

2.2 Calibration

In an optical-type AFM, small angular deflections of the beam resulting from the normal and friction forces sensed at the probe tip. These deflections are magnified by a long optical-beam path to generate considerable displacements upon a position sensitive detector (PSD), which transforms such detected displacements to digitized output voltages. It can be seen that the conversion between the forces exerted on the probe tip to the output signals is determined by two independent stages. The first is the relationship between angular deflections of the sensor beam and the sensed forces, which is prescribed by the bending and torsional stiffnesses of the sensor beam. There exist numerous contributions addressing the calibration of the bending and torsional spring constants of cantilever sensor beams (Cleveland et al., 1993; Ogletree et al., 1996; Sader et al., 1999; Cain et al., 2000; Green et al., 2004). Since rectangular cantilever sensor beams were used in this study, the normal and torsional stiffnesses are readily determined.

The second stage is the magnification process through long optical-path from small angular deflections to measured displacements on PSD, which is a geometrical response of the apparatus regardless of the sensor beam being used. In this stage, the measured displacement signals from PSD are determined by the product of the optical-beam path and the effective angles which are generally consider to be twice the true angular deflections resulting from normal and friction forces in AFM community (Marti et al., 1990). For the normal force shown in Fig. 2.2a, the factor 2 is obvious (Marti et al., 1990), i.e.,

$$V_{PSD} = 2\theta \cdot D + \delta \tag{2.1}$$

where, V_{PSD} is the magnified vertical displacement on the PSD, θ is the true angular deflection resulting from the normal force, δ is the vertical deflection at the laser reflection spot of the senor beam and D is the optical path from the reflection spot on the sensor beam to the PSD. For the MFT, the contribution from δ to V_{PSD} is less than 2%. However, the relationship between the effective twisted angle and the true twisted angle resulting from the friction force is subtle (Fig. 2.2b) and it can be shown that

$$U_{PSD} = 2\cos\alpha \cdot \varphi \cdot D \tag{2.2}$$

where, U_{PSD} is the magnified horizontal displacement on the PSD, α is the incident angle of the laser beam and φ is the true twisting angle resulting from the friction force. If α is small, this modification is negligible. For the MFT, $\alpha = 45°$ and the error is up to 30%. Figure 2.3 shows the variation of $U_{PSD} / 2D\cos\alpha$ with φ from two calibration processes and the resulting slope is 0.99. It can be also shown that the cross-talk between the normal and lateral deflections appear as second order corrections with respect to the normal or lateral angular deflections themselves.

The system was calibrated directly by an analytical balance (Denver Instruments PI-225D) with 0.01mg (100nN) resolution. A “Z” shaped wire, which enables application of a torque through a load in vertical direction, was used to calibrate the torsional response of the cantilever beam. One end of the wire was glued on the beam with the plane of the wire perpendicular to the axis of the cantilever beam. The calibration was done by sticking a small double-side adhesive tape to the free end of “Z” shaped wire and dipping this end into a reservoir of tungsten balls with a diameter of approximately 100μm placed on the balance at various depths. Consequently the torque exerted on the cantilever is the product of the length of the wire and the lost weight on the balance. It was found that the difference between the torsional spring constants resulting from this direct calibration and the nominal torsion spring constant is less than 5%.

However, the consistency of the calibrated normal spring constant with the nominal normal constant depends on the probe length. The shorter the probe, the higher the degree of consistency. This effect is caused by the axial friction force that accompanies the normal force. A schematic of the assembly of the cantilever beam and the probe is shown in Fig. 2.4a. The rotation of the free end of the sensor beam due to the normal load N is

$$\theta_N = \frac{NL^2}{2EI} . \tag{2.3}$$

The rotation of the free end of the sensor beam due to the resulting axial friction force F_a between the probe tip and the surface is

$$\theta_F = \frac{ML}{EI} = \frac{F_a cL}{EI} = \mu_s \frac{NcL}{EI} , \tag{2.4}$$

where c is the probe length and μ_s is the coefficient of static friction. The total rotation of the sensor beam is

$$\theta = \theta_N - \theta_F = (\frac{L}{2} - \mu_s c)\frac{NL}{EI}, \tag{2.5}$$

which accounts for the fact the rotations produced by N and F_a oppose one another. The displacement on the PSD resulting from θ_N in the absence of friction is

$$V_{PSD} = 2\theta_N \cdot D. \tag{2.6}$$

In the presence of friction, the displacement on the PSD is

$$V_{PSD}^{'} = \alpha(\theta_N - \theta_M). \tag{2.7}$$

If the force calibration factors for non zero and zero friction cases are $C = N / V_{PSD}$ and $C_N = N / V_{PSD}^{'}$, respectively, their ratio is

$$\frac{C}{C_N} = \frac{L/2}{L/2 - \mu_s c} = \frac{1}{1 - 2\mu_s c / L}. \tag{2.8}$$

Figure 2.4b shows the variation of C / C_N with c / L from a series of calculations with three curves corresponding to $\mu_s = 0.3$, 0.45 and 0.6, respectively. Each datum shown in Fig. 2.4b was the average of three calibrated values. Both Eq. (2.8) and the data indicate that the probe length has an effect on the calibration. The data was closest to the predictions for $\mu_s = 0.45$, but there was considerable scatter, probably due to variations in μ_s. Since μ_s is unknown and may be a function of material pairs, load levels, the length of probe, etc., a direct calibration *in situ* is necessary for accurate determinations of the normal spring constant of the assembly of the sensor beam and probe. As a matter of fact, this phenomenon was observed in the surface force apparatus (SFA) and hence nontilting cantilever beams were used to avoid the axial friction force (Christenson, 1988).

For comparisons with existing literature, effective normal spring constants (k_{normal}) and lateral spring constants ($k_{lateral}$) of the assemblies used in this study of a sensor beam and a probe whose length was approximately 1/5 of the beam length are listed in Table 2.1. These spring constants were obtained from direct calibrations. The length, width and thickness of #1 cantilever beam were 25.4mm, 12.7mm and 25.4μm, respectively and

19.1mm, 12.7mm and 12.7μm for the #2 cantilever beam, respectively. The lateral spring constant $k_{lateral} = k_{\phi} / c^2$ (Cain et al., 2000) (note that this equation applies where the lateral contact stiffness is much larger than the lateral spring constant), where k_{ϕ} is the torsional constant of the cantilever beam itself. Since the slopes of the normal force vs. displacement curve and the friction force vs. lateral displacement response represent k_{normal} and $k_{lateral}$, respectively, the validity of the spring constants being used can be checked from the consistency between the slope of the force vs. displacement curve and the corresponding spring constant assuming that the displacement of the piezo stage is accurate. Figures 2.5a and 2.5b display the normal force vs. vertical displacement and the friction force vs. the lateral displacement obtained from the experiments of the pull-off force and friction force measurements, respectively. In these experiments conducted in an ambient environment (RH 45%), a probe with 5.33μm radius and a type #2 cantilever beam were used. The slopes of linear portions of these curves are 0.23N/m and 1.89N/m, respectively. These are very close to 0.22N/m (k_{normal}) and 1.90N/m ($k_{lateral}$) listed in Table 2.1 for the #2-type cantilever beam.

2.3 Meso-scale Probe Tips with Sub-nanometer RMS Roughness

In this work, we were interested in single asperity contact. Tabor (Tabor, 1977) suggested that single asperity contact occurs when the adhesive force acting on the asperity deforms it by at least the RMS roughness amount. The substrate in all the experiments reported here was freshly cleaved mica, an atomically smooth surface. AFM experiments on mica are considered to be single asperity contact due to the sharpness of the tips. The mica surfaces that are used in SFA experiments are also considered to provide single asperity contact. In the following, we propose novel procedures to fabricate electrochemically etched tungsten probes that were almost as smooth over a wide range of radii.

Surface smoothness of probe tips is critical for applications such as measuring the surface tension of various liquids, oscillatory hydration forces and interfacial shear strengths from friction experiments. In this chapter we establish conditions for fabricating tips with smooth surfaces by controlling the electrochemical polishing process throughout the tip evolution rather than following current practice of producing tips by the drop-off method. Polishing is conducted under constant voltage, with the wire immersed below the nominal air/electrolyte interface by no more than one half of the wire diameter and selecting the final current level. This process provides tip radii ranging from approximately 100nm to 5µm for a tungsten wire with a 0.2mm diameter. Alternatively the wire can be placed above the nominal air/electrolyte interface but within the meniscus until the current drops to zero. In this case the range of radii is 5µm to 50µm. In both cases, AFM scans of these tips show that the surface RMS roughness is about 0.3nm.

2.3.1 Introduction

Electrochemical etching/polishing is widely used to prepare specimens for transmission electron microscopy (TEM) (Hirsch et al., 1965), make sharp tips for field ion microscopy (FIM) (Muller and Tsong, 1969) as specimen tips and for other kinds of electron microscopes as electron sources. Since the introduction of scanning tunneling microscopy (STM) (Binning et al., 1982) and atomic force microscopy (AFM) (Binnig et al., 1986), efforts to make tips as sharp as possible have intensified where the drop-off method and its variants are most widely used (Bryant et al., 1987; Chen et al., 1989; Ibe et al., 1990; Melmed, 1991; Fotino, 1992; 1993; Bourque and Leblanc, 1995; Zhang and Ivey, 1996; Liu et al., 1997; Kar et al., 2000; Sun et al., 2002). However, very smooth tips with a wide range of radii are necessary for many applications. The AFM has been used to determine the surface tension of various types of liquids (Malotky and Chaudhury, 2001; Jones et al., 2002; Drelich et al., 2004). Surface roughness is one of several factors that hinder consistent and reproducible measurements. Furthermore, oscillatory hydration forces can only be observed and studied between two smooth and rigid surfaces (Israelachvili and Pashley, 1983; Israelachvili and McGuiggan, 1988; Israelachvili and Wennerstrom, 1996). In nano and meso-scale friction experiments (Homola et al., 1989; Homola et al., 1990; Carpick et al., 1996; Lantz et al., 1997; Wang et al., 2007), probes with smooth surfaces are required in order to obtain interfacial shear strengths. The shear strength is determined using Bowden and Tabor's assumption (Bowden and Tabor, 1950) on the friction force $f = \tau A$. In order to evaluate the true contact area, an appropriate contact mechanics model has to be used assuming single asperity contact, which requires two very smooth surfaces. Furthermore, in order to explore the two orders of magnitude difference in values of interfacial shear strengths obtained from experiments using SFA (Homola et al., 1989; Homola et al., 1990) and AFM (Carpick et al., 1996; Lantz et al., 1997), multiscale tips with a wide range of radii (say hundreds of nm to hundreds of μm) have to be used. However, the widely used drop-off method based on capillarity for making tips as sharp as possible cannot simultaneously provide tips with both smooth surfaces and a wide range of radii.

In the following, we present a method for producing smooth probe tips with a wide range of radii. The background for electrochemical etching/polishing, such as, electrochemistry, mechanisms of electrochemical etching and polishing and capillarity at the nominal air/electrolyte interface is first reviewed in Section 2.3.2. This is followed in Section 2.3.3 by a description of procedures for maintaining electrochemical polishing throughout the tip evolution. Finally it is shown, by analyzing images of the topography of the apexes of tips scanned by AFM, that the procedures developed here result in tips with RMS surface roughness values up to 0.3nm. The following discussion is exclusive to the electrochemical etching/polishing of tungsten (W) since it has been widely and thoroughly studied and used in practice.

2.3.2 Background for the Electrochemical Etching/Polishing

Electrochemical etching/polishing is essentially a result of the anodic dissolution of tungsten in an aqueous electrolyte. In a typical electrochemical etching/polishing cell (dc etch) (Fig. 2.6a) the cathode is usually selected to be a loop or a cylinder made of inert material. The tungsten wire as the anode is placed in the center of the loop (cathode). The anode is usually fixed to a vertical stage in order to adjust the immersed depth of the wire. The electrolyte may be NaOH or KOH. In the following, the electrochemistry associated with etching/polishing, etching and polishing mechanisms and capillarity at the nominal air/electrolyte interface are reviewed.

2.3.2.1 Electrochemistry

A meniscus forms around the wire once it is placed into the electrolyte as shown schematically in Fig. 2.6b. Etching occurs at the surface of the wire (anode) inside the meniscus and below the nominal air/electrolyte interface when the potential is applied. The electrochemical reactions can be expressed as (Ibe et al., 1990)

cathode:

$$6H_2O+6e^- \rightarrow 3H_2(g)+6OH^- \qquad SRP=-2.48V, \tag{2.9a}$$

anode:

$$W(s)+8OH^- \rightarrow WO_4^{2-}+4H_2O+6e^- \qquad SOP=+1.05V \tag{2.9b}$$

and overall:

$$W(s)+2OH^-+2H_2O \rightarrow WO_4^{2-}+3H_2(g) \quad E^0=-1.43V, \tag{2.9c}$$

where, E^0 is the standard electrode potential given by the sum of the standard reduction potential (SRP) and the standard oxidation potential (SOP) for tungsten. Ideally these non spontaneous chemical reactions will be initiated when the applied potential exceeds 1.43V. However in practice the potential required to initiate electrochemical reactions is usually higher than the one calculated from the standard electrode potential, particularly when a gas (such as hydrogen) is involved as a reaction product because of electrochemical polarization (Ibe et al., 1990).

However the reaction mechanisms are more complicated than those given in Equations 2.9. Kelsey (Kelsey, 1977) proposed that reaction mechanisms from the oxidation of tungsten to tungsten trioxide, the most thermodynamically stable oxide, are electrochemical and the following dissolution of the trioxide to form the soluble tungstate $\left(WO_4^{2-}\right)$ anion is non electrochemical:

$$WO_3(s)+OH^- \rightarrow HWO_4^-(aq) \tag{2.10a}$$

$$HWO_4^-(aq)+OH^- \rightarrow WO_4^{2-}(aq)+H_2O. \tag{2.10b}$$

Since the initial surface of tungsten wire will be covered by a thin layer of trioxide (Warren et al., 1996; Lassner and Schubert, 1999) and the dissolution of these trioxides are non electrochemical, oxygen is instead produced at the anode at the beginning of the etching given by the reaction

$$4OH^- \rightarrow O_2(g)+4e^- + 2H_2O \tag{2.11}$$

This is why bubbles at the tungsten anode in the first few seconds have been reported in most direct-current (dc) etches (Edwards and Pearce, 1978; Kar et al., 2000). However for an alternating-current (ac) etch, vigorous bubbling around the tungsten wire has been observed throughout the whole etching process (Edwards and Pearce, 1978; Fotino, 1992;

1993). Most of this bubbling results from hydrogen given by Equation 2.9a. For an ac etch the cathode is also consumed if it is not inert.

2.3.2.2 Electrochemical Etching and Polishing

The two electrochemical processes, electrochemical etching and polishing, are distinctly different from one another. A typical current-voltage (I-V) curve for the electrochemical etching/polishing process is shown schematically in Fig. 2.7 (Tegart, 1956; Hirsch et al., 1965; Ibe et al., 1990). Etching occurs in the lower current regime when the applied potential $V < V_E$, polishing in the middle plateau range when $V_E < V < V_P$ and both etching and polishing accompanied by gas evolution and resultant pitting when $V > V_P$. In the initial etching stage the material is removed in a selective manner, where different etching rates result from inhomogeneities, such as crystallographic orientation, microstructure and composition (Melmed, 1991). As a result, the etching process leads to a rough topography. However polishing is insensitive to these parameters and removes material more rapidly from any asperities and uniformly if there is a smooth surface. Consequently smooth surfaces result from polishing. It was shown (Tegart, 1956) that both a thin surface film and a viscous layer play critical roles in the polishing process. This thin surface film is generally an oxide film, which homogenizes the surface topography and prevents the anode from being exposed to the electrolyte directly (if this occurs, inevitably etching results because the dissolution prefers sites with high energy, for example, grain boundaries). A viscous layer tends to stream off the anode surface and protects the anode from the electrolyte. According to the Boltzmann distribution, the concentration of counterions (hydroxide) from the anode is saturated outside this viscous layer (Crow, 1988; Israelachvili, 1992b). During steady state polishing, the thickness of the viscous layer remains constant. Thus smoothing or polishing can be accounted for qualitatively by the difference in the concentration gradient in the viscous layer over the peaks and valleys. At the peaks, the layer is thin and the concentration gradient is higher, while in the valleys, the layer is thicker and the concentration gradient is lower. As a result, preferential solution of the peaks occurs and the surface is smoothed.

For tungsten (Ibe et al., 1990; Sun et al., 2002), the surface oxide and viscous layers are composed of tungsten trioxide $\left(\mathrm{WO_3}\right)$ and tungstate ions $\left(\mathrm{WO_4}^{2-}\right)$, respectively and $V_E \approx 2 \sim 4\mathrm{V}$ and $V_P \approx 15\mathrm{V}$. Generally, the applied potential is larger than 4V, so electrochemical polishing occurs. However, for consistency with existing literature, the term electrochemical etching is still used in the following.

2.3.2.3 Capillarity at the Air/Electrolyte Interface

The meniscus (Fig. 2.6b) that forms around the anode is critical for controlling the geometry of tips produced by the electrochemical etching process. The etching rate is controlled by two diffusion processes: (i) the diffusion of hydroxide anions to the anode and (ii) the diffusion of tungstate anions away from the anode. During the etching process, there is a gradient in the hydroxide concentration in the meniscus ranging from zero at the top of the meniscus to a maximum at the bottom. At the top of the meniscus, the hydroxide anions are used up quickly and diffuse from the lower portion; at the bottom, the hydroxide anions diffuse from the bulk electrolyte which is equal to the nominal value of the concentration of the electrolyte. The tungstate anions have to diffuse away from the anode to the bulk electrolyte in order to maintain etching. These tungstate anions most likely flow downward because the saturated hydroxide layer behaves like a sheath for the viscous layer of tungstate anions and the interactions between hydroxide and tungstate anions are repulsive. Faster diffusion leads to higher etching/polishing rates, so the etching rate is lowest at the surface of the anode at the top of the meniscus and highest at the bottom of the meniscus and below the nominal air/electrolyte interface. As a result, the portion of the wire below the nominal air/electrolyte interface would be etched away. However the flow of tungstate anions no longer conforms to the surface of the wire when it approaches the portion of the wire below the nominal air/electrolyte interface. This leads to the formation of a neck at the nominal air/electrolyte interface. When the weight of the lower part of the wire exceeds the tensile force that the necking area can support, it drops off, thereby simultaneously producing two sharp tips. This is the mechanism of the widely used drop-off method for producing sharp tips. If the tip is sharp enough, the maximum tip length is the height of the meniscus, which determines the aspect ratio (the ratio of the tip length to the diameter of the wire shank) of the tip.

The aspect ratio of a tip is also an important parameter: for example, tips for STM require low aspect ratios in order to minimize vibrations, while AFM tips with high aspect ratios are preferred in order to scan deep grooves/trenches. This facet of tip making has not been explored very much in the literature. However it is a key component for understanding how a wide range of tip radii can be produced.

The product of the tip radius and the aspect ratio can be shown to be constant if the shape of a tip is assumed to be composed of two segments (Fig. 2.8): a paraboloid at the sharp end and a hyperboloid from the root with a smooth transition between them. Assume that the paraboloidal and herperboloidal regions are represented by the functions $y_1 = -Ax^2 + L$ and $y_2 = C/x$, respectively, where A, L (the tip length) and C are constants. These two curves meet at $x = x_0$ and satisfy $y_1(x_0) = y_2(x_0)$ and $y_1'(x_0) = y_2'(x_0)$. Under these conditions, it is readily obtained that $L/A = 3x_0^2$. In addition, the radius of the curvature $R = 1/2A$ at the sharp end and the aspect ratio $\alpha = L/D$, where D is the diameter of the wire. Consequently $R\alpha = 3x_0^2/2D$, which is a constant for a given value of x_0. Intuitively this conclusion is true: the sharper the tip is, the longer it is. Later, data collected from many tips will confirm this relationship.

Since the meniscus primarily determines the aspect ratio and overall shape of the tip, we consider the problem of the capillary rise along the wire. The relationship between the rising height H and the radius R of the wire (Fig. 2.6b) was numerically determined by Huh and Scriven (Huh and Scriven, 1969). The dimensionless height H/a was fit to a fifth order polynomial:

$$\frac{H}{a} = 4.2543\left(\frac{R}{a}\right) - 22.505\left(\frac{R}{a}\right)^2 + 92.41\left(\frac{R}{a}\right)^3 - 206.49\left(\frac{R}{a}\right)^4 + 181.2\left(\frac{R}{a}\right)^5 \qquad (2.12)$$

for $\frac{R}{a} < 0.4$, where a is the capillary constant (Adamson, 1990) with a value of 3.85mm for an aqueous based electrolyte. In the analysis, the additional surface tension due to the electrolyte (Levin, 2000) was neglected. The diameter of most tungsten wires used ranges from 0.1mm to 0.2mm, resulting in dimensionless rising heights from 0.052 to 0.097. Thus the largest aspect ratio that can be obtained using the loop cathode is approximately

2. However, if a hollow cylinder with a small enough inside diameter is used as the cathode, a much higher meniscus results. The meniscus height inside the cylinder is determined by $H = a^2 / R_{in}$, where R_{in} is the inner radius of the cylinder cathode. Consequently tips with larger aspect ratios can be produced when a hollow cylinder cathode is used. For example, tips with aspect ratio of approximately 10 were made by Sun et al. (Sun et al., 2002).

2.3.3 Tip Etching Procedures and Experiments

The goal of this study was to fabricate probe tips with a wide range of radii and ultra smooth surfaces, at least near their apexes. All the tips were etched in the etching cell shown in Fig. 2.6a and monitored through an optical microscope with 40× magnification. Tungsten wire (anode) with a 0.2mm diameter was placed inside a platinum wire loop (cathode) with a diameter of 1cm. The etching was conducted in a 1.78M potassium hydroxide solution. The applied potential was 4V and the etching current was monitored and recorded using a computer equipped with a data acquisition system. The radii of all tips were characterized using images obtained from a scanning electron microscope (SEM).

2.3.3.1 Procedures for Producing Tips with Ultra Smooth Surfaces

The key point for making probe tips with ultra smooth surfaces (<0.3nm RMS) is that there should be no drop-off of the lower part. In other words the drop-off method cannot be used to make tips with ultra smooth surfaces. First of all, the dropping of the lower part compromises the electrochemical polishing process because the viscous tungstate layer is disturbed and the broken cross section is not covered by the thin oxide surface film. It takes time to form a steady viscous layer and the oxide surface film after the lower part has dropped. Second, due to the fracture process, the surface of the broken cross section is irregular and very rough. Third, the plastic strain in the necking area may multiply the number of dislocations, which are sources of pitting, by 4 orders of magnitude (Hull and Bacon, 2001). Figure 2.9 shows a series of tips which were obtained by terminating the etching at different times following the drop off. Figure 2.9a shows the type of tip obtained by shutting off the etching approximately 0.5s after drop off. It is clear that the tip is irregular and rough. If etching was terminated 60s after the drop-off

(Fig. 2.9b), the polishing phase has yet to begin and the resulting surface was still very rough. Figure 2.9c shows a tip with a smooth surface which was obtained by turning off the etching process 240s after the drop-off. Apparently this is the time span required for establishing the steady state thickness of the oxide surface film and the viscous tungstate layer, which gives rise to polishing.

The question then arises as to how a sharp tip can be made without drop off. Because the immersed part of the wire is surrounded by the same environment, the etching rate is the same on both its cylindrical and bottom surfaces. Thus if the immersed length is equal to the radius R of the wire, the tip will be formed naturally at one point without drop-off, as shown schematically in Figs. 2.10a and 2.10b. The transition from the surface profile in Fig. 2.10a to the one in Fig. 2.10b occurs very rapidly. According to Faraday's laws of electrolysis (Tilley, 2004), the etching current is a direct reflection of the material etched per unit time, which, in turn, is related to the total area of the surface available for etching. In other words, the history of the etching current records the evolution of the etched surface and can be used to determine when a sharp tip is formed by noting when a slope discontinuity in the current history appears. This can be seen in the typical current history shown in Fig. 2.11a where the immersed depth was 0.1mm (the radius of the wire).

There is an initial stage (not shown in Fig. 2.11a) where the current was high (up to 100mA) and oscillatory, which is due to dissolution of the natural oxide film (Eqs. 2.10 and 2.11) on the tungsten wire surface (Lassner and Schubert, 1999) and generation of oxygen bubbles. During the plateau (0 - 200s), electrochemical etching (Eq. 2.9) begins with the growth of the oxide film until it reaches its steady state thickness. This is followed by two other stages: first, the rate of current decay increases. During this time (e.g. ⓪), the tip has the shape shown in Fig. 2.11b, and schematically in Fig. 2.10a. This stage terminated when a pointed tip (Fig. 2.10b) was formed, corresponding to ① in Fig. 2.11a. Subsequently there was very little change in the shape of the tip and the variation of current slowed considerably as the tip became blunter. By turning off the etching at various current levels (e.g., ①, ②, ③, ④ and ⑤) within this second stage, ultra smooth tips with various radii were obtained.

2.3.3.2 Producing Tips with a Wide Range of Radii

The other goal of this part of study was to obtain tips with as broad a range of radii as possible. From the previous discussion, the sharpest tip (with a radius R_0) was obtained by switching off the etching at ① (Fig. 2.11a). After that, the tip became blunter until the meniscus ruptured at ⑤ and the current jumped to zero. This gave rise to the largest tip (with a radius of R_m) regardless of the immersed depth as long as the wire was initially immersed below the nominal air/electrolyte interface. The rupture of the meniscus occurs (Freud and Freud, 1930; Boucher and Kent, 1977) when the weight of the electrolyte inside the meniscus exceeds the sum of forces around the tungsten wire at the top of the meniscus resulting from surface tension. This is similar to the ring method used to determine the surface tension of liquids.

Tips with radii ranging from R_0 to R_m can be obtained by switching off the etching at various current levels as mentioned above, but tips with radii larger than R_m must be produced in a different way. To do this, recall that the product of the radius and the aspect ratio of a tip is constant (see Section 2.3.2.3). Now suppose that the end of wire is *above* the interface but still inside the meniscus as shown schematically in Fig. 2.12. The aspect ratio of the resulting tip is now affected by the immersed depth. In other words by controlling the immersed depth inside the meniscus but above the nominal air/electrolyte interface, tips with radii *larger* than R_m can be obtained. In practice, after placing the wire inside the meniscus and at different levels above the nominal air/electrolyte interface, tips with different radii are obtained until rupture of the meniscus occurs, which automatically stops the etching process.

2.3.4 Results and Discussion

In this section, we present several examples of tips obtained from the procedures described above. In addition, the smoothness of their surfaces was evaluated by AFM. The relationship between the aspect ratios and the radii of these tips is considered to verify the assumption that the product of the aspect ratio and the radius is constant.

2.3.4.1 Range of Radii for Tips

Two sets of tips were produced from the two procedures discussed above. The first set of tips was obtained by immersing the wire about 0.1mm (half the diameter) beneath the air/electrolyte interface and stopping the etching at different current levels. Their radii ranged from R_0 at the turning point to R_m at the rupture of the meniscus. Figure 2.13a shows the variation of tip radii. Before the rupture of the meniscus, larger tip radii were obtained at lower shut-off currents. This can be understood by noting that sharper tips have larger aspect ratios and correspondingly larger surface areas available for etching. The notations ①, ②, ③, ④ and ⑤ are consistent with the ones noted in the etching current history (Fig. 2.11a). Figure 2.13b shows a tip with a radius of 150nm obtained by shutting off the etching at ① (the turning point) in Fig. 2.11a. It is unlikely that tips with radii smaller than 100nm can be obtained by monitoring the current history and stopping the etching manually as was done in this study. It is possible to make sharper tips (~10nm) by designing a circuit to stop the etching more quickly by monitoring the derivative of the etching current (Chen et al., 1989). The advantage of this automatic control is that the sharper the tip is, the quicker it blunts in subsequent processing. Similar schemes are used in the drop-off method where a special circuit is designed to stop the etching as soon as possible following drop-off. In this case it is possible to produce ultrasharp tips (~10nm).

The tip became blunter after ①. Tips obtained by stopping the etching at ②, ③ and ④ are shown in Figs. 2.13c, 2.13d and 2.13e, respectively. Their corresponding radii are 1.05μm, 1.90μm and 3.61μm, respectively. The tip with a radius of 8.50μm shown in Fig. 2.13f was obtained at the rupture of the meniscus (⑤ in Fig. 2.11a). This is the maximum radius R_m obtained regardless of the immersed depth in cases where the wire is initially immersed beneath the nominal air/electrolyte interface. The value of R_m obtained in this study was 5-10μm.

The second set of tips with radii larger than R_m was obtained by placing the wire inside the meniscus but above the nominal air/electrolyte interface by a distance Δ and letting the rupture of the meniscus terminate the etching process. Figure 2.14a shows how the tip radius increases with increasing distance Δ above the nominal air/electrolyte interface. The dimensionless distance Δ / H used in the plot indicates that a large range of radii can be obtained for relatively small dimensionless distances. Figures 2.14b, 2.14c, 2.14d, and 2.14e show tips with radii of 4.57μm, 8.0μm, 19.13μm, and 47.62μm, respectively. The aspect ratio for the tip with the largest radius was about 0.2. In practice, tips with smaller aspect ratios may be undesirable because the shank of the wire may interfere with contact. This requirement sets up the upper limit of the tip radius.

In summary, for a tungsten wire with a diameter of 0.2mm, tips with radii ranging from 0.1μm to 50μm were obtained in this study.

2.3.4.2 Surface Roughness of Tips

Figure 2.9a shows the kind of tip that results from the drop-off method. Its surface is rough and irregular. However, the surfaces of the tips produced by the procedures described above, where drop-off is avoided, are very smooth. As discussed earlier, the first requirement for obtaining smooth surfaces is to prescribe a potential between 4V to 15V, which is in the electrochemical polishing plateau. In this study, the prescribed potential was maintained at 4V in order to slow down the etching process and facilitate control. However, etching at higher potentials (<15V) leads to somewhat smoother surfaces (Tegart, 1956), but not enough to offset the higher degree of control. In order to obtain a quantitative measure of the exact surface roughness, the apexes of the tips were scanned using AFM (AutoProbe M5, Park Scientific) to provide three-dimensional and two-dimensional images and profiles from line scans (Fig. 2.15) of a tip with a radius of 20μm. The AFM was operated in contact mode with a scanned area of 500nm square. The resulting RMS roughness was 0.3nm. When a freshly cleaved mica surface was used as a reference, its RMS roughness was 0.15nm. However, previous measurements of fresh cleaved mica yielded RMS roughness values of about 0.05nm (Butt et al., 1991; Frink and van Swol, 1998). Thus it is possible that other factors such as thermal noise and environmental vibration may have caused surface roughness to appear to be higher than it actually was.

When the scan size was increased, the RMS roughness of surfaces was higher. For example, the RMS roughness of the tip with a radius of 20μm for square scans of 1μm and 5μm was 1nm and 8nm, respectively, based on the assumption of a perfect paraboloid. However, increasing the scan size exposes imperfections in the assumed paraboloid and gives rise to an apparent increase in roughness. If the scan size was further increased to10μm, corrugations appeared. Thus limiting the scan size to the apex

(500nm) led to the smoothest surfaces. This may not just be an artifact of scan size. For example, the most stable surface oxide film and viscous layer occur at the apex, which results in the smoothest surface.

It was also noted that stagnant electrolytes yielded better surfaces. Thus isolating the etching cell from vibrations is required. The size of the cathode loop could also affect the stagnation of the electrolyte surrounding the anode. During etching, bubbles form at the cathode, which disturbs the electrolyte. Consequently the diameter of the cathode loop should be large enough to remove this disturbance from the anode. For example, from our practice, loop diameters of 1 to 2cm were found to be satisfactory.

2.3.4.3 Relationship between the Aspect Ratio and the Radius

As indicated earlier, the overall shape of the tip is defined by diffusion. Consequently it might be expected that the root region follows an exponential. The tip region is commonly accepted as being a paraboloid. In examining the shapes of the various tips produced in this study, it was found that the root region could be well approximated by a hyperboloid. Enforcing continuity and smoothness of the surface profile at the intersection of the parabola and hyperbola leads to the postulate that the product of the aspect ratio and the radius of a tip is constant (see Section 2.3.2.3).

The validity of this postulate was examined by considering 32 tips, 25 of which were made by immersing the wire at different depths and setting the applied potential at 4V. The remaining seven were made at an applied potential of 10~15V. Figure 2.16 shows the relationship between the dimensionless radius (R/D) and the aspect ratio (L/D). The data obtained at the potential of 4V were fit to the form $R/D = c_1/(L/D - c_2)$, thereby validating the postulate. In addition there was an offset to the aspect ratio. The reason for this offset is that there is an upper-limit for the tip radius that can be obtained using a tungsten wire whose diameter is D. Furthermore, if the tip is too short, the assumption that the tip profile is composed of a hyperboloid and a paraboloid may be invalid. For the data that was obtained at the higher potential, the product of the aspect ratio and the radius was slightly smaller. In other words for two tips with the same aspect ratio, the one obtained at the higher applied potential has a smaller radius than the one obtained at the lower applied potential. This can be explained by noting that at higher applied potentials etching rates are faster, which shortens the portion of the tip that is described by a paraboloid.

Earlier it was assumed that the maximum length of the tip was the same as the meniscus height. This assumption was considered by measuring these quantities. The height of the meniscus for the tungsten wire with a diameter of 0.2mm ranged from 0.36 to 0.39mm (measured before imposing the prescribed potential), which is very consistent with the prediction (0.374mm) in Section 2.3.2.3. However the length of a tip with a radius of 150nm (Fig. 2.13b) was 0.24mm, which is 35% smaller than the rising height of the meniscus. This discrepancy may be caused by the shielding effects of the downward flowing tungstate anions and the blunting behavior. Another possibility is electrocapillarity (Mohilner and Beck, 1979; Crow, 1988) when the etching potential is imposed, which causes a decrease of interfacial surface tension due to the electric double layer adjacent to the wire (anode) with a high concentration of anions.

Chapter 3 Contact Mechanics Theories and Selections

In order to evaluate the resulting shear strength using Eq. (1.1), the true contact area has to be determined. In SFA experiments, the contact area can be determined directly by monitoring the interference fringes over the contact area (Homola et al., 1989; Homola et al., 1990). On the other hand, it is not possible to measure the contact area directly in the AFM or MFT. Typically, the contact area in AFM experiments has been estimated indirectly by several methods. One of them is to measure the variation of electric current that was passed through the tip (Enachescu et al., 1998; 1999) during contact; however, this method requires that both the probe and substrate be conductive[1]. The measurement of total lateral stiffness was also used to determine the contact area (Carpick et al., 1997; Lantz et al., 1997), but this method applies only to situations where the lateral contact stiffness is comparable to the cantilever beam lateral stiffness. Nevertheless the prediction of contact area resulting from such direct or indirect methods is consistent with the one evaluated from an appropriate contact mechanics theory. In other words, for single asperity contact, the appropriate contact mechanics theory predicts the contact area quite accurately. In the following, three adhesive contact mechanics theories JKR, DMT and Maugis theories are first summarized. This is followed by the introduction of the modified Tabor parameter for capillary force dominant contact. Finally, some of applications of the modified Tabor parameter are discussed.

3.1 Introduction to JKR, DMT and Maugis Theories

For simplicity, the following discussion is confined to the case of adhesion between a sphere of radius *R* and a flat surface; these ideas can be generalized to other contact geometries through numerical formulations similar to that described in the simpler case.

---

[1] Note that electromagnetic forces resulting from the current may affect the contact area; other effects such as melting, arcing may occur as the current density within the contact area becomes larger (see Brown et al., 2007 for recent work in this area).

Three models – JKR, DMT and Maugis – are available for evaluating the contact interaction between two surfaces. In the JKR approximation, the distribution of the adhesion forces is reduced to a singular stress at $r = a$, the end of the contact zone, and the sum of the adhesion force outside the contact zone is zero. In the DMT approximation, both the adhesion forces acting outside the contact zone and the external load are balanced by the repulsive force inside the contact zone; the stress distribution is not continuous at $r = a$. In the Maugis model, the stress distribution is continuous across the contact zone boundary, i.e., there are stresses resulting from adhesion forces both inside and outside the contact zone. The limit of the contact zone is defined at the points where the adhesion stress is maximal. For solid-solid adhesion, it is known that these three models are neither exclusive nor competitive, but apply over overlapping ranges according to the non-dimensional parameter defined by Tabor (Tabor, 1977). A brief summary of the three models is first presented.

3.1.1 The JKR Model

JKR (Johnson et al., 1971) proposed that in addition to the stored elastic energy of Hertzian contact, a general surface energy term must be introduced to account for the adhesive interactions between the two surfaces in contact. This results in an increase in the area of contact and changes the indentation depth. Based on this analysis, the relationship between the contact parameters can be written as

$$a = \left[\frac{R}{K}\left(P + 3w\pi R + \sqrt{6w\pi RP + (3w\pi R)^2} \right) \right]^{1/3}, \tag{3.1a}$$

$$\delta = \frac{a^2}{R} - \sqrt{\frac{8w\pi a}{3K}} \tag{3.1b}$$

and

$$P_c = \frac{3}{2} w\pi R, \tag{3.1c}$$

where, a is the contact radius, δ is the indentation depth, P is the applied load and P_c is the pull-off force or the minimum load. For contact between two surfaces of the same material the effective modulus corresponds to $K = 4/3\left((1-\nu_1^2)/E_1 + (1-\nu_2^2)/E_2\right)^{-1}$. The adhesive energy or the Dupré energy, w, can be represented as

$$w = \gamma_1 + \gamma_2 - \gamma_{12} \tag{3.2}$$

where γ_1, γ_2, γ_{12} are respectively the surface energies in vacuum of surfaces 1 and 2 and the interface between them. If the contacting materials are the same, the adhesive energy w simplifies to 2γ ($\gamma_1 = \gamma_2 = \gamma$, $\gamma_{12} = 0$). For experiments conducted in laboratory air, γ_{SV} is more appropriate than γ.

3.1.2 The DMT Model

The DMT model (Derjaguin et al., 1975) assumes that the surface interactions occur only outside the contact region. As a result, the contact surface deforms according to the elastic equations of Hertz with the adhesion forces P_a being regarded as an additional external load. Therefore, the contact radius, approach distance and pull-off force may be written as:

$$a = \left[\frac{R}{K}\left(P + P_a\right)\right]^{1/3}, \tag{3.3a}$$

$$\delta = \frac{a^2}{R} \tag{3.3b}$$

and

$$P_c = 2\pi wR. \tag{3.3c}$$

In the original paper (Derjaguin et al., 1975), a thermodynamic approach found that $P_a = 2\pi wR$ at zero contact radius and decreases to $P_a = \pi wR$ at zero external load, which is physically unreasonable. However when a simple force balance was made by integrating the surface interaction forces (Müller et al., 1983a; Pashley, 1984), P_a increased continuously from $2\pi wR$ as the surfaces approach one another. For real applications $P_a = P_c$ may be assumed if the relative approach δ is less than the equilibrium distance between surfaces or $a << R$.

3.1.3 The Maugis Model

The situation where surface interactions are considered inside and outside the contact region was analyzed in several different ways. Maugis (Maugis, 1992) developed an elegant quasi-analytical solution for contact using a fracture mechanics or Dugdale

(Dugdale, 1960) approach that assumes a constant adhesive force of intensity σ_0 until a separation h_0 is reached. Earlier Fogden and White (Fogden and White, 1990) considered more general adhesive interactions using the Green’s function for a half-space. Barthel’s solution (Barthel, 1998) to this problem for general adhesive intractions was obtained in terms of mixed boundary conditions using a linear superposition of Hertz (Hertz, 1882), Boussinesq (Timoshenko and Goodier, 1986), and Lowengrub and Sneddon (Lowengrub and Sneddon, 1965) solutions. In light of Barthel’s work (Barthel, 1998), the basis of the Maugis theory (neglecting friction) is the solution of the following simple mixed boundary value problem in linear elasticity:

$$\begin{array}{ll} u(r)=\delta-\dfrac{r^2}{2R} & \text{for } r\le a \\ \sigma(r)=-p(r) & \text{for } a<r\le c \end{array} , \tag{3.4}$$

where, $u(r)$ is the normal deformation of the surface of the plane (positive if depressed), δ is the displacement in the z direction (increasing with approach) at $r=0$, $\sigma(r)$ is the distribution of normal stress at the surface of the plane (negative if tensile) , $p(r)=\sigma_0$ is the distribution of adhesive pressure (positive if attractive) and the separation between two surfaces is h_0 at $r=c$. Introducing the following non-dimensional parameters

$$\bar{a}=a\left(\frac{K}{\pi wR^2}\right)^{1/3},\ \bar{c}=c\left(\frac{K}{\pi wR^2}\right)^{1/3},\bar{P}=\frac{P}{\pi wR},\ \bar{\delta}=\delta\left(\frac{K^2}{\pi^2w^2R}\right)^{1/3},\ \lambda=2\sigma_0\left(\frac{R}{\pi wK^2}\right)^{1/3} \tag{3.5}$$

the solution for the contact parameters can be obtained from

$$\frac{\lambda\bar{a}^2}{2}\left[\sqrt{m^2-1}+\left(m^2-2\right)\tan^{-1}\sqrt{m^2-1}\right]+\frac{4\lambda^2\bar{a}}{3}\left[\left(\sqrt{m^2-1}\tan^{-1}\sqrt{m^2-1}\right)-m+1\right]=1, \tag{3.6a}$$

$$\bar{P}=\bar{P}_1+\bar{P}_a=\bar{a}^3-\lambda\bar{a}^2\left(\sqrt{m^2-1}+m^2\tan^{-1}\sqrt{m^2-1}\right) \tag{3.6b}$$

and

$$\bar{\delta}=\bar{a}^2-\frac{4}{3}\bar{a}\lambda\sqrt{m^2-1}\ \bar{\delta}=\bar{a}^2-\frac{4}{3}\bar{a}\lambda\sqrt{m^2-1}\ . \tag{3.6c}$$

Note that the relationship between the pull-off force and the adhesive energy is implicit. Thus if the adhesive energy is not known, Eqs. (3.6) have to be solved through numerical iterations. In practice, this is a rather cumbersome approach (Liechti et al., 1997) for obtaining w from data. For convenience, two general methods for approximating the Maugis model have been proposed (Carpick et al., 1999; Pietrement and Troyon, 2000).

3.2 The Modified Tabor Parameters

For solid-solid adhesion, it is known that the JKR, DMT and Maugis models are complementary and apply to different parts of a spectrum of elastic solutions (Eqs. (3.6)) determined by a non-dimensional parameter which was first defined by Tabor (Tabor, 1977)

$$\mu_T = \left(\frac{16Rw^2}{9K^2 z_0^3} \right)^{1/3}, \tag{3.7}$$

where z_0 is the interatomic equilibrium distance in the Lennard-Jones potential for solid-solid interactions. This parameter is the ratio of the magnitude of the elastic deformation to the range of adhesive forces. To see this, the gap h outside the contact zone between two surfaces in contact is proportional to $\left(Rw^2 / K^2 \right)^{1/3}$. If h becomes comparable to z_0, the adhesion force outside the contact zone cannot be neglected. Consequently, a dimensionless parameter $\frac{h}{z_0} \propto \left(\frac{Rw^2}{K^2 z_0^3} \right)$ can be defined to determine when the adhesive interactions outside the contact zone need to be considered and this is the well known Tabor parameter. If the parameter is large, implying that the gap outside the contact zone is much larger than z_0, it is not necessary to consider the adhesion force outside the contact zone and the JKR model then applies. If the parameter is small, the adhesion force outside the contact zone can be considered to be an external load and the DMT model holds. In solid-solid adhesion, z_0 is a measure of the range of adhesive interactions.

When two hydrophilic surfaces are in contact in a humid environment, a liquid annulus (Fig. 3.1) forms as a result of capillary condensation or diffusion from surrounding adsorbed liquid on the surface and the resulting capillary force is dominant (see Appendix B). Consequently for contact in the presence of a liquid meniscus, s or $2r_m$ (twice the Kelvin radius) should be the measure of the capillary interactions and should be substituted for z_0. Therefore, parameters were introduced (Fogden and White, 1990; Maugis and Gauthiermanuel, 1994) for contact when capillary forces are dominant that can be viewed as the modified Tabor parameter

$$\mu_T^c = \left(\frac{16Rw^2}{9K^2s^3}\right)^{1/3} = \left(\frac{2Rw^2}{9K^2r_m^3}\right)^{1/3} . \tag{3.8a}$$

The Maugis parameter $\lambda = 2\sigma_0 \left(\frac{R}{\pi w K^2}\right)^{1/3}$ is quite general and applies to any adhesive interactions between surfaces. In the case of solid-solid interaction $\sigma_0 \cong 1.03\frac{w}{z_0}$ (Maugis, 1992), making $\lambda = 1.16\mu_T$. For capillary interaction, $\sigma_0 = \Delta p = \gamma_{LV} / r_m$ and $w = 2\gamma_{LV}$, so that

$$\lambda^c = \left(\frac{Rw^2}{\pi K^2 r_m^3}\right)^{1/3} = 1.13\mu_T^c . \tag{3.8b}$$

Thus it can be seen that there is a very strong correspondence between the Tabor and the Maugis parameters, if they are interpreted in the manner just described. Greenwood and Johnson (Johnson and Greenwood, 1997) presented an adhesion map based on the Maugis parameter. The interpretation given above to the modified Tabor parameter (Eqs. (3.8)) allows the map to be used for contact in the presence of a liquid meniscus. To summarize, the JKR model can be used when μ_T or $\mu_T^c > 5$, the DMT model when μ_T or $\mu_T^c < 0.1$ and the Maugis model for intermediate cases.

3.3 Further Discussion on the Modified Tabor Parameter

In interpreting the data presented in the ambient environment (45% RH), it was necessary to prescribe a value of Kelvin radius that was used in the modified Tabor parameter. This was accomplished via the Kelvin equation which establishes the relationship between the Kelvin radius and the relative humidity. Substituting the Kelvin equation (Eq. (B3)) into Eq. (3.8a) and invoking $w = 2\gamma_{LV}$, the modified Tabor parameter becomes

$$\mu_T^c = \left(\frac{8R\left(R_cT\ln(p/p_s)/V\right)^3}{9K^2\gamma_{LV}}\right)^{1/3} . \tag{3.9}$$

In surface chemistry studies, the SFA has been widely used to determine the surface tension of liquids using the relationship between the pull-off force and the surface energy or surface tension, which depends on the chosen contact mechanics model. Generally, either JKR (Eq. (3.1c)) or DMT (Eq. (3.3c)) models have been used to describe contact over a wide spectrum of relative humidity. In view of the developments here, it is reasonable to reanalyze these data to account for the dependence of the modified Tabor parameter on humidity and provide guidelines to select proper contact mechanics models for SFA and AFM data obtained in humid environments.

3.3.1 Verification of Young-Laplace Equation

In this section, for generality the relative vapor pressure (RVP) is used instead of relative humidity (RH). We now return to the question that was raised in interpreting the data obtained from experiments in the ambient environments (45% RVP): At what relative vapor pressure does bulk behavior appear? Examining the Young-Laplace equation (Eq. (B2)), derived from macroscopic thermodynamics, the question arises as to the limit of the meniscus radius below which macroscopic thermodynamics ceases to apply. Note that, as $r_m \rightarrow 0$, the Laplace pressure Δp approaches infinity. Fisher and Israelachvili (Fisher and Israelachvili, 1981) examined this issue using the SFA to measure the pull-off forces and used Eq. (3.3c) (DMT) to determine γ_{LV} irrespective of the relative vapor pressure levels. They concluded that, for cyclohexane, the limit occurs at relative vapor pressure levels as low as 10% with a critical Kelvin radius of 0.5-0.6nm, which is almost the size of a molecule. However, for water this limit occurred at 90% RVP with a Kelvin radius of 5nm, which is almost ten times the value for cyclohexane. Considering that the cyclohexane molecules are larger than water ones, this discrepancy is even more remarkable. This issue was reexamined by Christenson (Christenson, 1988) and it was pointed out that the rolling and shearing between two mica surfaces by use of a leaf spring compromised the conclusion (Fisher and Israelachvili, 1981). This rolling and shearing effects resulting from the friction are quantitatively analyzed in Chapter 2 (Eq. (2.8)). In the following, data (Fisher and Israelachvili, 1981; Christenson, 1988) are reanalyzed based on the dependence of the modified Tabor parameter on the relative vapor pressure levels.

We expect the relative vapor pressure to change the applicable contact mechanics model. The general expression for the pull-off force is

$$P_c = n\pi R\gamma_{LV}, \tag{3.10}$$

where the coefficient n is a function of μ_T^c and depends on the chosen model. For example, $n = 3$ if the JKR model applies ($\mu_T^c > 5$) and $n = 4$ if the DMT model applies ($\mu_T^c < 0.1$).

For intermediate values of μ_T^c, Maugis' model should be applicable, but unfortunately there is no explicit expression for the relationship between the pull-off force and the surface tension in this case. Carpick (Carpick et al., 1999) curve-fitted an approximate solution for n when μ_T^c (or λ^c) is known a priori (within ~1% accuracy or better) as

$$n = \frac{7}{2} - \frac{4.04\times\left(1.13\mu_T^c\right)^{1.4} - 1}{2\left(4.04\times\left(1.13\mu_T^c\right)^{1.4} + 1\right)} = \frac{7}{2} - \frac{4.79\times(\mu_T^c)^{1.4} - 1}{9.59\times(\mu_T^c)^{1.4} + 1}. \tag{3.11}$$

Returning to the data (Fisher and Israelachvili, 1981; Christenson, 1988), we now use Eqs. (3.9-3.11) to consider the dependence of n upon relative vapor pressure. Taking the radius of the mica surfaces and the temperature to be approximately 2cm and 294K (21°C), respectively, as mentioned (Fisher and Israelachvili, 1981; Christenson, 1988), and the gas constant R_c of 8.31J/mol/K, the values of the related saturated vapor pressure, bulk surface tension and molar volume are shown in Table 3.1. The elastic properties of mica are shown in Table 3.2. The dependence of μ_T^c and n on p/p_s and the corresponding Kelvin radii placed underneath is shown in Fig.3.2a for water and cyclonhexane. It is seen that the DMT model ($n = 4$) can only be applied at very high relative vapor pressure for both water and cyclohexane.

Considering the water data first, the bulk surface tension is shown in Fig. 3.2b along with the original data assuming $n = 4$ and the modified data using n values obtained from Eq. (3.11) (Fig. 3.2a). Fisher and Israelachvili concluded that bulk behavior manifested above 90% RVP based on γ_{LV}=65 mJ/m^2, which is 90% of the bulk water surface tension. However, the modified data suggest that the bulk behavior can be seen above 50% RVP. It was thought that the critical Kelvin radius was 5nm (90% RVP) in the original paper. However, 50% RVP corresponds to a Kelvin radius of 0.78nm, which is much smaller than was originally claimed. Basically, estimates of surface tension based on $n = 4$ (Fisher and Israelachvili, 1981), will be low. The modified data from Christenson (Christenson, 1988) is always higher than the bulk value. Note that γ_{LV} approaches a plateau in the range of 30-50% of RVP and thus it is reasonable to take this range as the initiation of the bulk behavior.

For cyclohexane, the modified values of γ_{LV} were obtained with n from Fig. 3.2a. The original and modified sets of data from (Fisher and Israelachvili, 1981; Christenson, 1988) are shown in Fig. 3.2c along with the bulk value. Surprisingly both the original data and modified data from (Fisher and Israelachvili, 1981; Christenson, 1988) were consistent when the RVP levels are higher than 10%. Furthermore, the modified values of γ_{LV} were higher than the bulk value for most of levels of relative vapor pressure. One explanation, particularly at low vapor pressure levels is that solid-solid adhesion occurred. However as the vapor pressure increases and more molecules are adsorbed onto the surfaces, the contribution from solid-solid adhesion drops and the values of γ_{LV} should have returned to the bulk value. As it stands, this data does not indicate where the transition to bulk behavior occurs because the values of γ_{LV} were always higher than the bulk value. If we allow for a 10% uncertainty in γ_{LV}, then the transition to the bulk behavior could be said to occur at 30%RH at a Kelvin radius of 0.92nm. This is almost consistent with original claims. It is indicated in Fig. 3.2a that the coefficient n varies more dramatically for water than for cyclohexane. As a result, there is a wider range to the critical Kelvin radius for cyclohexane.

Another parameter (Matsuoka and Fukui, 2002) that has been defined for the transition to bulk behavior arises from the dimensionless critical Kelvin radius, $2r_m^c / d_e$, where r_m^c is the critical Kelvin radius and d_e is the effective molecular diameter. All the values for water and cyclohexane are summarized in Table 3.3. The dimensionless critical Kelvin radius for water is larger than the one for cyclohexane. This difference can be explained by the attributes of the molecules of cyclohexane and water. Cyclohexane is nonpolar while water molecules are polar and interact with mica. As a result, the first one or two monolayers of water adjacent to mica surfaces are constrained, which makes the dimensionless critical Kelvin radius for water larger than the one for cyclohexane by at least 2. This difference is much more reasonable than the values 1 and 18 obtained from (Fisher and Israelachvili, 1981) for cyclohexane and water, respectively.

Although the results in (Fisher and Israelachvili, 1981) were questioned by Christenson (Christenson, 1988), our analyses show that the data from both differed only at low levels of RVP and support that it is necessary to use the modified Tabor parameter to interpret data for surface tension measurements in various relative vapor pressures. Both SFA and AFM are widely used to measure the surface tension of liquids. For SFA the two mica surfaces are molecularly smooth, and thus the measurements are reliable and consistent with the results using other methods. However, for AFM poor reproducibility in pull-off force measurements have been reported (Malotky and Chaudhury, 2001; Jones et al., 2002; Leite et al., 2003; Cleaver and Tyrrell, 2004; Drelich et al., 2004). It appears that the results from AFM measurements are qualitative rather than quantitative. In the cited papers it is pointed out that there are problems in using AFM to determine the surface tension accurately due to the surface roughness, uncertainty in calibration and heterogeneity issues. The surface roughness can be solved by transferring a small amount of liquid to the tip in order to obtain a smoother surface (Putman et al., 1995; Malotky and Chaudhury, 2001; Zamora et al., 2004). The second problem can be solved by directly calibrating the sensor beam in situ (Cleveland et al., 1993; Senden and Ducker, 1994). The use of larger probes may reduce the effect of the molecular heterogeneity on the measurement of pull-off force, but may detrimentally increase the effects of surface roughness.

3.3.2 Selection of Contact Models for SFA and AFM in Humid Environments

Since the surface force apparatus (SFA) and atomic force microscopes (AFM) are widely used in science and industry, it is desirable to develop guidelines for interpreting data obtained from them. Guidelines for determining the appropriate contact mechanics model have been generated for typical material pairs and geometries that are used in SFA and AFM. For SFA, both surfaces are mica and their radius is about 2cm. For AFM, the material of a probe with radius 100nm (conservative estimate) was taken to be Si_3N_4 contacting the mica surface. The elastic properties of probe and substrate are listed in

Table 3.2. The saturated vapor pressure p_s and molar volume V at a temperature of 298K (25°C) are 3.17×10^3 Pa and 1.8×10^{-5}m^3/mol, respectively.

The guidelines were obtained from Eq. (3.9) and are shown in Fig. 3.3. It can be seen that, for the SFA, the DMT model may only be applied to fully saturated (say 99% RH) environments. On the other hand, the JKR model may be used when the relative humidity is below 50%. At intermediate humidity levels the Maugis model should be applied. Thus in ambient environments (40-50% RH), the JKR model is appropriate. These guidelines are consistent with experiments conducted by Maugis and Gauthier-Manuel (Maugis and Gauthiermanuel, 1994).

As to the guidelines for AFM experiments, the DMT model is appropriate for a broad range of humidity levels (>30%) and the JKR model is never valid, although it has been frequently employed. These predictions are also consistent with experiments conducted by Carpick et al. (Carpick et al., 1997) and Schwarz et al. (Schwarz et al., 1995). Furthermore, if stiffer materials and smaller probes are used, the lower humidity limit for use of the DMT model is even lower.

Note that these predictions are based on the assumption that both the Laplace-Young and Kelvin equations hold. However, lower humidity levels give rise to smaller Kelvin radii to the point where the equations no longer hold. For example, when the relative humidity is less than 10%, the resulting Kelvin radius is about 0.2nm, which is of the order of the interatomic equilibrium separation z_0 and less than molecular dimensions, placing the dominance of capillary forces in doubt. According to our earlier discussion, the guidelines developed here apply above relative humidity levels of 40-50%.

Chapter 4 Friction Experiments, Results and Discussions

The purpose of this work is to study the transition of shear strengths from several hundreds of MPa to several tens of MPa. The friction forces obtained with the probes fabricated by the novel procedures introduced in Chapter 2 were measured by the mesoscale friction tester (MFT) discussed in the same Chapter and the corresponding contact area is evaluated by the appropriate contact mechanics theory summarized in Chapter 3. As a result, the shear strength is obtained using Bowden and Tabor's friction law, i.e., the ratio between the friction force and the true contact area. This transition of shear strengths is studied by varying the dimensions of probes. In the following, experimental details, results, discussions and analysis are presented.

4.1 Experiments

In this section, the samples and probes used in the study are introduced first and this is followed by the experimental procedures.

4.1.1 Samples and Probes

In this work, we are interested in single asperity contact in the sense of Tabor (Tabor, 1977) who suggested that single asperity contact occurs when the adhesive force acting on the asperity deforms it by at least the RMS roughness amount. The substrate in all the experiments reported here was freshly-cleaved mica, with an atomically smooth surface. AFM experiments on mica are considered to be single asperity contact due to the sharpness of the probe tips. The mating mica surfaces that are used in SFA experiments are also considered to provide single asperity contact. We have shown in Chapter 2 earlier that the electrochemically etched tungsten probes were almost as smooth. In an ambient environment (RH 45%), the Kelvin radius is about 0.66nm. Any roughness smaller than this gives the appearance of single asperity contact (Putman et al., 1995; Zamora et al., 2004) due to capillary condensation. Furthermore, repeated sliding results in smoother surfaces due to dislocation nucleation, accumulation and annihilation activities (Yu et al., 2003). For this reason, roughly fifty cycles of sliding at zero external normal load were conducted at different locations prior to any data acquisition with a particular probe or environment.

In the present study, three tips with radii of 21.4µm, 5.33µm and 0.90µm were used in the ambient environment (45% RH) and the other three tips with radii of 4.38µm, 1.60µm and 0.31µm were used in the dry environment (5%). The SEM images of these probes are shown in Fig. 4.1. Their surfaces were checked by AFM or the appearance of the oscillatory hydration forces.

4.1.2 Procedures

In the experiments reported here, the ambient environment was controlled simply by building an enclosure around the apparatus. The humidity was measured and found to be nearly constant (45% RH) for the duration of the experiment. The 5% RH environment was obtained with dry nitrogen flush and desiccants (anhydrous calcium sulfate) placed in the chamber. The system was allowed to equilibrate for about 2 hours. The mica sample was attached to the sample stage and cleaved. The surface energy of the freshly cleaved surface depends on the duration of its exposure to the environment (Homola et al., 1990; Israelachvili, 1992a; Miranda et al., 1998; Drew, 1999). For all the experiments conducted in the ambient environment, mica surfaces were exposed to air for about twenty hours prior to friction experiments since we found that the surface energy of such mica surfaces became stabilized. For the experiments in the dry environment, mica surfaces were exposed to dry N_2 from two hours to fifteen hours. The pull-off forces under normal loading were measured before and after each friction experiment in order to extract the adhesive energy and check the consistency of the contacting surfaces during the friction experiment. In the friction experiments, the piezo stage was moved toward the probe until a desired normal load level was achieved. The stage was then moved laterally back and forth across the sample. In order to eliminate possible offset in the lateral force signal resulting from any misalignment of the system, the friction force was obtained as the mean value of the lateral or friction forces in both the forward and backward directions. The scanning speed was about 0.1µm/s. After each scan, the stage was lowered by 0.06 to 0.08µm prior to the next forward and backward scan. These steps were repeated until the tip pulled off the sample. After each series of scans, the probe was examined using SEM and the mica surface was scanned using AFM. No permanent damage was detected on either surface. The mica surface scanned by the tip with 0.90μm radius was analyzed by an X-Ray Photoelectron Spectroscopy (XPS) and no tungsten atoms were detected.

Figure 4.2a shows a typical friction trace for a single line scan at a constant normal load at a relative humidity of 45%. In this case, a compressive normal load of 0.24μN was applied and the probe initially stuck to the mica, but once the critical lateral force was reached, the probe slid over the sample smoothly without any signs of stick-slip behavior. The slight difference in friction force during the forward and backward scan indicates some misalignment. The friction force that was reported for this normal load was the average of the two sliding force signals. Figure 4.2b shows a typical friction trace for a line scan in the 5% RH environment. Because of stronger adhesion between the tip and substrate, the friction trace exhibited stick-slip behavior. The reported friction force was obtained from the average of the maximum friction forces or the first maximum friction forces in the forward and backward scans.

4.2 Results and Discussion

In this section, the results of friction experiments in both ambient and dry environments are first presented. Then the observed transition in shear strengths is discussed with a quantitative analysis of the shear strengths obtained in the present work along with data obtained from previous AFM and SFA friction experiments based on the Lifshtz van der Waals theory.

4.2.1 Experimental Results

Many different experiments were performed, varying the conditions of the specimen, the probe, and the environment. Table 4.1 summarizes the details of the various experiments. We describe the details of each measurement and interpretation in this section.

4.2.1.1 Adhesion Energy Measurements

Normal load experiments were conducted before and after each set of friction experiments. From these measurements, the pull-off force, denoted $P_{c-normal}$, was determined as the average values of four measurements, two each before and after each set of friction measurements and are shown in Table 4.1. The variation in $P_{c-normal}$ was less than 10% for all the experiments; the consistency of these pull-off force measurements indicates that there was no significant change in the contacting surfaces before and after each set of friction experiments. The adhesive energy was evaluated using Eqs. (3.1c) and (3.3c) for all the experiments. This was done in order to establish bounds on the adhesive energy based on the JKR and DMT models. The estimates of the adhesive energy given above are then used to establish bounds on the Tabor parameter μ_T for the dry environment (5% RH; Eq. (3.7)) and the modified Tabor parameter μ_T^c for the ambient environment (45% RH; Eq. (3.8a)). In these calculations, the equilibrium separation and the Kelvin radius were taken as 0.2nm and 0.66nm, respectively. The material properties for Tungsten and mica (c-axis) are listed in Table 3.2. The estimated values of the Tabor parameters (listed in Table 4.1) are then used to select the appropriate contact model for interpretation of the friction force measurements (see Section 3.2). In order to establish the consistency of the contact mechanics model selected as indicated above with the experimental data, both the JKR and DMT responses (two limit cases) are calculated for each set of experiments.

The range of contact radii and the maximum average pressures for each set of experiments are shown in Table 4.1. The lower and upper limits of contact radii correspond to the contact radius at pull-off and the maximum applied load, respectively. The maximum average pressure is evaluated by the sum of the pull-off force and the maximum normal load divided by the corresponding contact area.

It is observed from the data in Table 4.1 that the adhesive energy in the ambient environment is surprisingly low considering the surface tension of bulk water. This apparently anomalous behavior could be due to the presence of purely repulsive, short-range hydration forces (Christenson, 1988; Israelachvili and McGuiggan, 1988; Israelachvili and Wennerstrom, 1996) resulting from the ordering of water molecules. Another possibility is the presence of electrical double-layer forces in the condensed meniscus because the mica substrate provides a reservoir of potassium ions. Both types of force fields are repulsive and act in the presence of the capillary force to reduce the measured adhesive energy. It is possible that adsorbed hydrocarbons on the mica surface during exposure reduce the contact angle as well (Spagnoli et al., 2003). Another issue relates to whether the bulk properties of water still hold when the relative humidity is about 45% (Fisher and Israelachvili, 1981; Christenson, 1988).

It was observed that the pull-off force resulting from the friction experiment – i.e., the lowest value of normal force at which the friction loop measurements could be performed as we progressively decrease the normal force, denoted as $P_{c-friction}$ – was less than $P_{c-normal}$ obtained from normal approach and pull-off experiment. Table 4.2 lists the pull-off forces $P_{c-normal}$ and $P_{c-friction}$ obtained from normal load and friction experiments, respectively and the ratio between them for each probe. Obviously $P_{c-friction}$ was much less than $P_{c-normal}$ for experiments conducted in the ambient environment while the two measures were almost consistent for the dry environment. While it is apparent that $P_{c-friction}$ depends on the adhesion mechanism, it is not clear what kinetic effects or hysteretic effects in the contact zone during friction loop experiments influences this behavior. Since the differences are the largest in capillary dominated contact, it is possible that breakage of the capillary annulus around the contact zone was triggered during sliding, which led to premature pull-off in the ambient environment.

4.2.1.2 Friction Force Measurements

The variations of friction force with normal load for the friction experiments conducted in the ambient environment are shown in Fig. 4.3a, 4.3b and 4.3c corresponding to probes with radii of 21.4μm, 5.33μm and 0.90μm, respectively. In order to interpret the friction force measurements in terms of the interfacial shear strength, we need to employ the appropriate contact model. For the JKR model, the contact area for any normal load was evaluated from Eq. (3.1a), with the adhesive energy determined from the pull-off force measured from the normal force experiments (Table 4.1). With this contact area, the shear strength at each normal load level in the friction experiments was determined from Eq. (1.1). The average shear strength was then computed and multiplied by the contact area to obtain the JKR curve shown in these figures. For the DMT model, the contact area at each normal force level was determined from Eq. (3a) with the pull-off force obtained from the normal force experiments. With this contact area, the shear strength at each normal load level in the friction experiments was again determined from Eq. (1.1). The average shear strength determined from these measurements was then multiplied by the contact area to obtain the DMT curve shown in the figures. Figures 4.3 show clearly that the data obtained under ambient conditions were consistent with the DMT model; note that the modified Tabor parameter μ_T^c (Table 4.1) indicated that the DMT model was the appropriate contact model. The shear strengths determined with this procedure with the DMT model are plotted in Fig. 4.5; we discuss the scale dependence of the shear strength in the next section.

Figures 4.4a, 4.4b and 4.4c show the variations of friction force with the normal force for experiments conducted in the dry environment corresponding to probes with radii of 4.38μm, 1.60μm and 0.31μm, respectively. Predictions of the friction force vs normal force for the JKR and DMT models were again obtained as discussed above. It can be seen from the figures that the data for the probe with a 4.38μm radius are consistent with the JKR model as indicated by the value of the Tabor parameter μ_T. However, the data for probes with radii of 1.60μm and 0.31μm are in the regime of the Maugis theory; the contact areas for the Maugis model were obtained using the method described in (Carpick et al., 1999) with constrained pull-off force shown in Table 4.1. However, for the data using the probe with a 1.60μm radius as shown in Fig. 4.4b, the Tabor parameter $\mu_T = 0.53$ resulting from this curve fit, which is less than the expected value ($\mu_T = 1.58 \sim 1.92$) shown in Table 4.1. From the discussions of Greenwood and Johnson (Greenwood, 1997; Johnson, 1997), when μ_T is greater than 0.5, the contact area predicted by the JKR theory also closely agrees with the values obtained by a numerical solution. The data are indeed quite close to the JKR response. For example, the maximum normal load was about 0.4μN, the contact radius evaluated from JKR model was 61nm and the curve-fit results in a 50nm contact radius. Figure 4.4c shows all the responses for experiments with the 0.31μm probe. The curve-fitted $\mu_T = 0.44$ is in the range (0.43~0.53) of calculated values shown in Table 4.1. The shear strengths shown in both Figs. 4.4b and 4.4c result from the curve-fits to the Maugis model. The results presented in Figs. 4.3 and 4.4 have shown that the relationship between friction force and normal force is consistent with the selected contact mechanics model following the adhesion map given in (Johnson and Greenwood, 1997). It can be concluded from these friction force measurements that for nonwear, single asperity contact, Eq. (1.1) holds firmly up to the load levels approached in these experiments by assuming a constant shear strength τ. Notice that an additional term incorporating a linear dependence of τ on the normal pressure was suggested (He et al., 1999; He and Robbins, 2001). However, the maximum external load was much less or comparable to the corresponding pull-off force in each friction experiment and hence the dependence of the shear strength on the normal pressures may not be apparent.

4.2.2 Transition of Shear Strengths

The main objective of this section is the study of the transition in shear strengths obtained from AFM friction experiments and SFA experiments in one apparatus. This transition was indeed observed in our experimental results displayed in Table 4.1. In the ambient environment, the shear strengths obtained from friction experiments using 21.4μm and 5.33μm probes were 51MPa and 52MPa, respectively and the shear strength using the 0.90μm probe was 350MPa. Similar behavior was observed in the dry environment. The shear strengths using two larger probes with radii of 4.38μm and 1.60μm were 38MPa and 35MPa, respectively and a much higher shear strength of 280MPa was obtained from experiments with the 0.31μm probe. Note that all shear strengths obtained from the ambient environment data are slightly higher than the corresponding ones from the dry environment data; this may be caused by the deviation of the true contact area from the calculated contact areas since the latter depend on the selected contact mechanics model. As mentioned earlier, all contact areas in the ambient environment determined from DMT theory may be conservative. For the case of zero external normal load, the contact area calculated from Eq. (1a) (JKR) or Eq. (3a) (DMT) with the same adhesion energy, the variation in the shear strength is about 2. Consequently, the variation in shear strengths shown in Table 4.1 between ambient and dry environments is not considered to be significant.

Figure 4.5 shows the variation of shear strength with contact radius for both environments. The shear strength, which is on the order of a few hundreds of MPa for contact radii less than about 20nm (consistent with AFM measurements : Carpick et al., 1996; Meyer et al., 1996; Carpick et al., 1997; Lantz et al., 1997; Enachescu et al., 1998), drops down to a few tens of MPa when the contact radii are larger than about 30nm. The lower shear strength persisted as the contact radius was increased over a hundred nm in our experiments; SFA experiments also reinforce this observation at contact radii of several hundreds of μm (Israelachvili et al., 1988; Homola et al., 1989; Homola et al., 1990). The origin of shear strengths in the two extremes of our experiments can be understood as follows: the lower shear strengths (35-50MPa) from experiments using four larger probes in both ambient and dry environments result from contact mediated by one monolayer of some interfacial molecules (most likely water, but also possibly hydrocarbons (Spagnoli et al., 2003)), while the larger shear strengths (280-350MPa) using the two smallest probes result from intimate contact (no interfacial molecules between two surfaces). Consequently, the present experiments provide evidence of an abrupt transition from intimate contact to monolayer lubricant contact at contact conditions intermediate to those observed in the AFM and the SFA friction experiments, rather than for a gradual transition – *this is the main experimental finding of the present work*.

How such an abrupt transition from monolayer lubricated contact to intimate contact occurs remains to be explored. In our experiments it is most likely that the adsorbed water molecules were hydrogen-bonded to two hydrophilic surfaces: mica and WO_3 (electrochemically etched tungsten probes are covered by a thin layer of tungsten trioxide (Lassner and Schubert, 1999; Xu et al., 2007b)). Even in the dry environment, at least a monolayer of adsorbed layer of water molecules exists and this layer disappears only in an ultra-high vacuum (UHV, $<10^{-7}$ Torr) environment (Roth, 1976). During sliding, this layer of water molecules must be squeezed out from the contact zone to obtain intimate contact. Smaller probes and higher normal pressures result in a higher probability to obtain such intimate contact. Figure 4.6 shows the variation of shear strength with the corresponding average maximum normal pressure (Table 4.1). When the maximum average normal pressure is larger than certain level (about 400MPa), the resulting shear strength is high and vice versa. Since we assumed that these interfacial water molecules were hydrogen-bonded to the surfaces, the critical normal pressure level should be high enough to break such hydrogen bonds and then obtain an intimate contact. The Young's modulus of ice (hydrogen-bonded solid) is about 10GPa (Petrovic, 2003) and consequently the theoretical yield strength is about 700MPa ($E/15$). Considering that 400MPa is an averaged pressure for the whole contact area, the corresponding maximum pressure (if simply assuming a Hertz pressure distribution) is consistent with the theoretical yield strength of ice.

The high shear strength of hundreds of MPa was observed using two smallest probes in each environment where the corresponding average normal pressure was higher than 400MPa. The 5.33μm probe was tested at much higher initial normal load of 5μN, which resulted a maximum average normal pressure of about 350MPa. After two friction scans (the resulting friction forces from these two scans were much lower than the ones by assuming an intimate contact), the probe was examined using AFM and the corresponding three dimensional topography, two-dimensional image and a line scan profile are shown in Fig. 4.7. The RMS roughness was about 5nm in contrast to 0.3nm before the sliding experiment. It is most likely the oxidized layer was broken and fell off the probe during sliding. This example shows that the level of the normal pressure is not the only factor to initiate intimate contact.

It was noticed that the shear strengths obtained using different probes are independent of the measured adhesion energies. Even for the same probe, similar shear strengths were obtained whereas the adhesion energies differed considerably. As mentioned earlier, the mica surfaces for these experiments shown in Table 4.1 conducted in the ambient environment were exposed to air for 20 hours prior to the friction experiments. However, from the experiments where mica surfaces were exposed to air for shorter and longer periods, the resulting shear strengths were almost the same at 50MPa. For example, a set of friction experiments using the 5.33μm probe after the mica surface was exposed to air for six hours resulted in a shear strength 47±1MPa ($P_{c-normal}$=1.83μN, $P_{c-friction}$=0.26μN and DMT model). An average shear strength 54±1MPa was obtained from a set of friction experiments using the 21.4μm probe after the mica surface was exposed to air for fifty hours ($P_{c-normal}$=0.88μN, $P_{c-friction}$=0.25μN and DMT model). The same observation was made in the dry environment. This observation is further born out in Table 4.3, which lists a summary of previous friction experiments using AFM and SFA along with our friction results. The shear strengths obtained from these AFM experiments were in the same order of several hundreds of MPa with various material pairs and in various environments such as UHV, dry N_2 and ambient, although the variation of the adhesion energies derived from measured pull-off forces is more than one order and the Young's moduli of these materials vary by up to a factor of ten. Similarly, from SFA experiments, the shear strengths ranged several to several tens of MPa where two mica surfaces were separated by one layer of interfacial molecules in a dry environment or bulk liquids where the resulting adhesion energies could vary about one order. However, considering the adhesive origin of friction, we hypothesize that the obtained shear strength is determined by the *true environment* for friction (the interfacial condition inside the contact zone) rather than the nominal environment. In these experiments, the measured adhesion energies were different, but the resulting interfacial conditions inside the contact zones could be similar and the sizes of these contact zones were affected by adhesion energies along with the applied normal load. In all SFA experiments listed in Table 4.3 two mica surfaces were separated by on layer of interfacial molecules (such as, water, cyclohexane and OMCTS) and the resulting shear strengths were of the same order although the larger molecules resulted a lower shear strength. Since in SFA friction experiments, shear strengths of several tens of MPa were obtained as two surfaces were separated by only one layer of interfacial molecules and furthermore, for contact separated by several layers of interfacial molecules (Israelachvili et al., 1988), the resulting shear strengths were much lower. Consequently, it is reasonable to assume that the shear strengths of several hundreds of MPa were obtained from intimate contact (no interfacial molecules between two sliding surfaces) in these AFM friction experiments.

4.2.3 Analysis of Shear Strengths

In the following, we provide a quantitative analysis to predict the shear strengths according to the corresponding interfacial conditions. We assume that in the present friction experiments van der Waals interactions are dominant for interfacial bonding between the two sliding surfaces and chemical bonds (e.g., electrostatic or ionic bonds and covalent bonds) except metallic bonds are hardly formed due to lack of specificity, stoichiometry and directionality across the interface (Pauling, 1960). This assumption is consistent with the conclusions from both experiments and simulations, in this regime of non-wear contact, that phonon excitation created by the van der Waals interaction is dominant in the atomic origins of frictional energy dissipation for the contact of an adsorbed monolayer or bilayer thin film sliding on a metal substrate (Krim et al., 1991; Cieplak et al., 1994; Daly and Krim, 1996; Tomassone et al., 1997). Furthermore, for bulk specimens usually held by chemical bonds, such as, electrostatic or ionic bonds, metallic and covalent bonds with dimensions only in submicron range, theoretical strengths in the order of GPa have been approached (Brenner, 1956; Agrawal and Raj, 1989; 1990; Uchic et al., 2004). In the AFM experiments and our experiments using the two smallest probes the contact radii ranged from several to ten nanometers. However, the shear strengths (Table 4.3) obtained from these friction experiments were only several hundreds of MPa, even with such small contact dimensions. If such chemical bonds were dominant in friction experiments, the resulting shear strength should have been about one order of magnitude higher. The cold welding (formation of metallic bonds) for a metal-on-metal contact is such example and the resulting shear or tensile strengths of several GPa in the same order of theoretical strength limit were obtained with the contact radii of several to slightly more than ten nm (Rubio et al., 1996; Budakian and Putterman, 2002). In addition, the breaking of such chemical bonding produces debris. Nevertheless, in all friction experiments, the responses from positive normal load to pull-off are consistent, indicating nonwear contact during the whole experiment. This nonwear contact is also supported by the AFM images: if there was wear or debris resulting from the break of formed chemical bonds during sliding, we would not have obtained repeatable and uniform images of the surfaces.

In this idealized view of interfacial bonding formation for friction, van der Waals bonds both in repulsion to support the normal load and in attraction to cause the friction force exist inside the contact zone. The repulsive bonds are always effective even during sliding since the normal load persists; this can be seen in the present experiments where the normal load was constant while the friction force exhibited stick-slip behavior (see Figure 4.2b) as well as in AFM experiments ((Mate et al., 1987; Carpick et al., 1996)). The interaction between the repulsive bonds and attractive bonds during sliding remains an open issue. In the following, the attractive van der Waals bonds that cause friction is our concern. Models which suggest that friction originates from dynamic formation and rupture of molecular bonds using statistical thermodynamics have been proposed

(Chernyak and Leonov, 1986; Filippov et al., 2004). In the following, these bonds are specified to be van der Waals bonds and regarded mechanically so that shear strengths are quantitatively predicted based on Lifshitz theory (Israelachvili, 1992b) and compared with the results of the present experiments, and previous AFM and SFA friction experiments.

Figure 4.8 shows the model that was used in this analysis. The two (rigid) parallel plates represent the two sliding surfaces inside the contact zone and only the atoms on surface layers are shown by the open circles. These two plates are connected by van der Waals bonds (represented in Fig. 4.8 by the springs) to cause friction across the interface. Assuming that the normal separation between two surfaces is maintained by the repulsive bonds for supporting the normal load and remains constant during sliding (the repulsive potential is very steep), the bonds in repulsion are not shown. The van der Waals bonds can be described by a Lennard-Jones potential (Israelachvili, 1992b) $w(z)=4\varepsilon\left(\left(r_0/z\right)^{12}-\left(r_0/z\right)^{6}\right)$, where ε is the minimum energy, r_0 is the hard sphere diameter of the involved molecules or atoms and z is the real separation between two molecules or atoms. Static friction force originates from the quasi-static collective rupture of all such van der Waals bonds and the energy resulting from rupture is dissipated through atomic lattice vibrations (phonon excitation) (Singer and Pollock, 1992). The equilibrium separation between the bonds (corresponding to $w'=0$) is approximately $z_0=1.12r_0$. In Fig. 4.8, the initial positions of van der Waals bonds are shown by the dashed lines. When these springs are stretched to the maximum ($z_{\max}$ in Fig. 4.8) rupture occurs, with the static friction force corresponding to the force at rupture. For the van der Waals bond, the maximum stretching $z_{\max}$ of these springs (corresponding to $w''=0$) occurs at $1.11z_0$. Consequently the angle θ between the bonding direction at rupture and the sliding direction can be determined and the resulting shear strength is obtained in terms of the bond strength σ:

$$\tau=\cos\theta\sigma=0.43\sigma\,, \tag{4.1}$$

The strength of the bonds in the case of intimate contact and interfacial molecule separated contact can be estimated using the Lifshitz theory of van der Waals force

(Israelachvili, 1992b; Butt, 2006), where the two sliding surfaces and interfacial conditions are treated as continuous media in terms of effective bulk dielectric constants and refractive indices (Fig. 4.9c). Consequently the resulting strength of van der Waals bonds between the two macroscopic parallel plates can be represented

$$\sigma = A / 6\pi D^3 , \tag{4.2}$$

where D is the separation between two surfaces and A is the Hamaker constant (Hamaker, 1937; Visser, 1972; Bergström, 1997) which is a complicated function of static and frequency dependent dielectric constants of the materials of two surfaces and the intervening medium. Combining Eq. (4.1) and (4.2), the shear strength is obtained as

$$\tau = 0.43 A / 6\pi D^3 . \tag{4.3}$$

Now we can check the prediction of the shear strength in Eq. (4.3) with our experimental measurements. The Hamaker constant A_{W-mica} between tungsten (W) and mica can be approximated as follows (Butt, 2006):

$$A_{W-mica} \approx \sqrt{A_{W-W} \cdot A_{mica-mica}} \tag{4.4}$$

where, A_{W-W} and $A_{mica-mica}$ are the Hamaker constants between two W surfaces and two mica surfaces, respectively, in vacuum or air. Typically Hamaker constants for metals[2] in the range of $(20\text{~}30)\times10^{-20}$J (Visser, 1972). Assuming that $A_{W-W} = 20\times10^{-20}\,\mathrm{J}$ and $A_{mica-mica} = 10\times10^{-20}\,\mathrm{J}$, results in $A_{W-mica} = 1.4\times10^{-19}\,\mathrm{J}$ in vacuum or air. The shear strength predicted by Eq. (4.3) is about 400MPa if an equilibrium atomic spacing $D = z_0 = 0.2\mathrm{nm}$ is assumed; this estimate is consistent with the higher shear strengths (280MPa and 350MPa) obtained from our experiments with the smallest of probes.

For the case of lubricant mediated contact we assume that the influence of the interfacial molecules on the Hamaker constant is negligible. This assumption is rationalized on the grounds that the Hamaker constants in vacuum and air are not usually

---

[2] Since the values of Hamaker constants of metal or metal oxide are similar (Bergström, 1997), the conclusion is not changed even if a thin layer of oxide covers the probe surfaces.

distinguished, although surfaces in air may be covered by more than one layer of adsorbed molecules. Furthermore, the planar density of such interfacial molecules between two sliding surfaces is unknown and it is possible that during sliding this monolayer of molecules becomes sparse enough just to prevent intimate contact. Accordingly, $A_{W-mica} = 1.4\times10^{-19}$J but the distance of separation is now the sum of z_0 and the diameter of a water molecule ($D = 0.45$nm); the corresponding prediction of shear strength from Eq. (4.3) is about 35MPa, consistent with our experiments (35MPa-52MPa).

In order to examine the applicability of Eq. (4.3) further, we examine previous AFM and SFA friction experimental results from the literature as shown in Table 4.3. The Hamaker constant used to calculate the shear strengths for different material pairs is estimated by Eq. (4.4) but subscripts W and mica are replaced by probe and substrate materials, respectively. Hamaker constants for these materials are obtained directly from the cited work or are estimated from reviews (Visser, 1972; Bergström, 1997). For contact separated by one layer of interfacial molecules separated contact, the separation D is the sum of the diameter of such molecules and the equilibrium spacing z_0. However, if these interfacial molecules (i.e., cyclohexane and OMCTS) are considerably larger than z_0, the separation is assumed to be equal to the diameter of such molecules since larger molecules are more vulnerable to deformation. Figure 4.10 shows the variation of shear strength with separation for the data shown in Table 4.3. Considering the challenge in calculating the Hamaker constant (Visser, 1972; Bergström, 1997), two dashed curves with the Hamaker constant of 10×10^{-20}J and 20×10^{-20}J (two limit values of the Hamaker constant in Table 4.3) are also shown in Fig. 4.10. It can be seen from Fig. 4.10 and Table 4.3 that all obtained shear strengths are reasonably consistent with the values predicted by the analysis. However, the degree of consistency between calculated values from Eq. (4.3) and the experimental results for intimate contact is not as good as in the case of lubricated contact. It is possible that shear strengths obtained from intimate contact may be complicated by several factors, such as, the determination of the separation D (equilibrium separation 0.2nm is always assumed for different materials and the resulting shear strength is very sensitive to D as D is small) (Israelachvili, 1992b), the calibration of the apparatus (AFM) (Carpick et al., 1996), the sporadic formation of non van der Waals bonds, etc.

The above analysis (Eq. (4.3)) based on Lifshitz theory from which the resulting shear strength τ is proportional to D^{-3} is a continuum expectation. However, the spectrum of the separation distance D depends on the interfacial condition, the size and the number of layers of the mediating interfacial molecules, and as a result, is not continuous; consequently, the corresponding shear strengths should be discrete or quantized. For example, in our experiments, the two sliding surfaces were separated by the distance of about 0.45nm or 0.2nm and the corresponding shear strengths were 35MPa and 300MPa, respectively. As a matter of fact, the concept of "quantized shear strength" was initiated by Israelachvili et al. (1988) and it was observed that the shear strength fell by about an order of magnitude per additional layer separating two mica surfaces (approximately the relationship of D^{-3} if the friction force originates from the breakage of van der Waals bonds between two mica surfaces other than the interactions between intermediating liquid molecules). However, when the intervening film approached a thickness of 8 to 10 molecular diameters, the friction measurements reflected the bulk viscosities of liquid films (Israelachvili et al., 1988). In such cases, the current analysis is no longer valid. Note that Robbins (He et al., 1999; He and Robbins, 2001) assumed that the friction force resulted from the interactions between the surface atoms and the adsorbed molecules. One conclusion from this assumption is that the friction force or shear strength increased from one monolayer to two monolayers separated contact, which seems to be inconsistent with experiments (Israelachvili et al., 1988) and the present analysis.

We have discussed that the shear strength is weakly dependent on the material pair in contact and the environment. Based on this analysis, reasonable explanations can be made for this behavior. The weak dependence of shear strength on materials can be explained by the fact that the van der Waals adhesion is weakly dependent on materials since the Hamaker constant is proportional to the product of the square of the molecular number density and the square of the polarizability, but the polarizability is roughly inversely proportional to the molecular number density (Israelachvili, 1992b). In addition, the same "true environment" inside the contact zone for friction is fulfilled because of rubbing in friction experiments although the nominal environment varies. For example, in AFM experiments and our experiments using two smallest probes, the environment of intimate contact existed in a variety of nominal environments, such as UHV, dry N_2 and ambient. The obtained shear strengths were of the order of several hundreds of MPa although Hamaker constants and equilibrium separations for different material pairs are slightly different. In SFA experiments and our experiments using four larger probes, a contact environment of one layer of interfacial molecules was approached irrespective of the nominal environments, such as dry N_2, ambient and bulk liquids. However, for this type of contact, the shear strength depends much on the size of interfacial molecules which determines the separation between two surfaces. For example, the shear strengths obtained from SFA friction experiments were 25MPa, 23MPa and 8MPa for two surfaces separated by water, cyclohexane and OMCTS, respectively. The order of shear strengths is consistent with the order of the size of molecules separating the two mica surfaces as predicted since the same material pair was used.

Several studies (Overney et al., 1992; Frisbie et al., 1994; Green et al., 1995; Noy et al., 1997; Noy, 2006) reported that friction forces were able to distinguish different chemical identities and showed that the stronger the adhesion, the larger the friction force. The correlation between the adhesion and the friction can be explained in two ways. First, the stronger adhesion leads to stronger shear strength if the corresponding true environment inside the contact zone is the same. For example, the corresponding Hamaker constant increases for a stronger van der Waals interaction or this stronger adhesion may result from a higher level interaction (e.g. hydrogen bonding). Second, the stronger adhesion results larger contact area. Recalling Eq. (1.1), both contribute to larger friction force. Additionally, a higher normal load also leads to larger contact area, which may increase the contrast of mapping with friction force as suggested (Frisbie et al., 1994).

At the same time, there is a strong theoretical counter argument to the idea that $\tau = 0.43A/6\pi D^3$ that arises when the two sliding surfaces are incommensurate. In this case the friction force vanishes (He et al., 1999; He and Robbins, 2001). However, the experiments clearly indicated that there was friction during intimate contact, thereby joining the debate on superlubricity (Hirano et al., 1991; 1997).

4.2.4 Lateral Pull-off Force

The friction force can be regarded as the pull-off force in lateral direction with the prescribed contact area. Tomlinson's model (Tomlinson, 1929; Zhong and Tomanek, 1990) has been used to explain and predict the stick-slip behavior in AFM friction experiments and a parameter $\eta = 2\pi^2 E_0 / k_{eff} c^2$ was defined to predict the onset of stick-slip behavior (Johnson and Woodhouse, 1998; Gnecco et al., 2001; Socoliuc et al., 2004; Medyanik et al., 2006), where k_{eff} is the effective lateral stiffness, c is the lattice constant of the surface and E_0 is the amplitude of the surface potential corrugation. Actually E_0 is proportional to the total number of atoms inside the contact zone which is proportional to the contact area. For example, in a one-dimensional model (Fig. 4.11), assuming a sinusoidal surface potential for each atom

$$V_i = -\frac{e_0}{2}\cos\left(2\pi\frac{x}{c}\right) \tag{4.5}$$

where, V_i is the surface potential and e_0 is its amplitude, and thus the total surface potential corrugation

$$V(x) = \sum_{i=0}^{n} -\frac{e_0}{2}\cos\left(\frac{2\pi}{c}(x+ic)\right) = -\frac{ne_0}{2}\cos(\frac{2\pi}{c}x) = -\frac{E_0}{2}\cos(\frac{2\pi}{c}x)\,. \tag{4.6}$$

where, n is the total number of atoms in length L. Since $x \approx c$ and $d^2V/dx^2 > k_{eff}$ when slip occurs or the static friction force results, in essence η can be defined as the ratio of d^2V/dx^2 to k_{eff} in the same way as evaluating the occurrence of the pull-off in the normal loading case (Israelachvili and Adams, 1978). Furthermore, e_0 can be represented alternatively in terms of the theoretical bonding strength and the equivalence between Eq. (1.1) and the friction force at pull-off in lateral direction is evident.

Chapter 5 Friction with Current

In the foregoing, friction experiments between tungsten probes and mica substrates were studied. Friction with current is of interest in many applications (Slade, 1999). The meso-scale friction tester (MFT) was modified to conduct friction experiments (Brown et al., 2007) with current at high density of approximately 10^{10}A/m^2, which is the typical current level found in electro-magnetic launchers (EML). In the following, several observations from experiments with the modified MFT are reported.

Figure 5.1 shows the circuit adjunct to the MFT in order to study the friction with current where connections marked by SHUNT and PROBE are reserved for arching detection and are not used in current experiments. A DC power supply (KLP 300-8-1200, KEPCO, NY) operated in constant current model was used. A tungsten probe with a radius of about 20μm was repeatedly scanned on a copper substrate as received with or without current. In order to protect the polished copper substrate, a 20nm thick layer of palladium was sputter coated on the copper surface. During these scans the normal force was maintained approximately constant at 30μN. Figures 5.2a and 5.2b show the variation of the friction force with time and the lateral displacement of the piezo stage, respectively, for 100 repeated scans without current. It can be seen in Fig. 5.2a that at the beginning the friction force increased as the increase of the number of repeated scanning. During this stage, it is possible that the surfaces were smoothened and the corresponding contact area increased so that a higher friction force was observed. After the peak value, the friction force started to decrease, which could hint the initiation of wear and formation of debris. Finally, the friction force became stabilized with a corresponding friction coefficient of ~0.5-0.6. Figures 5.3a and 5.3b show the variation of the friction force with time and the lateral displacement of the piezo stage in 100 repeated scans with a current density of 10^9A/m^2 (a contact radius of 6μm measured from Fig. 5.4b), respectively. The most distinguishable observation from both Fig. 5.3a and 5.3b is the occurrence of the various maximum friction forces and corresponding multiple stick-slip periods. It is observed that the maximum friction force is proportional to the corresponding stick-slip period by a coefficient, the cantilever-beam bending stiffness. Note that the maximum friction coefficient in the friction scans with current can be as high as 3. Compared to Fig. 5.2a, it seems that there is no apparent transition stage in the history of the friction experiment with current. This may result from the fact that the current density was so high that debris resulting from wear were mostly melted and welded during scanning. During cooling, recrystallization could occur and thus similar surfaces were involved in the following scan. Figures 5.3c, 5.3d and 5.3e show the variation of the friction force with the lateral displacement of the piezo stage during scans of 1st to 5th, 26th to 30th and 96th to 100th, respectively. Some interesting trends become apparent in these figures. In the first five friction loop experiments, uniform sliding is observed, similar to the observation from experiments without current and the friction coefficient appears to be unaltered by the passage of electric current through contact. However, in cycles from 26 to 30, it appears that sporadic stick-slip events occurred at the same location in both forward and backward scanning directions on the specimen. Similar behavior is observed between cycles between 96 and 100 but these stick-slips occurred at a different location.

Figures 5.4a and 5.4b show SEM images of the probe before and after friction experiments with current. It is apparent that the probe tip was worn. The worn area represents the size of the contact zone. The SEM image of the repeatedly scanned track on the copper substrate is shown in Fig. 5.5a. It can be seen that the track is composed of residua resulting from the arcing or melting during scanning with high density current. In addition, there exists an inner track with less debris than the outer areas, this may result from the nonuniform distribution of current density inside the contact zone. A top view of the probe (Fig. 5.5b) shows the size and the shape of the contact area which is represented by the worn area. Comparing Fig. 5.5a to Fig. 5.5b, it is found that the width of the scanned track is slightly larger than the diameter of the worn area (contact zone) of the probe, especially at two ends of the scanned track where the probe was stationary. Figure 5.6a shows a SEM image at high magnification of the area approximately shown inside the black rectangle in Fig. 5.5a. It is shown that the outer area of the scanned track is composed of irregular and circular spots. Figure 5.6b shows a close-up of a circular feature inside the rectangular area shown in Fig. 5.6a. We suggest that this is a result of an arc discharge from the probe to copper substrate although we have not been able to monitor it with optical sensors. Table 5.1 shows the compositions of copper, palladium and tungsten elements obtained from the EDS analyses on different areas noted by 0-7 (shown in Figs. 5 and 6a) on the copper substrate and the tungsten probe. The palladium element originates from the sputter-coated layer on the copper substrate. The area 0 represents the original copper surface. Areas 1, 2 and 3 represent the three different regions of the inner parts of the scanned track. Areas 4 and 5 correspond to the irregular and circular features resulting from scanning, respectively. Areas 6 and 7 represent the original surface and the worn surface (contact zone) of the probe, respectively. For the copper substrate, the variation of composition of W is of interest. Table 5.1 shows that the concentration of W on areas 4 and 5 resulting from scanning is three times the one analyzed on the original copper surface (area 0). Furthermore, the concentrations of W of both irregular (area 4) and circular (area 5) features are almost the same. The extra W was transferred from the W probe through arcing or melting during scanning. Surprisingly, the concentration of W analyzed from the inner part of the track (areas 1, 2 and 3) is almost the same as the original surface. For the tungsten probe, the variation of composition of Cu and Pd is of interest. Table 5.1 also shows that the concentrations of Cu and Pd analyzed on the worn surface of the probe (area 7) are much higher that the ones obtained on the original probe surface (area 6). These extra Cu and Pd were transferred from the copper substrate during frictional sliding with current.

Different maximum friction forces and multiple stick-slip periods were observed during the repeated scanning with current (Fig. 5.3) while the normal load was constant. As a matter of fact, the maximum friction force is proportional to the corresponding stick-slip period. Generally a uniform stick-slip period under a constant normal load was obtained in SFA, AFM and MFT experiments (Homola et al., 1990; Meyer and Amer, 1990; Carpick et al., 1996; Socoliuc et al., 2004), with a corresponding maximum friction force. We hypothesize that the multiple stick-slip periods originate from the heterogeneous structure of the sample surface which is mainly characterized by the grains with various dimensions. This is also reinforced by the observation that stick-slip events occurred at the same location during multiple scans. Figure 5.7 shows an image of a copper sample at 200× which was polished and etched by nitric acid (HNO_3) for about 10 seconds. This image was analyzed using the IMAQ software to obtain the grain size distribution. Due to the resolution limit, the stick-slip period less than 2μm could not be detected in the MFT. The histograms of the stick-slip periods extracted from Fig. 5.3b and the grain sizes analyzed from Fig. 5.7 are shown in Fig. 5.8. It is shown that the distribution of the grain sizes and the stick-slip periods are consistent when the bin size is larger than 2μm. This apparent consistency suggests that the stick-slip period is related to the grain size. Due to the high density current it is assumed that the welding occurred during the stick between the tungsten probe and the copper substrate and the metallic junctions were sheared off at the following slip. It is possible that the shearing or the dislocation movements of these metallic junctions were impeded by various grain boundaries.

Some preliminary observations on the effect of electrical current on friction are presented here. Initial interpretation suggests the possibility of micro arcing, melting and a significant increase in frictional resistance. Further work is needed to confirm these observations.

Chapter 6 Conclusions

The purpose of this work was to study the transition of shear strengths obtained from AFM and SFA friction experiments. Since the applied forces and contact dimensions involved in the friction experiments ranged over several orders of magnitude, neither device by itself could be used to study this transition. As a result, a mesoscale friction tester (MFT) with which a wide range of applied forces and contact dimensions are readily provided was developed. Furthermore, because nonwear and single asperity contact was of interest, novel procedures to fabricate tungsten probes with subnanometer surface roughness were developed. In addition, a modified Tabor parameter was used to select appropriate contact mechanics models for contact dominated by capillary forces dominant contact. In the following, concluding remarks are offered in each of these areas.

The Mesoscale Friction Tester (MFT) Apparatus

A meso-scale friction tester for friction studies covering contact areas from 10nm to 10μm and applied force levels from 10nN to 10mN, which are found in AFM and SFA experiments, respectively, has been developed. It adopted a similar design to an optical-type AFM. This apparatus was directly calibrated by an analytical balance so that any uncertainty in calibration was minimized. During this calibration, it was found that the normal spring constant is affected by the presence of the probe and the relationship between the effective twist angle and true twist angle resulting from the friction force depends on the incident laser beam angle, which are usually neglected in AFM community. These two factors were analyzed and the results predicted from the analytical models were consistent with the ones found in the calibration.

Mesoscale Probe Tips with Sub-nanometer RMS Roughness

Novel procedures for making ultra smooth tips with RMS roughness values up to 0.3nm were developed. The key to making such tips is to maintain the electrochemical polishing process throughout the evolution of the tip. This means that the popular drop-off technique is not suitable for producing ultra smooth surfaces. Electrochemical polishing does not guarantee a specific RMS roughness and recommended practice is to first evaluate tips using SEM. Following that, quantitative assessments of roughness can be made by AFM scans.

A wide range of radii can be obtained by stopping the etching progress at different current levels and by immersing the wire inside the meniscus at different heights above the nominal air/electrolyte interface. For example, for the 0.2mm diameter tungsten wire used in this study, tips with radii ranging from 0.1µm to 50µm were obtained. Sharper tips could be obtained by monitoring the rate of the current decay rather than the current itself.

Tips obtained in these ways are candidates for applications where probes with ultra smooth surfaces are needed or studies of scale dependence are contemplated. These procedures are generally based on electrochemistry, mechanisms of electrochemical etching, polishing and capillarity. We believe that they are applicable to other materials that can be electrochemically etched/polished.

On the Modified Tabor Parameter

A modified Tabor parameter that accounts for contact in humid environments to specify the appropriate contact mechanics model was considered. This parameter was first introduced by Fogden and White (Fogden and White, 1990) who introduced the Kelvin radius as a critical dimension for model selection. Further consideration of this parameter was provided by Maugis and Gauthier-Manuel (Maugis and Gauthiermanuel, 1994). These parameters reflect the ratio between the separation and the range of adhesion interactions. Accordingly, the equilibrium interatomic spacing that appears in Tabor’s original parameter for solid-solid contact was replaced, for contact in humid environments, by twice the Kelvin radius. This parameter is referred to as the modified Tabor parameter. This concept can be extended to contact dominated by other interactions such as electrostatic or magnetic ones.

Previous experimental data (Fisher and Israelachvili, 1981; Christenson, 1988) was reanalyzed using the modified Tabor parameter. It was found that the data should have been analyzed using Maugis' theory rather than the DMT model. Furthermore, the critical Kelvin radius for water and cyclonhexane was 0.78nm and 0.92nm instead of 5nm and 0.5nm, respectively. However these critical Kelvin radii for polar and nonpolar liquids were reconciled by considering (Matsuoka and Fukui, 2002) the dimensionless critical Kelvin radius.

Guidelines for the selection of proper contact mechanics models for SFA and AFM experiments in humid environments were developed. These guidelines are applicable at humidity levels where macroscopic thermodynamics or bulk behavior holds. For SFA experiments, the DMT model may only be used above 99% RH. The JKR model is applicable below 55% RH and the Maugis model may be used in the intermediate relative humidity levels. For AFM experiments, the DMT model is applicable over a broad range of humidity (>30%) but the JKR model should never be used.

The Transition from Intimate Contact to Monolayer Lubricated Contact

Using the newly developed mesoscale friction tester (MFT), the transition of shear strengths from AFM and SFA friction experiments was bridged. This transition was observed over contact radii ranging only 20~30nm in both ambient and dry environments. Shear strengths in tens of MPa resulted from contact separated by one layer of interfacial molecules and shear strengths in hundreds of MPa resulted from intimate contact (no interfacial molecules inside the contact zone). It was the interfacial condition inside the contact zone that governed the transition. As a result, it is suggested that the frictional shear strength is determined by the true environment inside the contact zone rather than the nominal environment. A continuum analysis based on Lifshitz theory which related the shear strength to the estimated strength of van der Waals bonds was used to explain such discretized shear strengths obtained from our experiments and both previous AFM and SFA friction experiments. The resulting shear strength is discrete because the separation between two sliding surfaces was not continuous (at least by one diameter of interfacial molecules). This analysis was consistent with data obtained from AFM, SFA and our experiments. We further suggest that the static friction force can be regarded as a pull-off force in the lateral direction with a prescribed contact area, whose occurrence can be defined in the same manner as the one for the normal pull-off force.

Remarks and Future Work

Based on the present investigations and conclusions, remarks and future work are suggested as follows:

- How the contact condition changes from monolayer lubricated contact to intimate contact still remains to be studied. Smaller probes and higher normal pressures result in a higher probability to obtain intimate contact. The smaller the probe, the easier the interfacial molecules are squeezed out from the contact zone. The higher the normal pressure, the higher the possibility to break the bonds between adsorbed molecules and surfaces. It is possible that the longer sliding durations and higher scanning speed could also contribute to the breakage of the bonds to help obtain intimate contact at lower normal pressures with larger probes. Such experiments are suggested to explore this issue.
- The current investigation of friction is valid for an elastic, nonwear and single asperity contact. The energy dissipation is limited to the rupture of interfacial bonds by neglecting energy dissipation in the probe and the substrate themselves (an analogy to linear fracture mechanics). However, if the normal load is high enough, plastic dissipation either in the probe or in the substrate may substantially contribute to the total energy dissipation. This possibility is foreseen from the fracture mechanics where plastic dissipation could be dominant.
- The friction experiments with high current density mentioned in Chapter 5 were just preliminary. Since another variable, current, was involved, the friction behavior became more unpredictable. The most significant feature is that multiple stick-slip periods were observed and the corresponding friction forces proportional to these periods varied dramatically at the same normal load level. This phenomenon deserves a sound explanation. One suggestion is to obtain stick-slip distributions using probes with various dimensions so that the resulting contact size should be larger than, equal to or smaller than a

typical grain size. The smaller the ratio of the contact size to the grain size, the larger the possibility that the probe contacts over a single grain instead of across the grain boundaries to form metallic junctions. It is expected that the stick-slip periods and the maximum friction forces will become more uniform at the same level of normal load when a smaller probe is used.

Tables

Table 2.1 Summary of spring constants

Cantilever	k_{normal} (N/m)	$k_{lateral}$ (N/m)
#1	0.74	11.88
#2	0.22	1.90

Table 3.1 Properties of cyclohexane and water at 21°C

Liquid	Saturated vapor p_s ($\times 10^4$Pa)	Surface tension γ_{LV} (mN/m)	Molar volume V ($\times 10^{-4}$m^3/mol)
Cyclohexane	1.08	25.5	1.09
water	0.249	72.5	0.18

Table 3.2 Elastic properties of materials considered in this study

Material	Young's Modulus (GPa)	Poisson's ratio	Source
Mica (c-axis)	55	0.1	(McNeil and Grimsditch, 1993; Carpick et al., 1996)
W	392	0.28	(Wang, 2005)
Si	168	0.22	(Wang, 2005)
Si_3N_4	310	0.22	(Barsoum, 1997)

Table 3.3 Critical data for cyclohexane and water

Liquid	Critical RVP	Critical Kelvin radius r_m^c (nm)	Effective molecular diameter d_e (nm)	Critical dimensionless Kelvin radius $2r_m^c / d_e$
Cyclohexane	0.30	0.92	0.56	3.3
Water	0.50	0.78	0.28	5.5

Table 4.1 Summary of experiments and corresponding quantities

RH (%)	Exposure Period (hour)	Tip Radius (μm)	Pull-off Force (μN)	Adhesive Energy (mJ/m^2)		μ_T & Model	μ_T^c & Model	Contact Radius (nm)	Shear Strength (MPa)	Average Maximum Pressure (MPa)
				DMT	JKR					
45	~20	21.4	4.62 ±0.33	34	46	not applicable	0.16~0.20 ~DMT	104~132	51±1	130
	~20	5.33	0.979 ±.009	29	39	not applicable	0.09~0.11 DMT	36~45	52±1	190
	~20	0.90	0.144 ±.003	25	34	not applicable	0.04~0.05 DMT	13~16	350±10	400
5	~2	4.38	12.64 ±1.03	459	612	3.68~4.45 ~JKR	not applicable	102~153	38±2	190
	~5	1.60	2.17 ±0.15	216	288	1.58~1.92 Maugis	not applicable	35~50	35±1	220
	~15	0.31	0.139 ±.003	72	96	0.43~0.53 Maugis	not applicable	7~14	280±13	580

Table 4.2 Summary of pull-off forces

RH	45%			5%		
Probe (μm)	21.4	5.33	0.90	4.38	1.60	0.31
$P_{c-normal}$ (μN)	4.62	0.979	0.144	12.64	2.17	0.139
$P_{c-friction}$ (μN)	1.15	0.368	0.007	12.44	1.86	0.123
$P_{c-friction} / P_{c-normal}$	0.25	0.38	0.05	0.98	0.86	0.88

Table 4.3 Summary of friction experiments with single asperity contact

Contact	Material pair	Environment	Shear Strength (MPa)		Reference	Apparatus
			Exp.	Eq. 11[e] (A_1; A_2) $\times 10^{-20}$J		
Intimate	W-mica	Dry N_2	280	400(20; 10)	-	MFT
	W-mica	Ambient	350	400(20; 10)	-	MFT
	WC-Diamond	UHV	238	490(10[f]; 30)	(Enachescu et al., 1998)	AFM
	Si_3N_4-mica	Ambient	680	380(18; 10)	(Carpick et al., 1997)	AFM
	Si-$NbSe_2$	UHV	610/660	450(25; 10[f])	(Lantz et al., 1997)	AFM
	Pt coated Si_3N_4-Mica	UHV	270-960	570(40[g]; 10)	(Carpick et al., 1996)	AFM
	Si-NaCl	Dry N_2	145-478[d]	360(25; 6.5)	(Meyer et al., 1996)	AFM
One layer separated	W-mica	Dry N_2	35/38	35(20; 10)	-	MFT
	W-mica	Ambient	51/52	35(20; 10)	-	MFT
	Mica-Mica	Dry N_2[a]	25	25(10; 10)	(Homola et al., 1990)	SFA
	Mica-Mica	Bulk Cyclohexane[b]	23	18[h](10; 10)	(Israelachvili et al., 1988)	SFA
	Mica-Mica	Bulk OMCTS[c]	8	4[h](10; 10)	(Israelachvili et al., 1988)	SFA

[a] Two surfaces were separated by a monolayer of interfacial molecules (most likely water) with a thickness of 0.3-0.5nm.

[b] Two surfaces were separated by a layer of cyclohexane molecules (molecular diameter 0.5nm).

[c] Two surfaces were separated by a layer of OMCTS molecules (molecular diameter 0.85nm).

[d] Data calculated from extended JKR for both terrace and step sites.

[e] $A_{12} \approx \sqrt{A_1 A_2}$, where, A_1 and A_1 are Hamaker constants of probe and substrate materials, respectively.

[f] A typical Hamaker constant 10×10^{-20}J are assumed since no data are available.

[g] Estimated from Au.

[h] The separation D equal to the diameter of such molecules is assumed since their size is much larger than 0.2nm.

Table 5.1 Summary of compositions of Cu, Pd and W for different areas of the copper substrate and tungsten probe

Area		Cu (%)	Pd (%)	W (%)
Copper Substrate	⓪	76.8	21.1	2.1
	①	58.2	40.2	1.6
	②	70.7	29.3	1
	③	71.8	24.8	3.4
	④	65.4	28.5	6.1
	⑤	64.8	28.6	6.6
Tungsten tip	⑥	0.1	3.5	96.4
	⑦	15.1	5	79.9

Figures

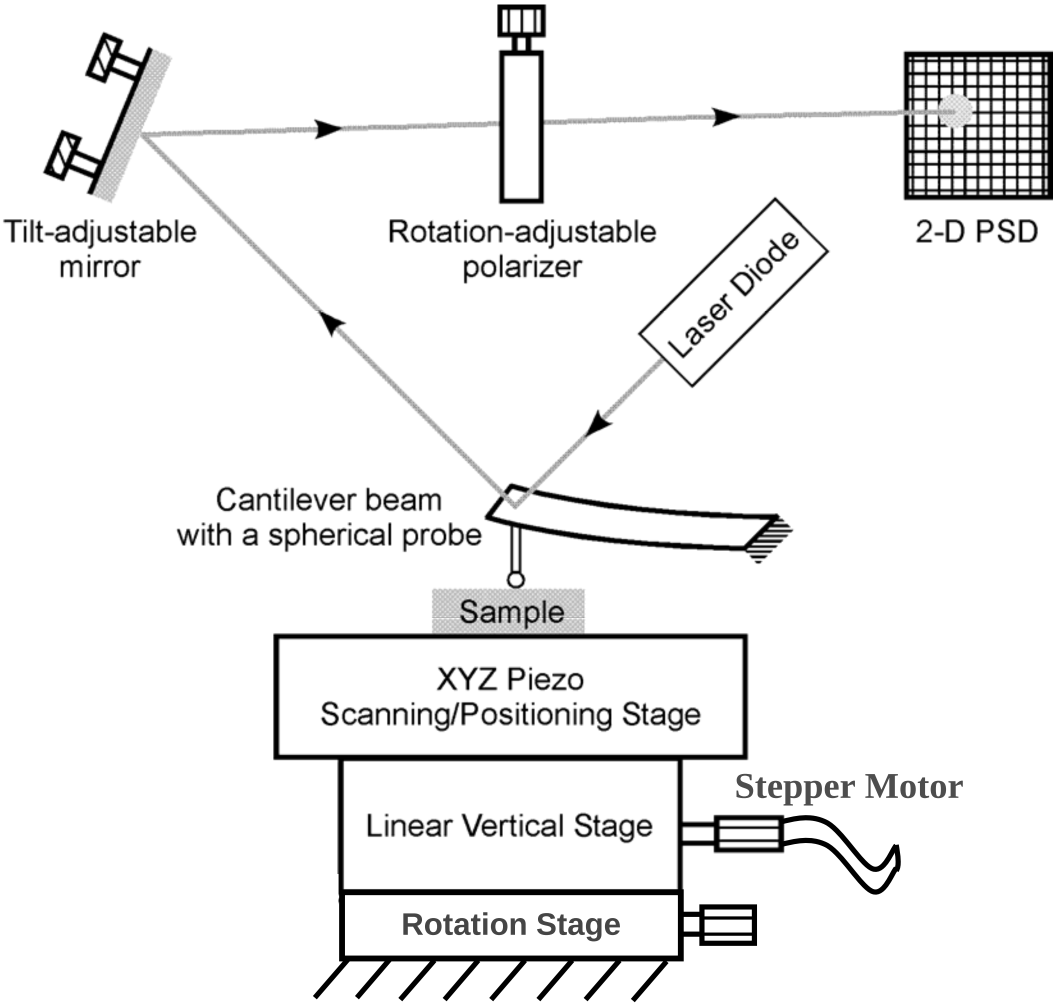
Tilt-adjustable mirror
Rotation-adjustable polarizer
2-D PSD
Laser Diode
Cantilever beam with a spherical probe
Sample
XYZ Piezo Scanning/Positioning Stage
Stepper Motor
Linear Vertical Stage
Rotation Stage

(a)

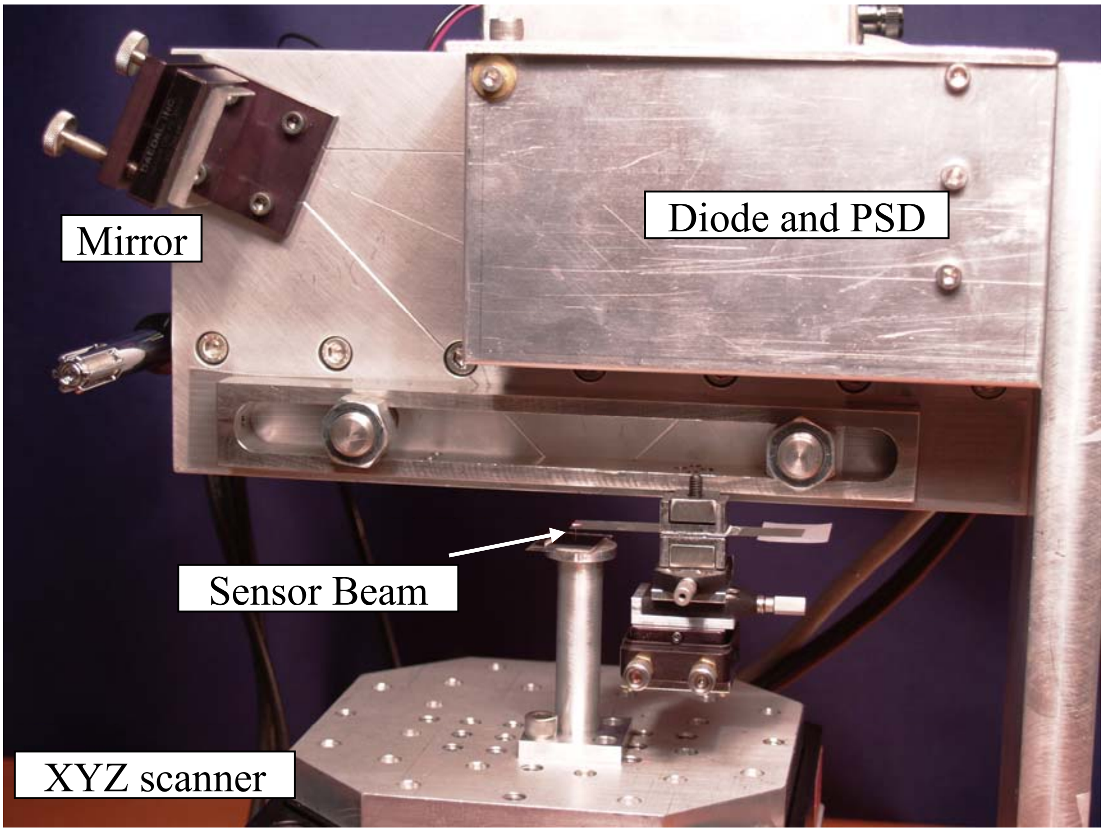

(b)

Figure 2.1 The meso-scale friction tester (MFT) (a) an operational schematic and (b) a photograph.

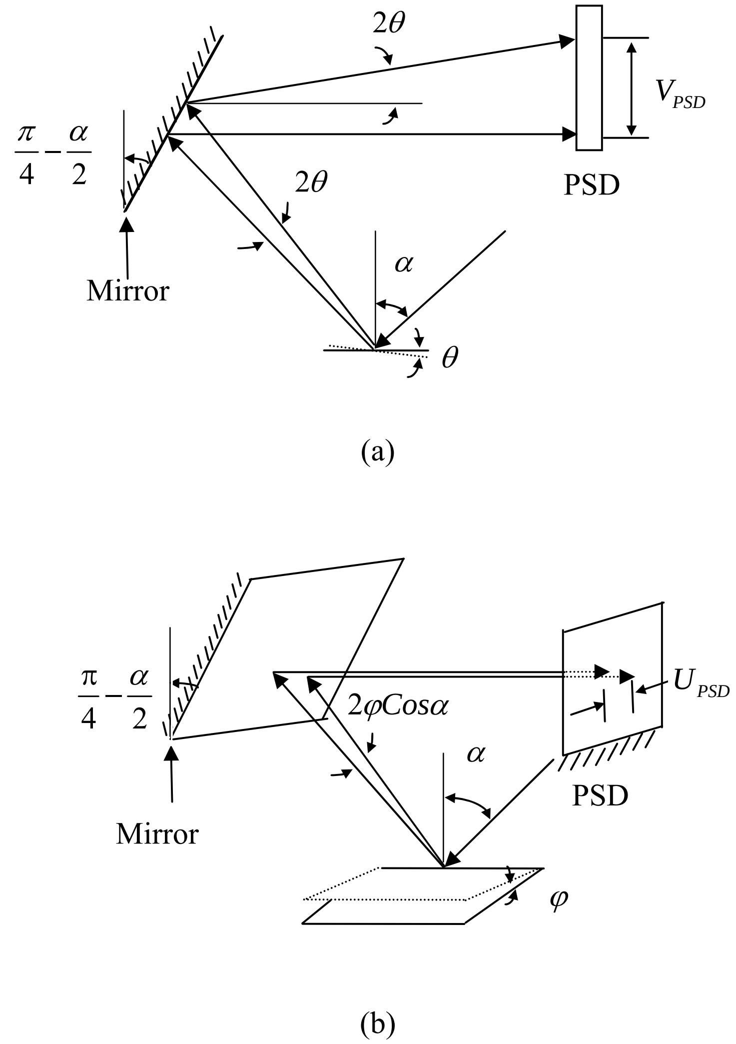

Figure 2.2 Schematics of the geometrical relationship for the angular deflections resulting from (a) normal force and (b) friction force.

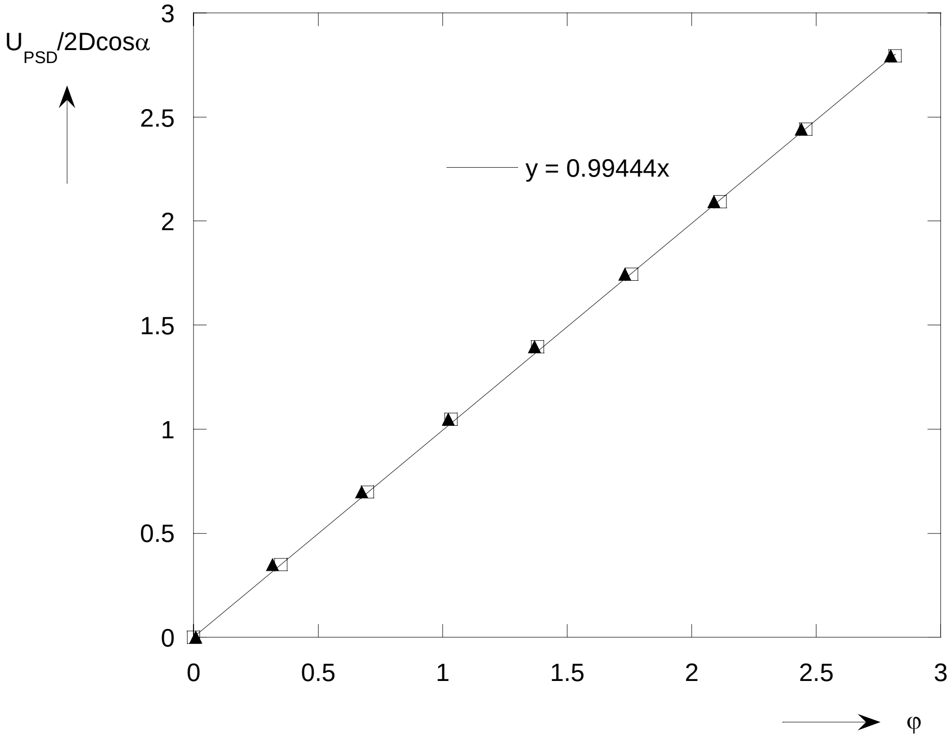

Figure 2.3 The variation of $U_{PSD}/2D\cos\alpha$ with φ in two calibration processes.

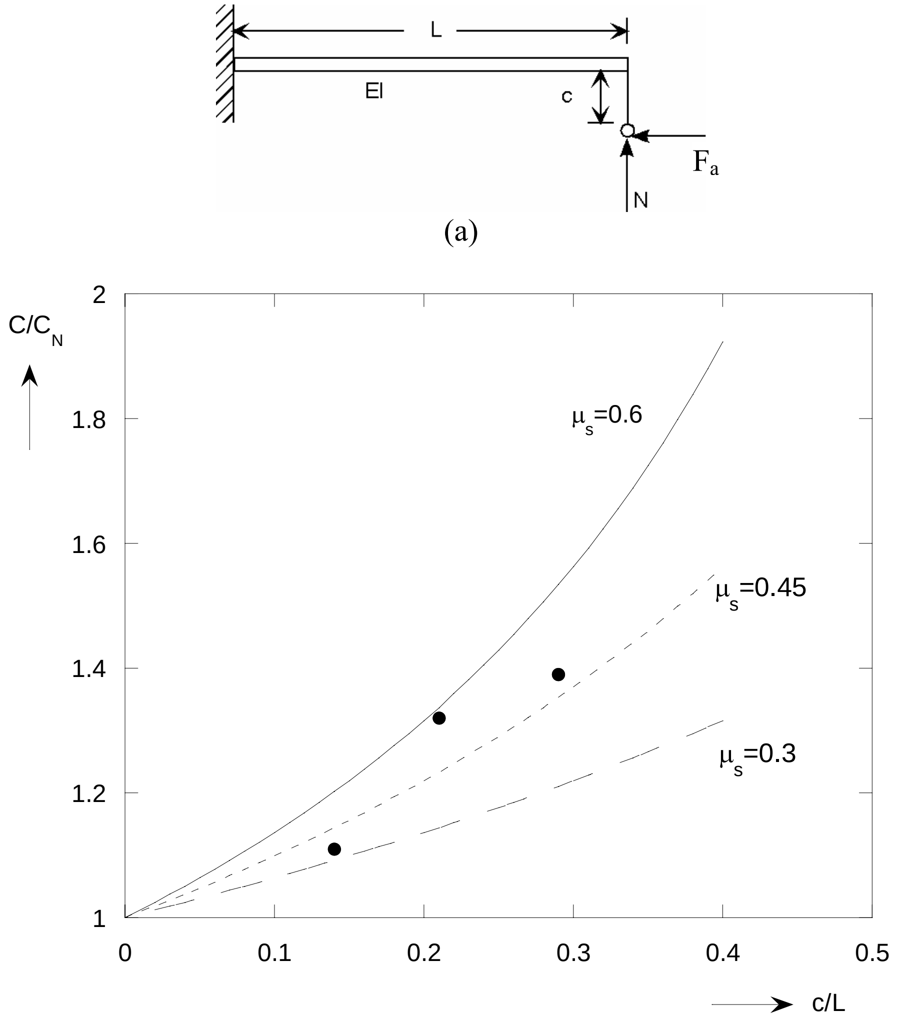

(b)

Figure 2.4 (a) A schematic of the normal force and accompanying axial friction force and (b) the variation of C/C_N with c/L obtained from three coefficients of static friction. Each datum represents the average of three calibrated values.

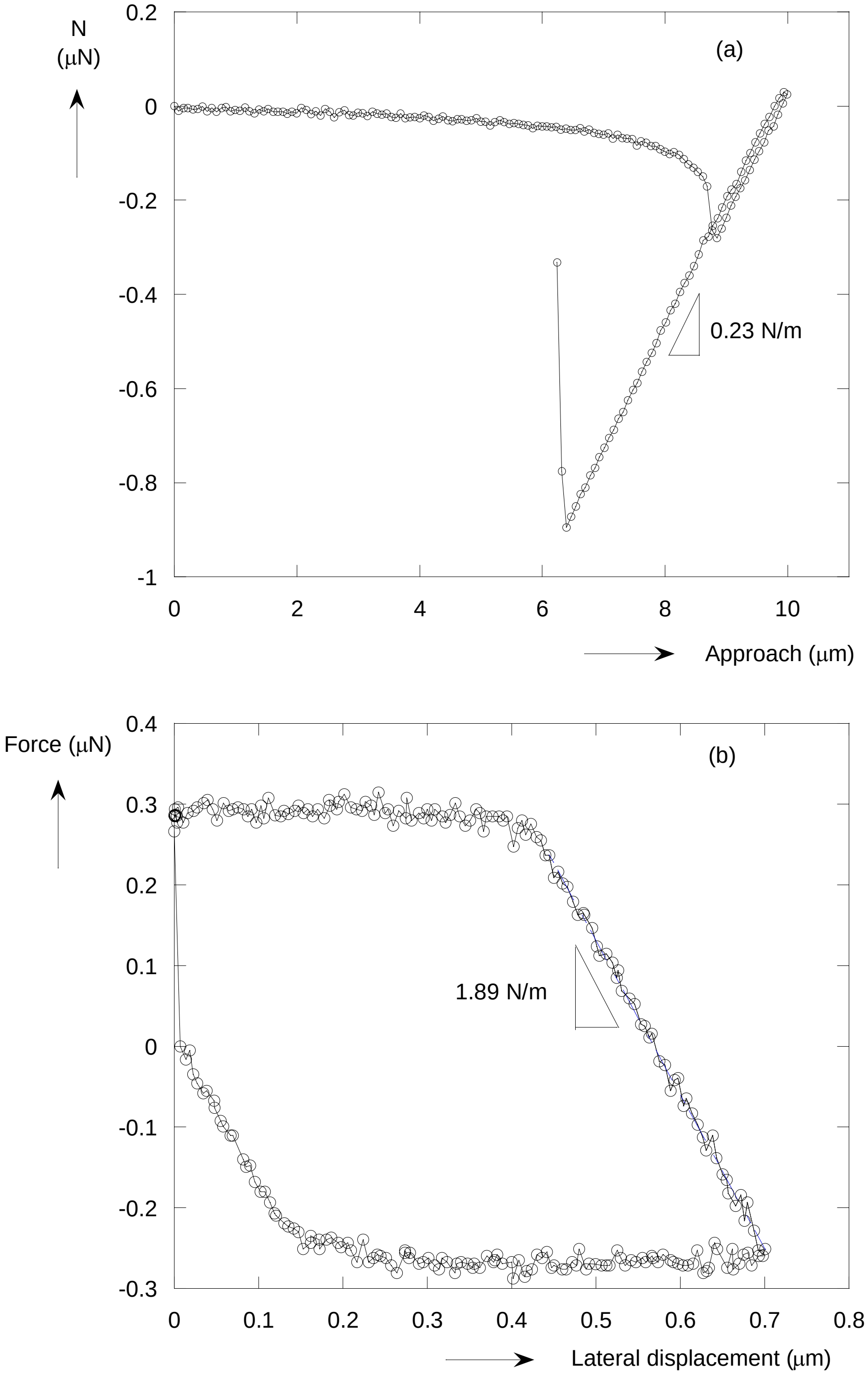

Figure 2.5 **(**a) The normal force vs. vertical displacement and (b) the friction force vs. lateral displacement obtained from the pull-off force and friction force measurements, respectively. The slopes of linear parts of these two curves are shown. These experiments were conducted using a probe with 5.33μm radius in an ambient environment (RH 45%).

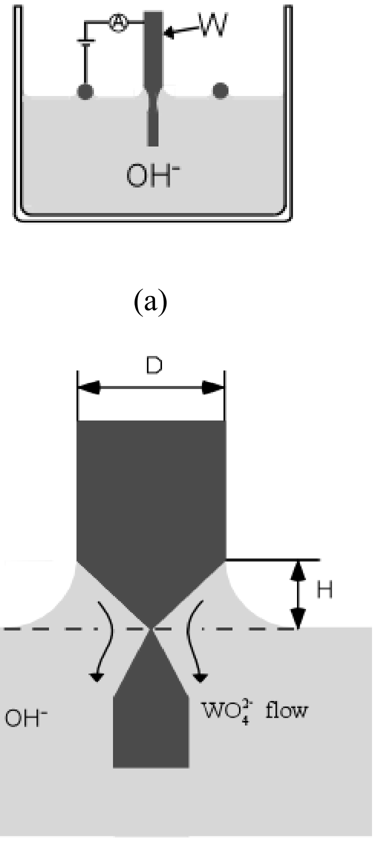

(a)

(b)

Figure 2.6 (a) A schematic of a typical electrochemical etching cell for W and (b) the meniscus at the air/electrolyte interface, where H is the height of the meniscus and D is the diameter of tungsten wire.

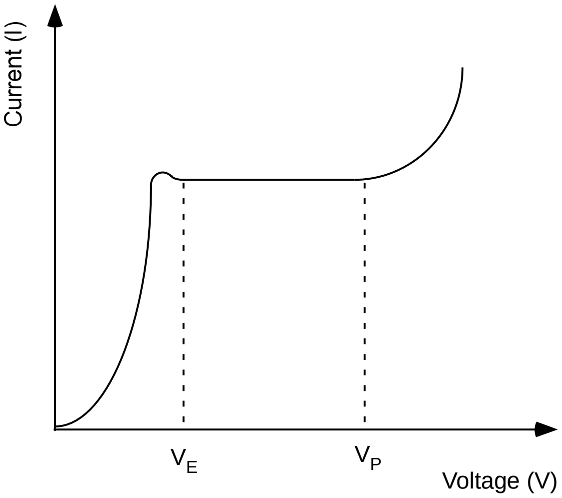

Figure 2.7 A schematic of the voltage-current (I-V) curve for a typical electrochemical etching/polishing process with a metal anode.

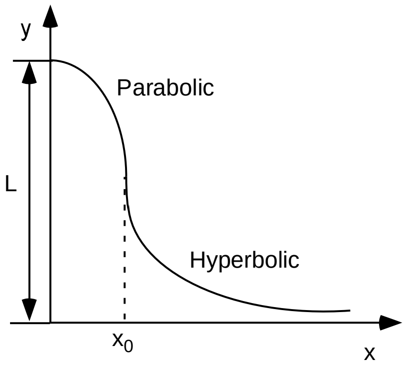

Figure 2.8 A schematic of a tip composed of a paraboloid and a hyperboloid.

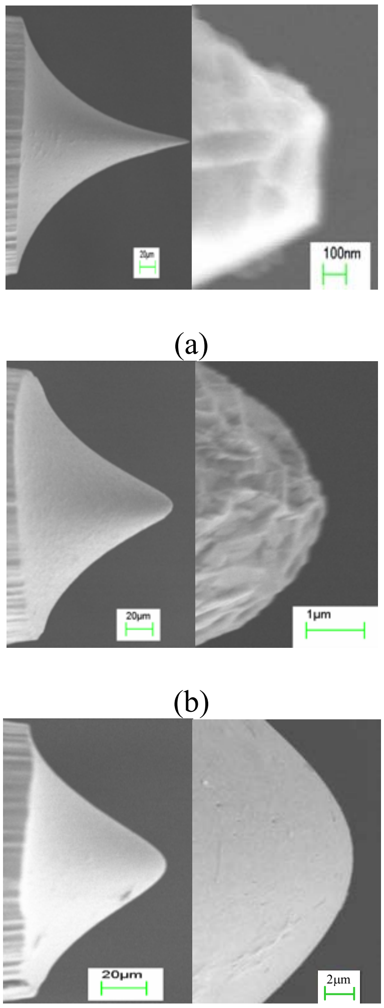

Figure 2.9 SEM images of tips obtained by terminating the etching process after (a) 0.5s, (b) 60s and (c) 240s once the lower portion has dropped off.

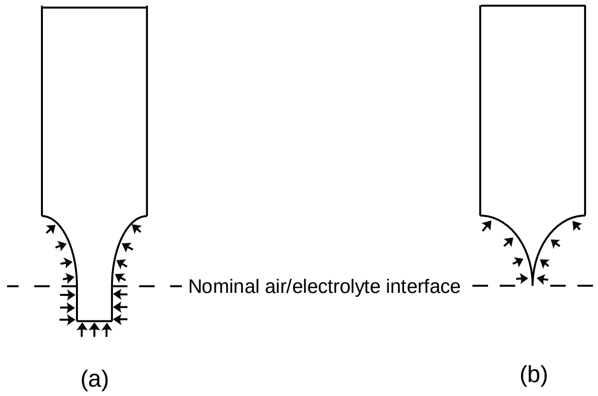

Figure 2.10 Schematic views of the etching progress (a) before and (b) after a pointed tip is formed when the immersed depth is about half the diameter of the wire (there is no drop-off).

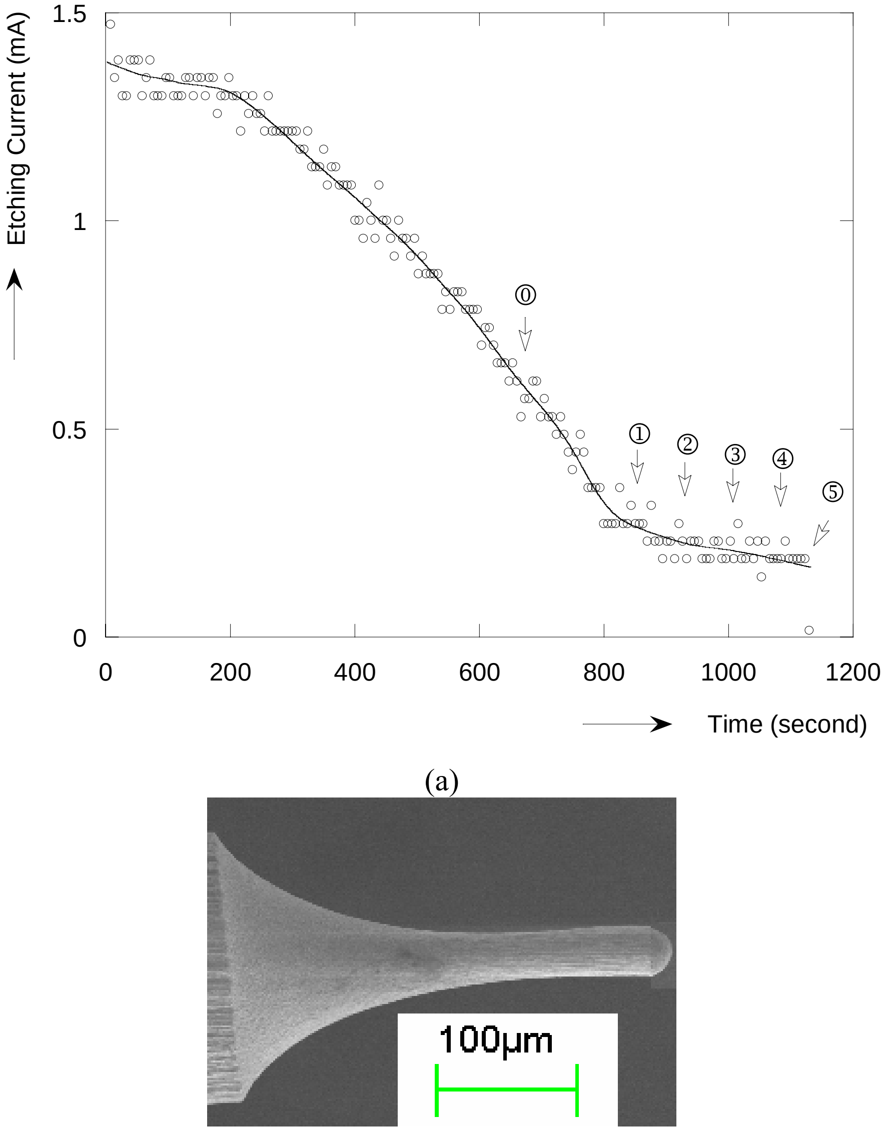

(a)

(b)

Figure 2.11 (a) A typical current history of the etching process and (b) the etched shape when the etching was stopped at ⓪ (i.e. before a pointed tip is formed).

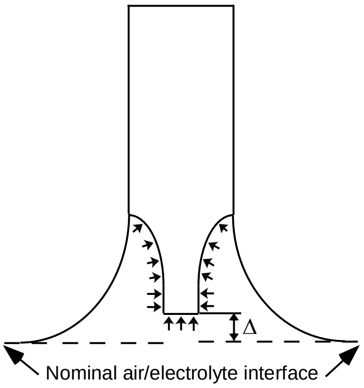

Figure 2.12 A schematic for immersing the wire inside the meniscus at a distance Δ above the nominal air/electrolyte interface.

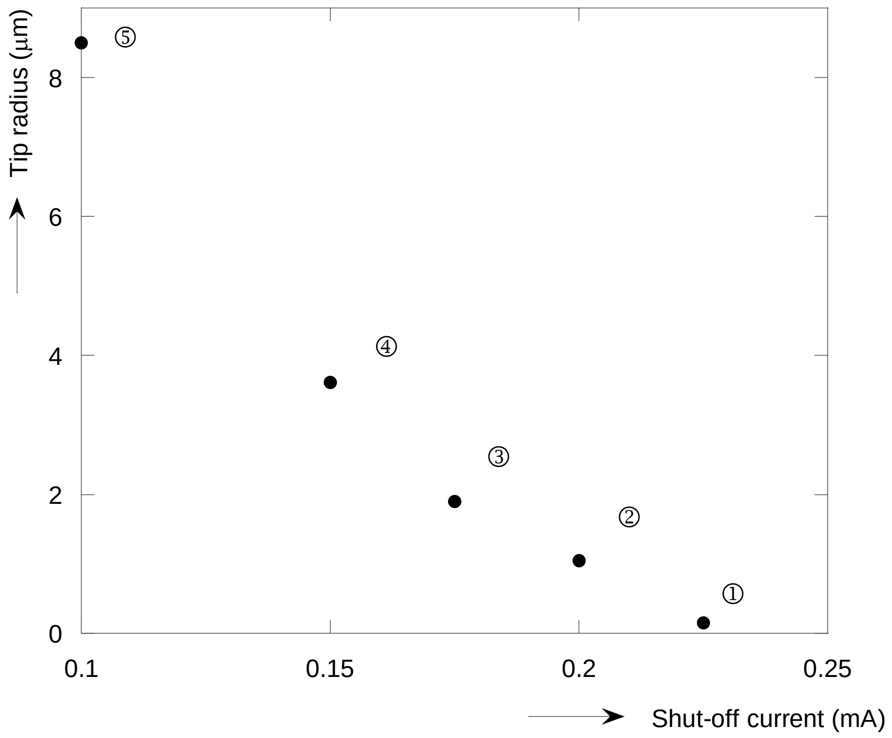
Tip radius (µm)
0
2
4
6
8
0.1
0.15
0.2
0.25
Shut-off current (mA)
①
②
③
④
⑤

(a)

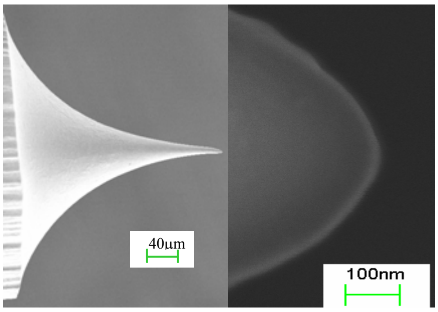
40µm
100nm

(b)

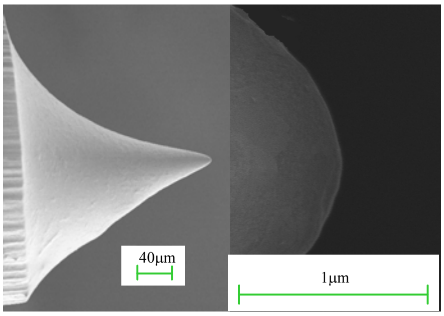
40µm
1µm

(c)

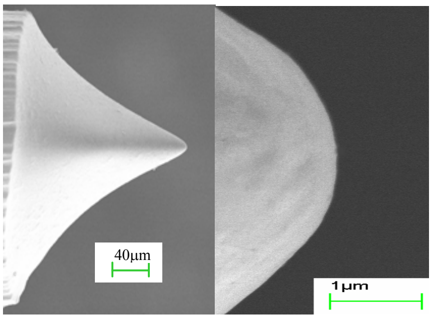

(d)

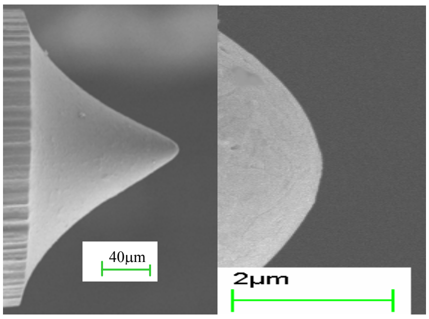

(e)

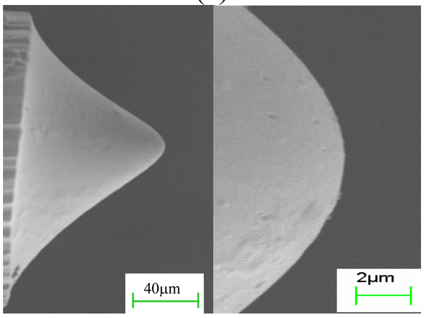

(f)

Figure 2.13 (a) The variation of tip radii with shut-off current. Images of the resulting tips with radii of (b) 150nm, (c) 1.05µm, (d) 1.90µm, (e) 3.61µm and (f) 8.50µm corresponding to ①, ②, ③, ④ and ⑤ in (a) , respectively.

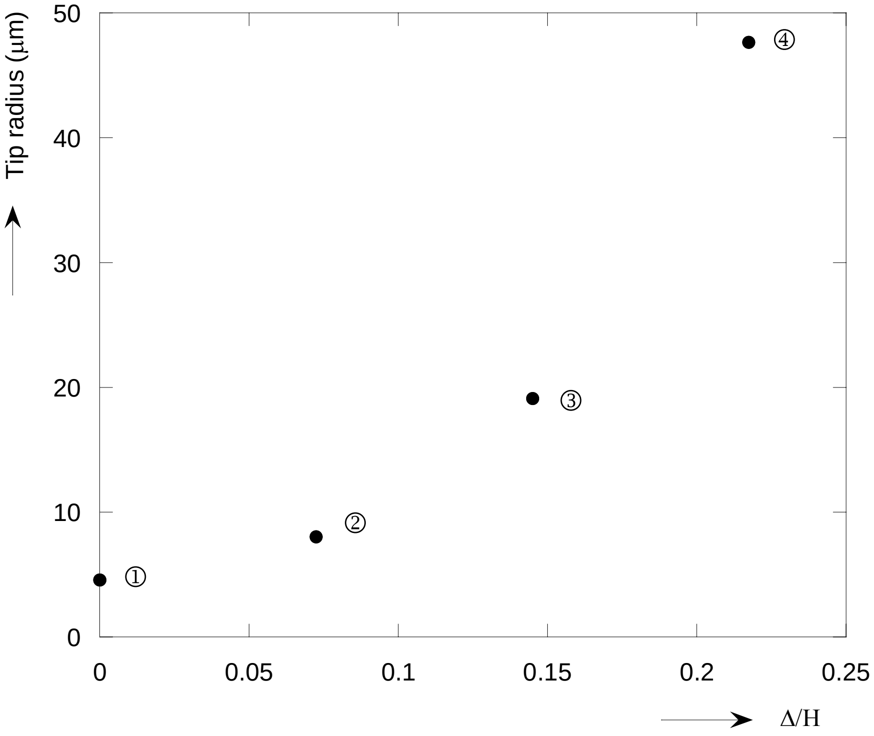

(a)

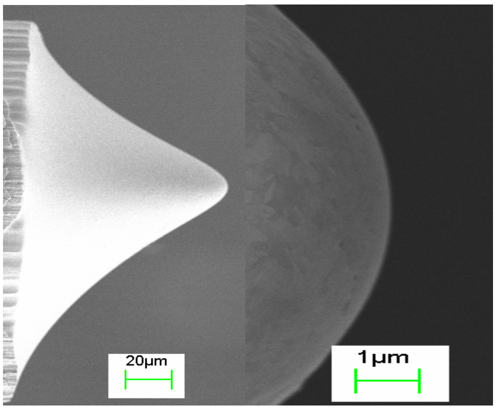

(b)

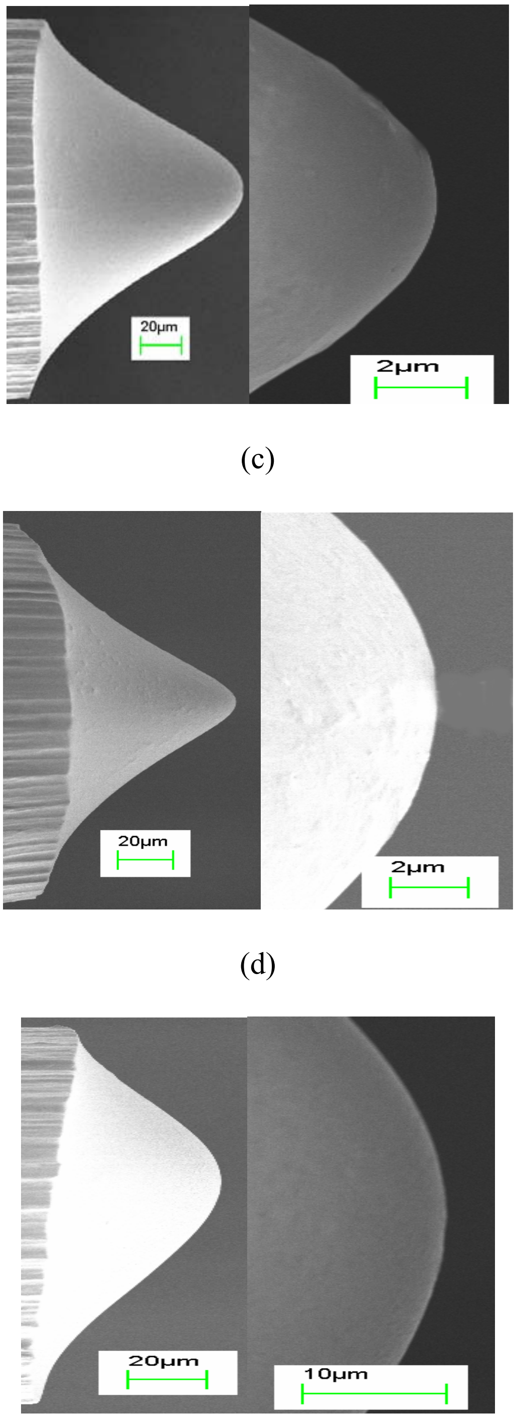

(c)

(d)

(e)

Figure 2.14 (a) The effect of the dimensionless distance Δ / H above the nominal air/electrolyte interface on the variation of tip radii obtained upon rupture of the meniscus. The resulting tips with radii of (b) 4.57μm, (c) 8.01μm, (d) 19.13μm, and (e) 47.62μm corresponding to ①, ②, ③ and ④ in (a) , respectively.

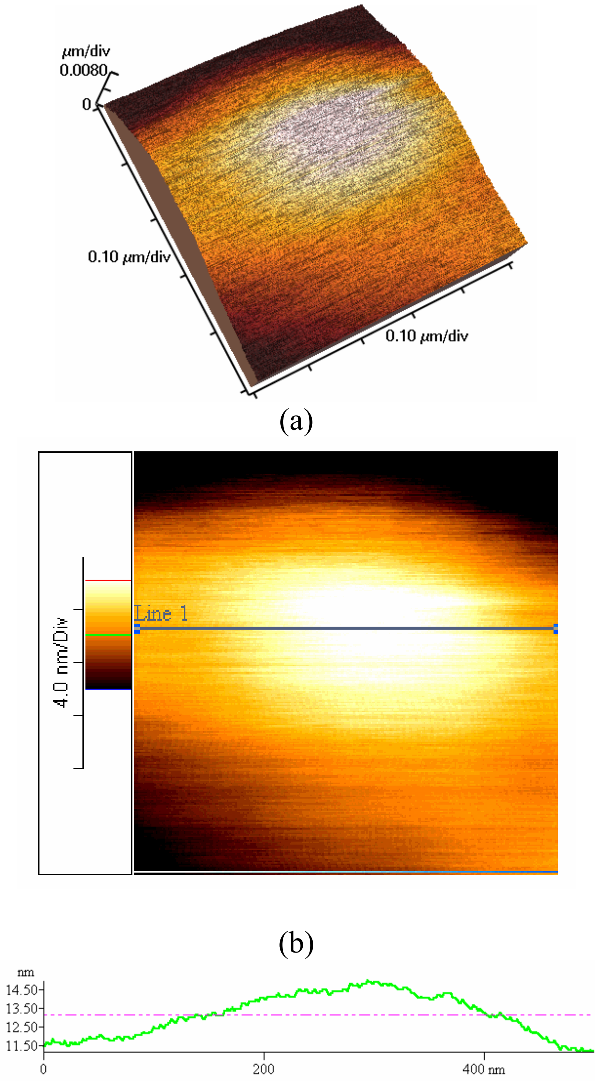

(a)

(b)

(c)

Figure 2.15 AFM images and line scan of a tip with a radius of 20µm. (a) Three dimensional topography, (b) a two dimensional image and (c) a line scan profile taken from “Line 1” in (b). The RMS roughness from the paraboloid was 0.3nm.

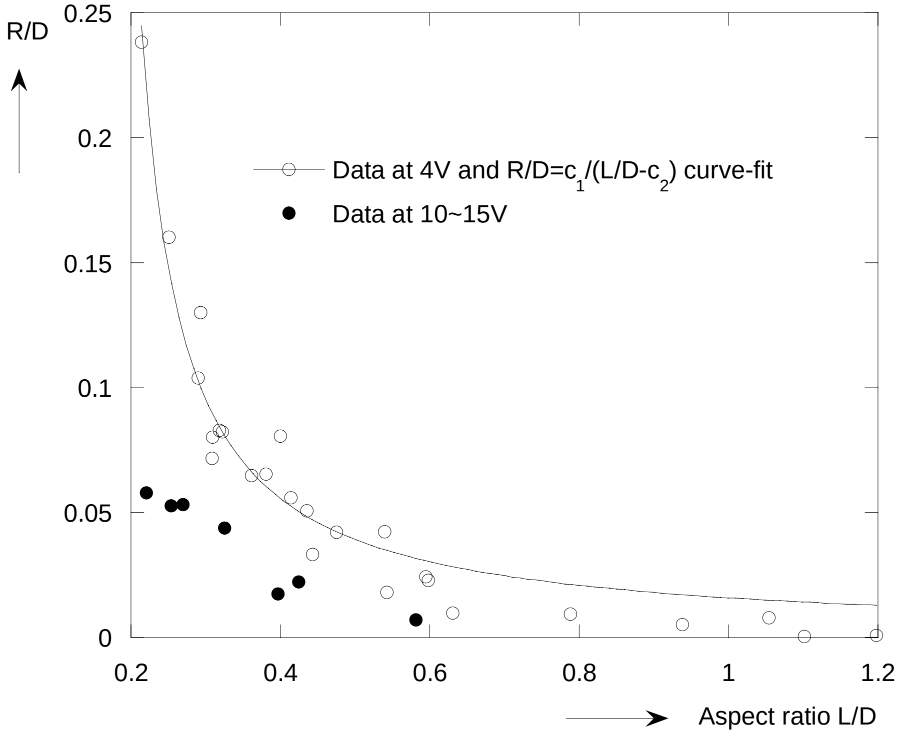

Figure 2.16 The variation of the dimensionless radius with the aspect ratio of tips formed at potentials of 4V and 10~15V.

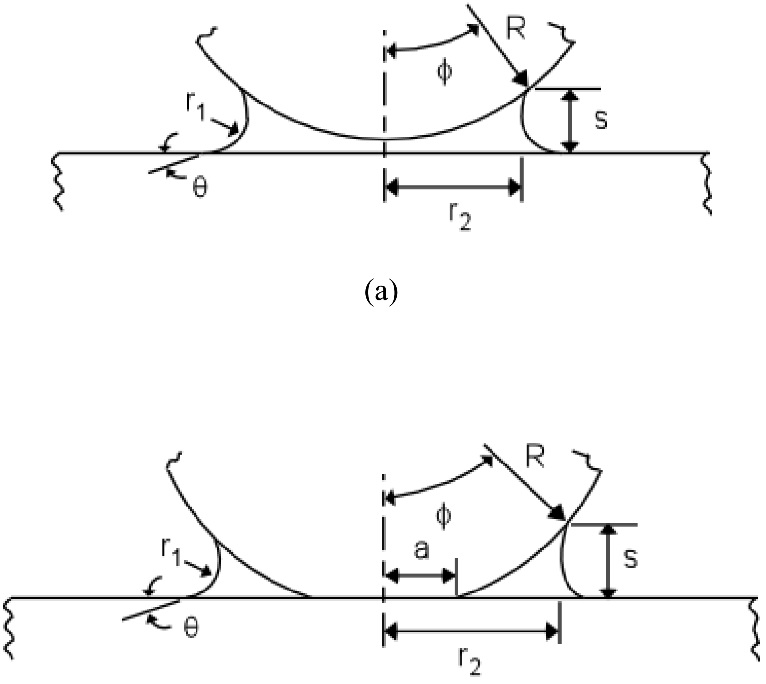

(a)

(b)

Figure 3.1 Schematic views of a condensed liquid between a sphere and a flat surface (a) before a contact and (b) under a contact.

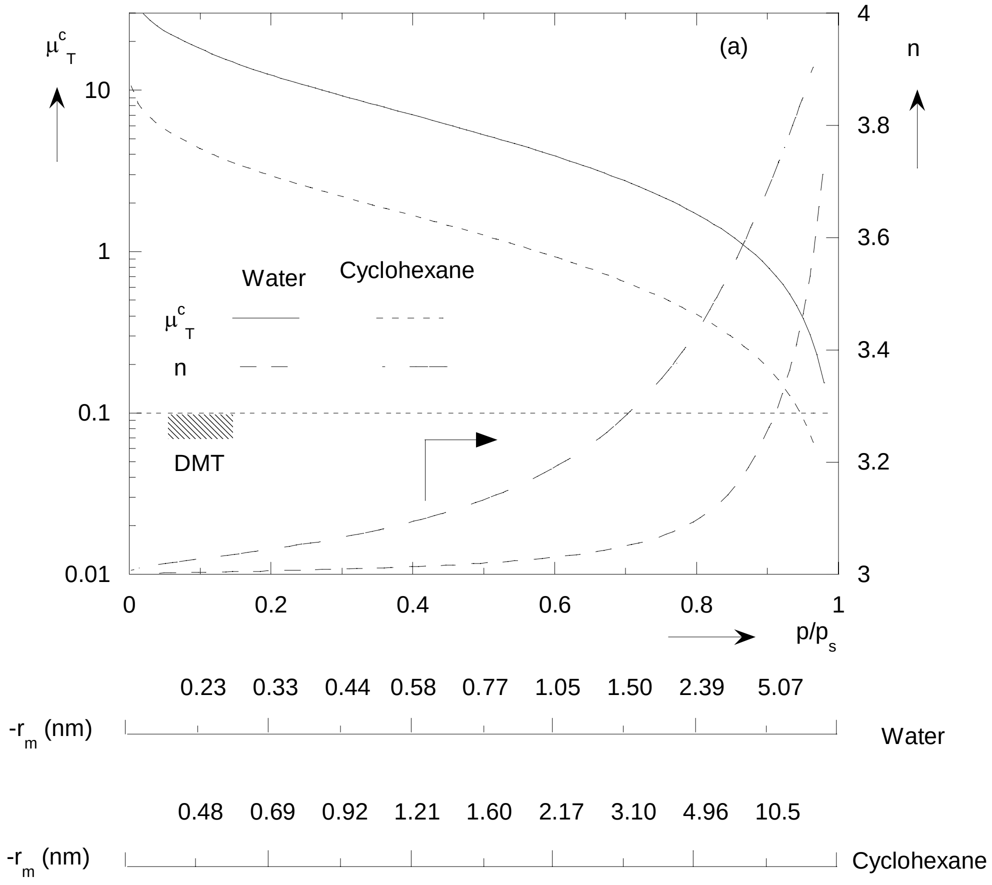

(a)
μ^c_T
10
1
0.1
0.01
n
4
3.8
3.6
3.4
3.2
3
Water
Cyclohexane
μ^c_T
n
DMT
0
0.2
0.4
0.6
0.8
1
p/p$_s$
0.23 0.33 0.44 0.58 0.77 1.05 1.50 2.39 5.07
-r$_m$ (nm)
Water
0.48 0.69 0.92 1.21 1.60 2.17 3.10 4.96 10.5
-r$_m$ (nm)
Cyclohexane

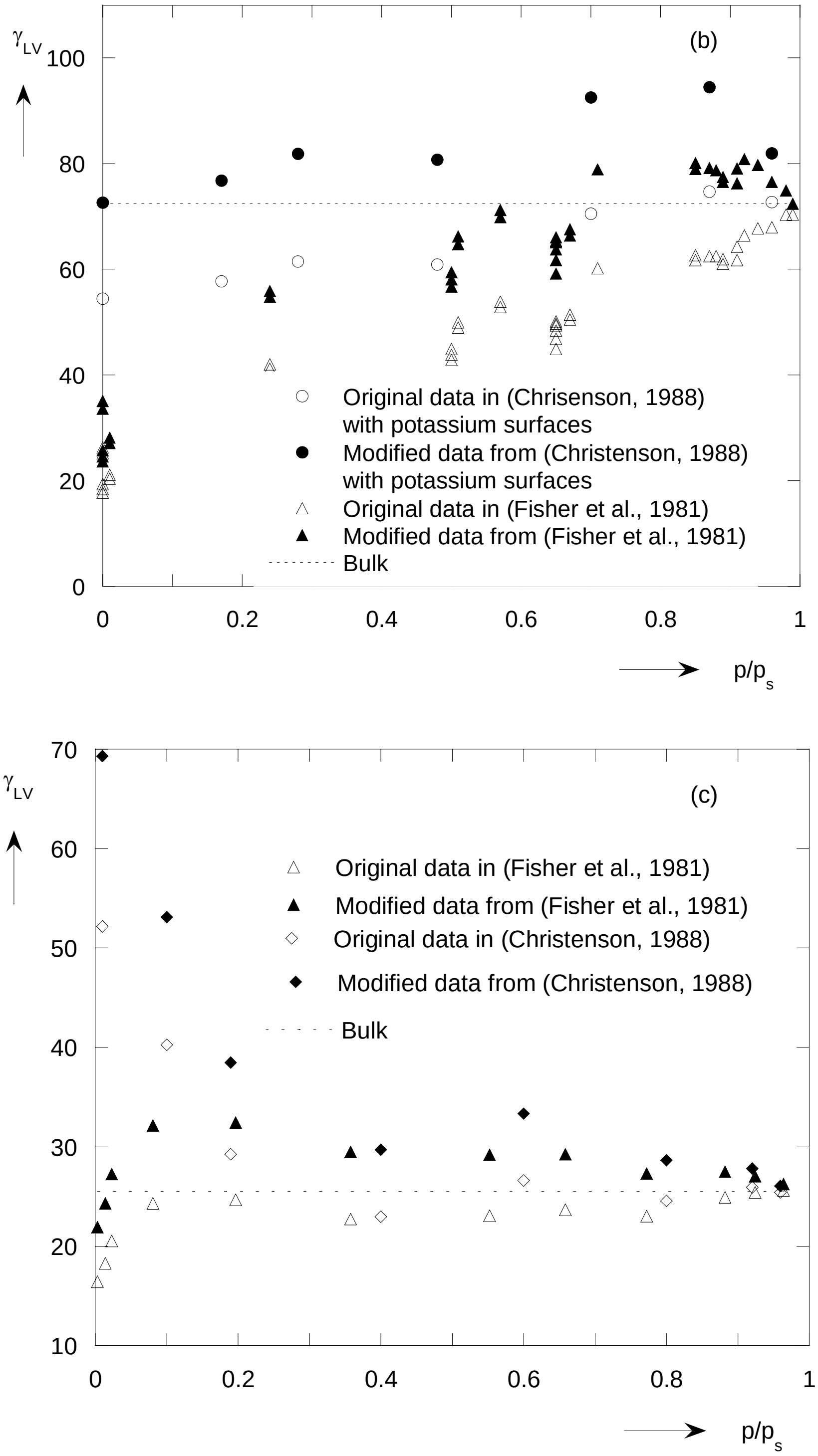

Figure 3.2 Reanalysis of data in (Fisher et al., 1981; Christenson, 1988). (a) The variation of μ_T^c and n with relative humidity and corresponding Kelvin radii and the original and updated data (modified with present interpretation) for water (b) and cyclohexane (c) based on n in (a).

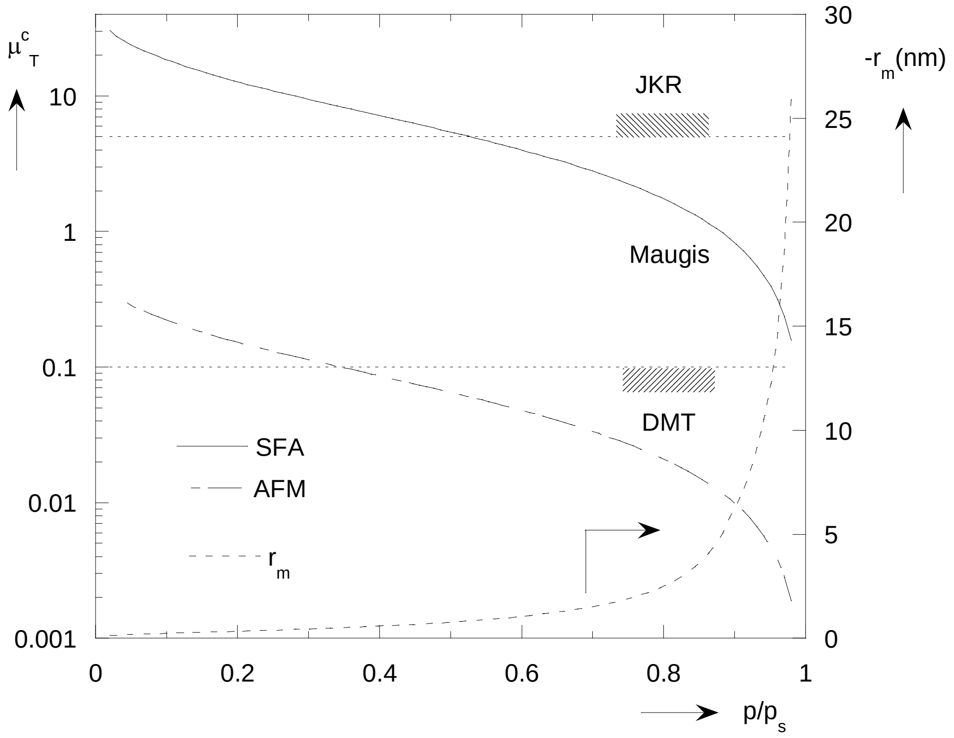

Figure 3.3 Guidelines for choosing contact mechanics models for SFA and AFM in humid environments. Two mica surfaces and a Si_3N_4 tip with a 100nm radius contacting on a mica surface are assumed for SFA and AFM, respectively. These guidelines are suggested to apply when the relative humidity level is above 40-50%.

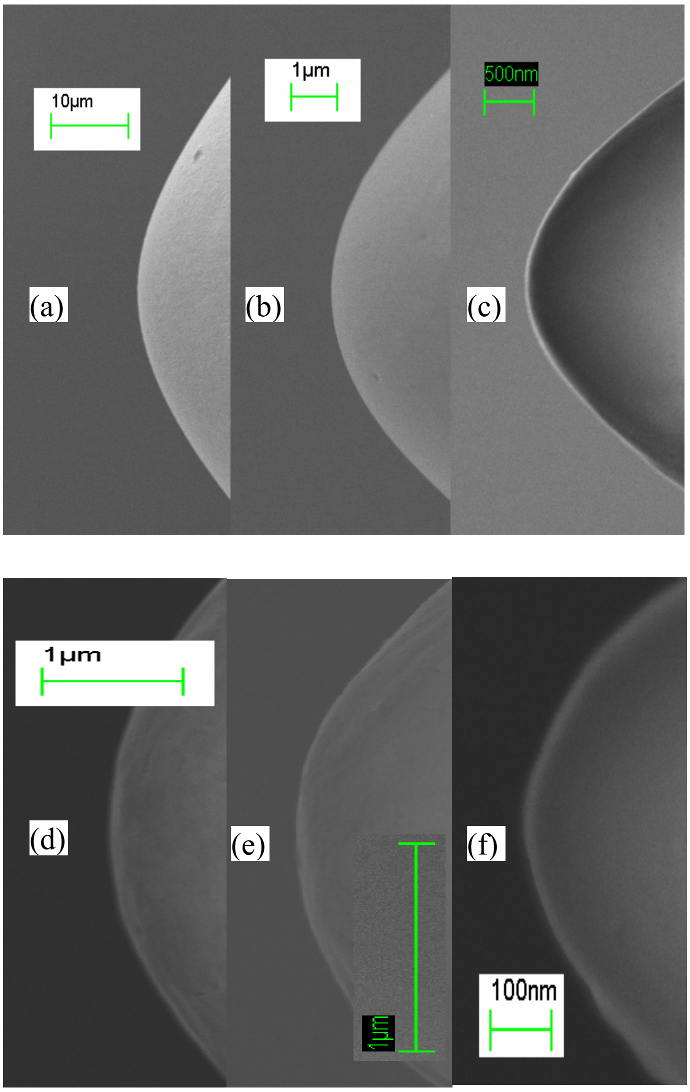

Figure 4.1 SEM images of probes used in friction experiments with radii of (a) 21.4µm, (b) 5.33µm, (c) 0.90µm, (d) 4.38µm, (e) 1.60µm and (f) 0.31µm.

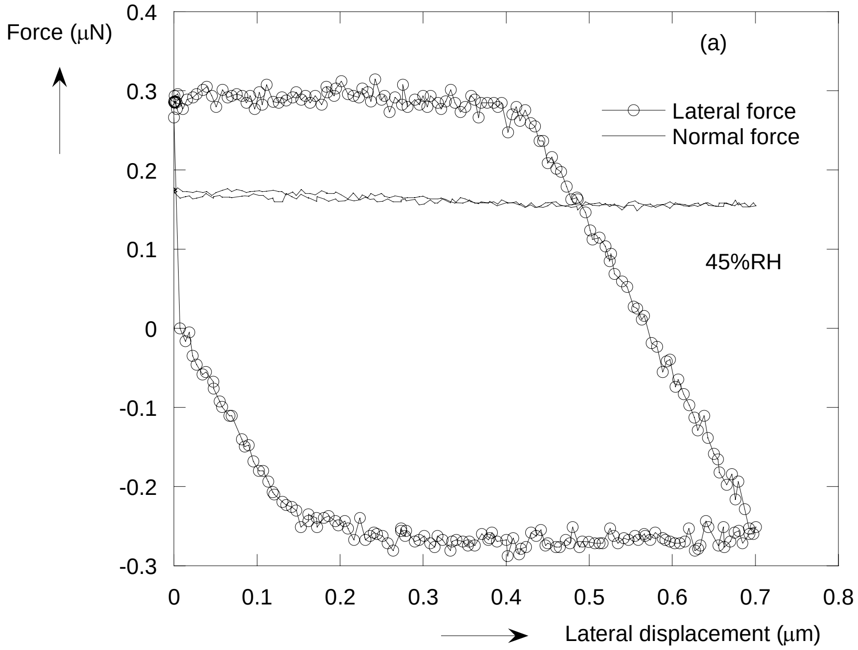

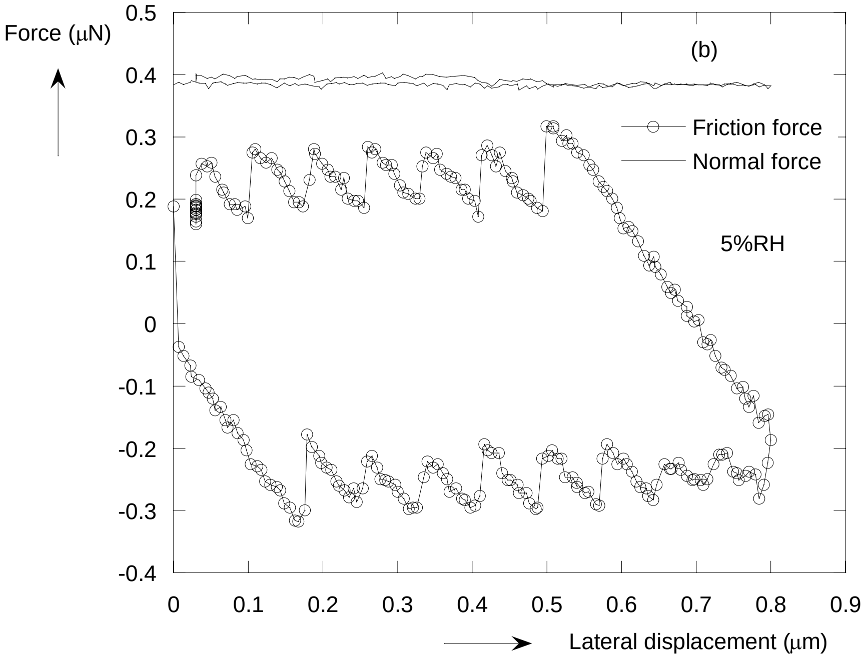

Figure 4.2 Friction and normal forces vs. lateral displacement and friction forces show (a) no stick-slip behavior in the ambient environment and (b) stick-slip behavior in the dry environment.

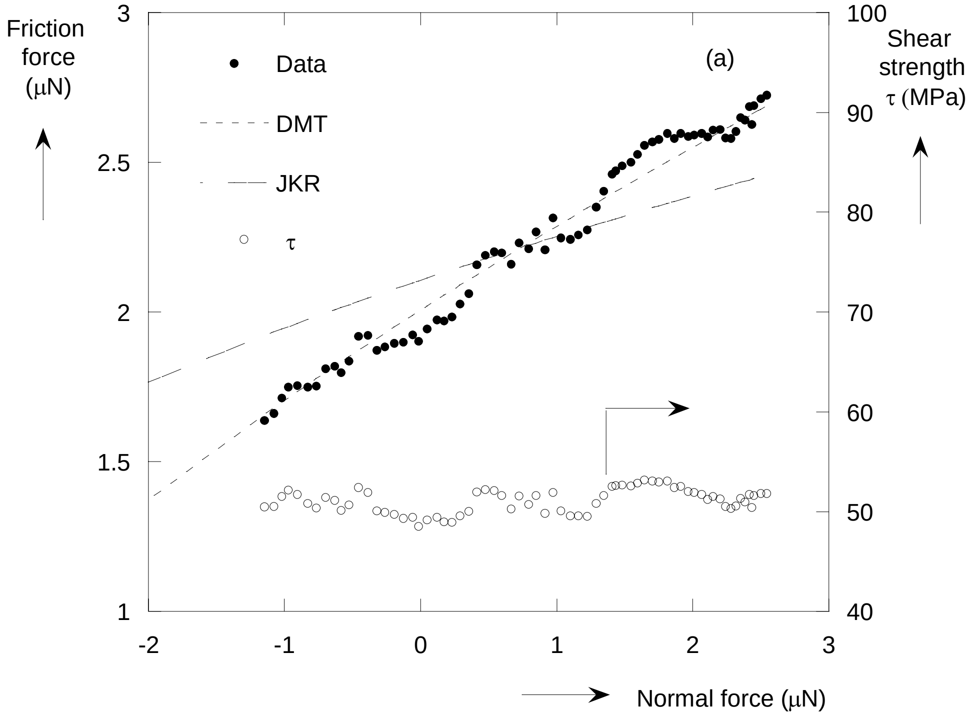
Friction force (μN)
3
2.5
2
1.5
1
-2
-1
0
1
2
3
Normal force (μN)
100
90
80
70
60
50
40
Shear strength τ (MPa)
(a)
Data
DMT
JKR
τ

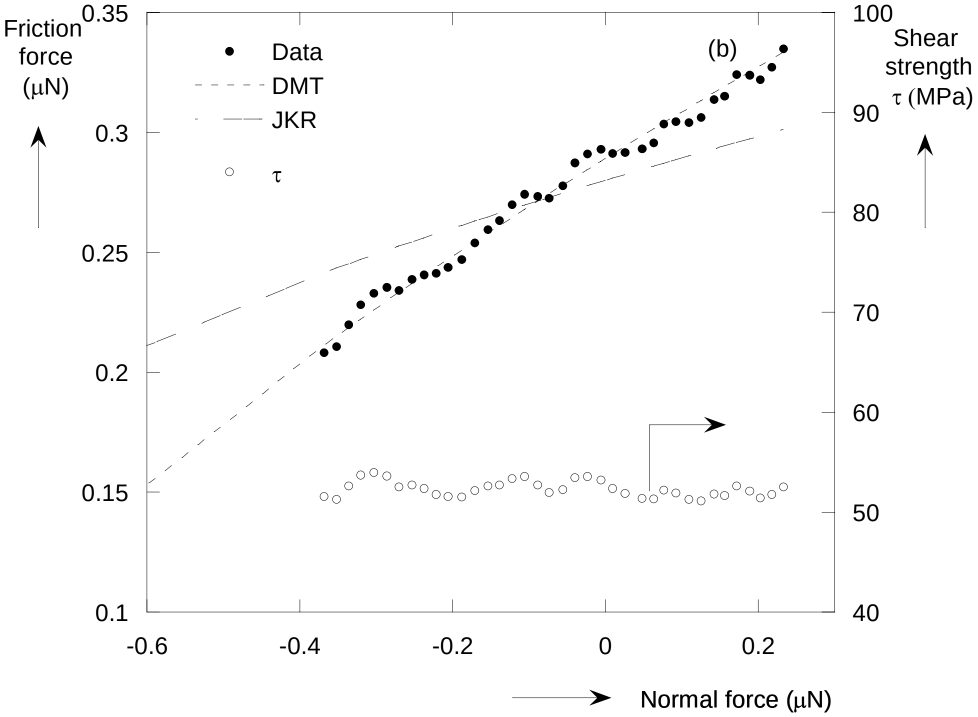
Friction force (μN)
0.35
0.3
0.25
0.2
0.15
0.1
-0.6
-0.4
-0.2
0
0.2
Normal force (μN)
100
90
80
70
60
50
40
Shear strength τ (MPa)
(b)
Data
DMT
JKR
τ

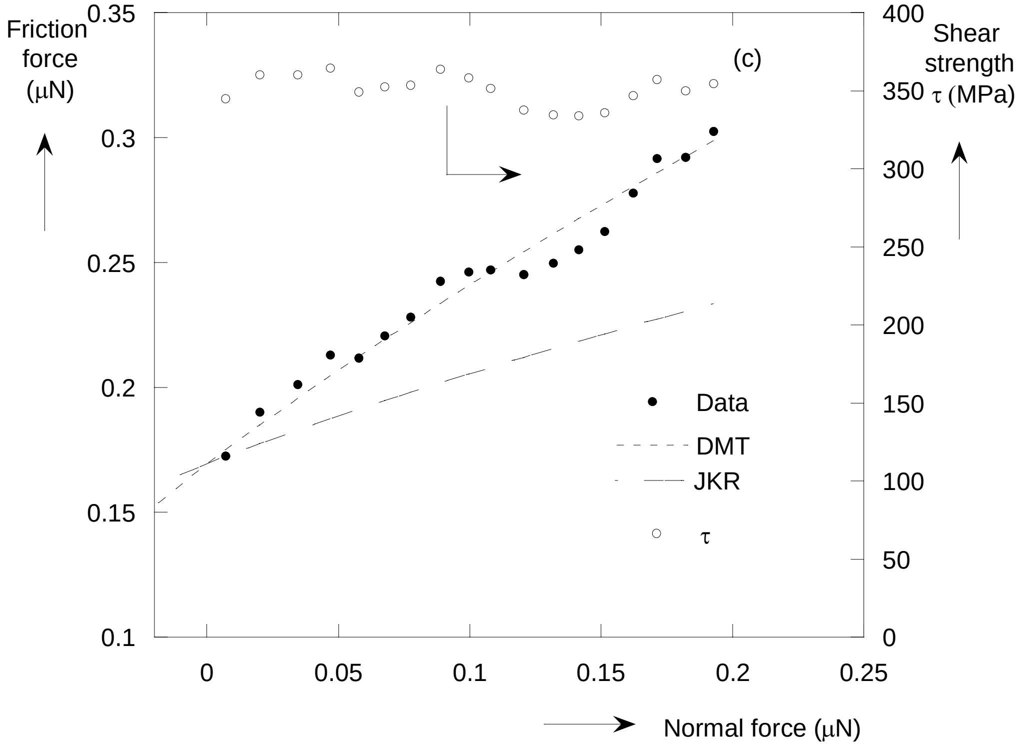

Figure 4.3 The variation of friction force with normal force in the ambient environment (45% RH) using probes with diameters of (a) 21.4μm, (b) 5.33μm and (c) 0.90μm, respectively. The shear strengths shown result from the contact mechanics model that was consistent with data.

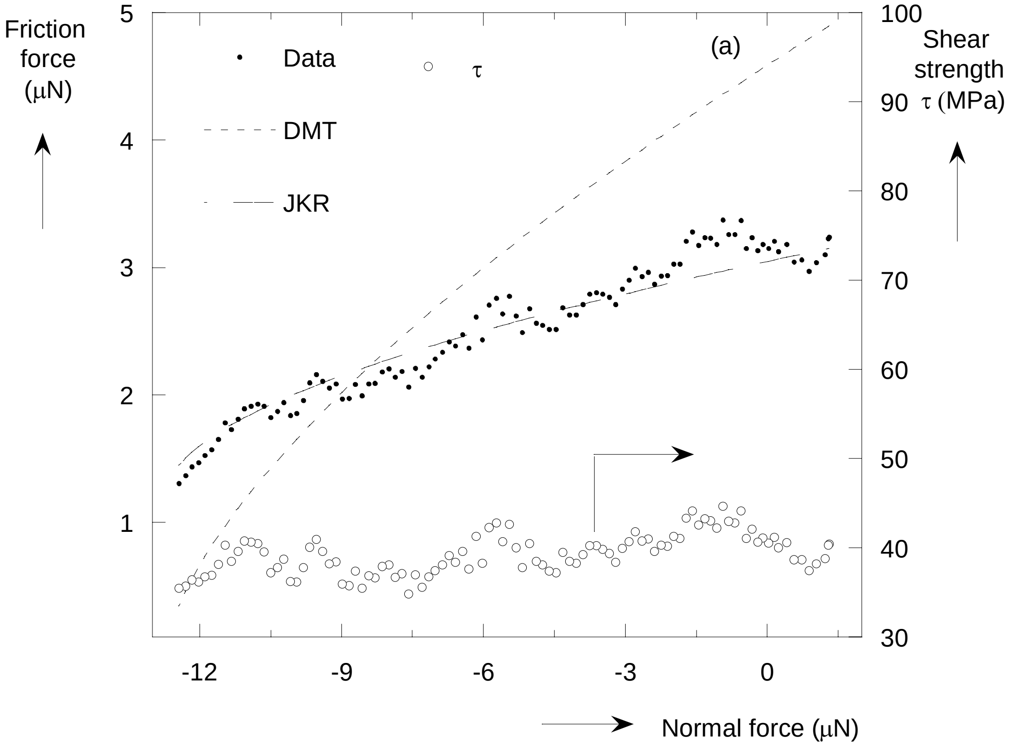
Friction force (μN)
Shear strength τ (MPa)
(a)
Data
τ
DMT
JKR
Normal force (μN)
5
4
3
2
1
100
90
80
70
60
50
40
30
-12
-9
-6
-3
0

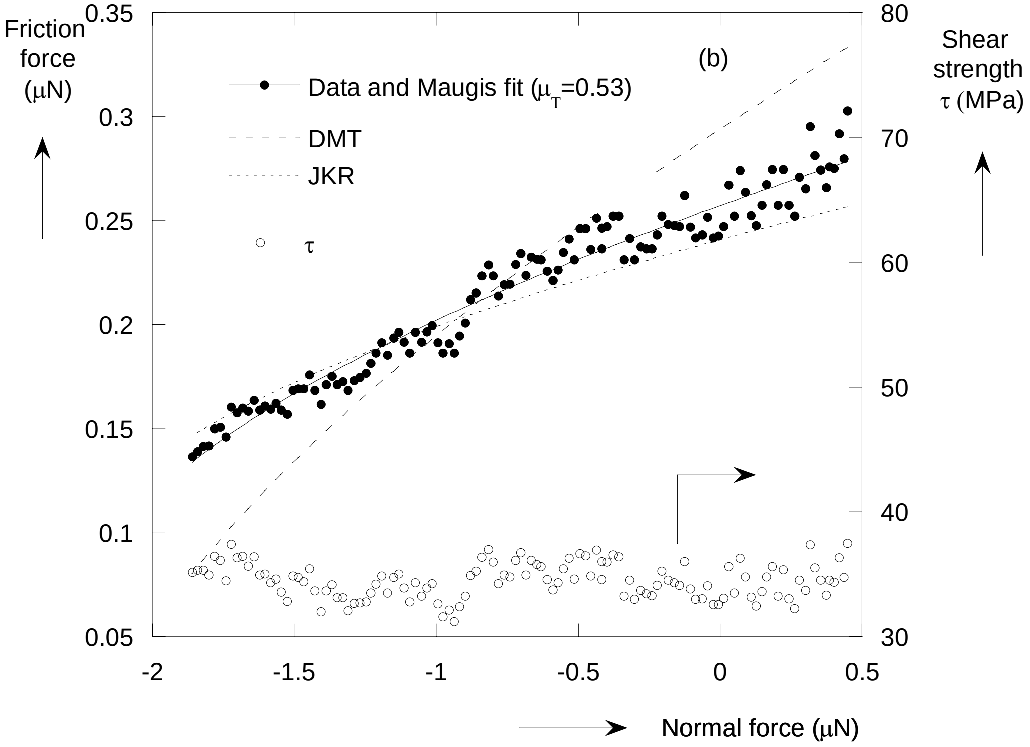
Friction force (μN)
Shear strength τ (MPa)
(b)
Data and Maugis fit (μ_T=0.53)
DMT
JKR
τ
Normal force (μN)
0.35
0.3
0.25
0.2
0.15
0.1
0.05
80
70
60
50
40
30
-2
-1.5
-1
-0.5
0
0.5

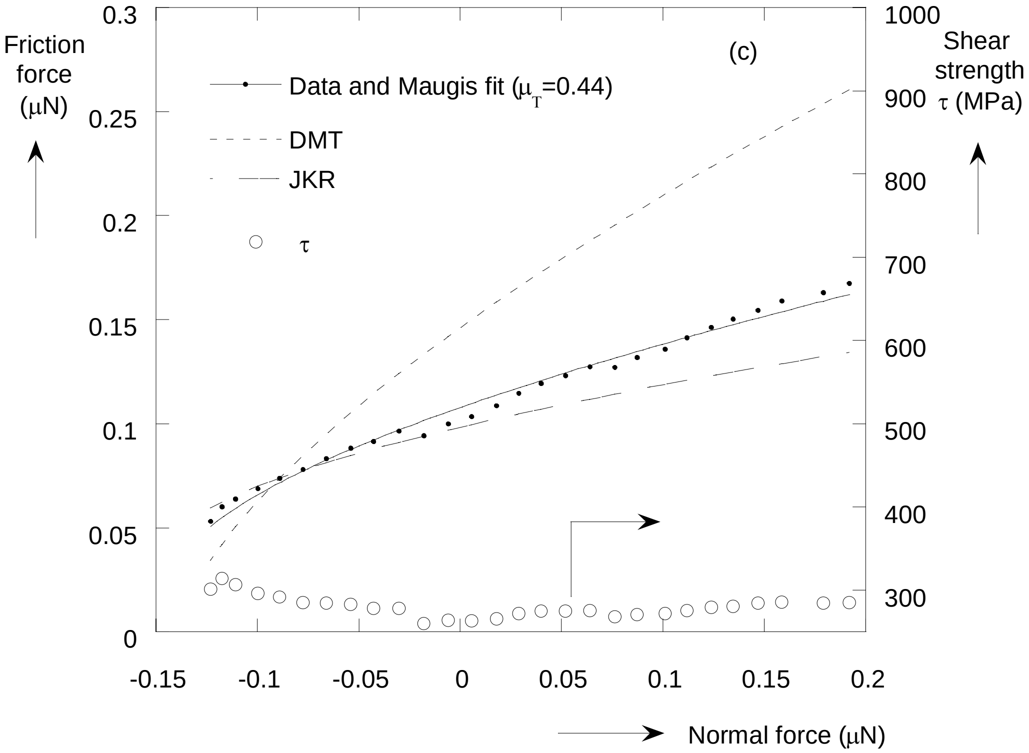

Figure 4.4 The variation of friction force with normal force in the dry environment (5% RH) using probes with diameters of (a) 4.38μm, (b) 1.60μm and (c) 0.31μm, respectively. The shear strengths shown result from the contact mechanics model that was consistent with data.

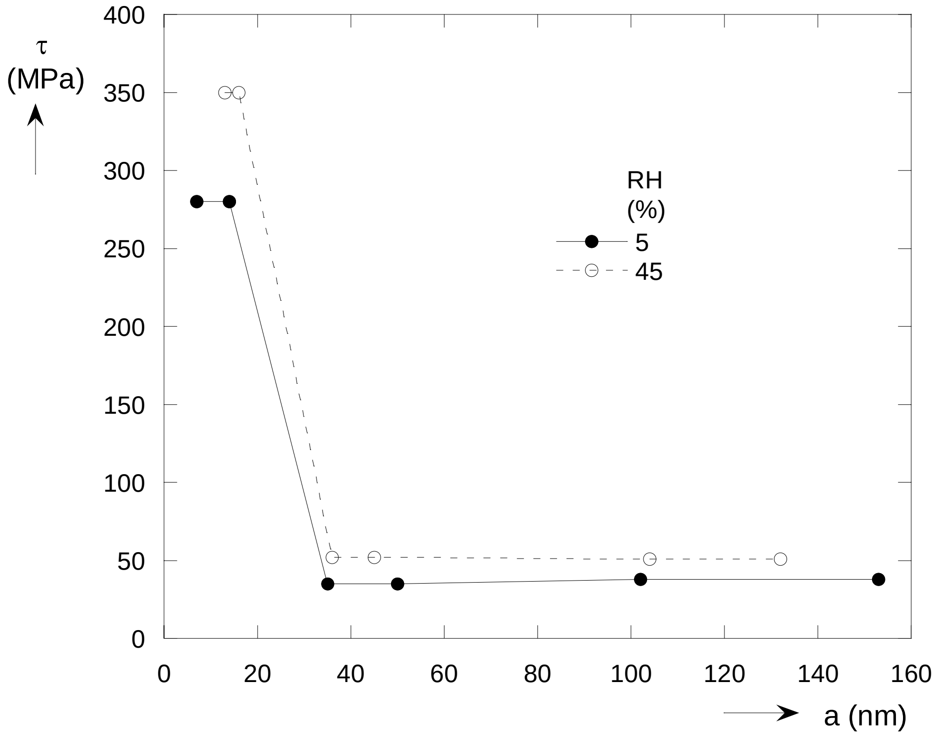

Figure 4.5 The variation of shear strength with contact radius in both the ambient and dry environments.

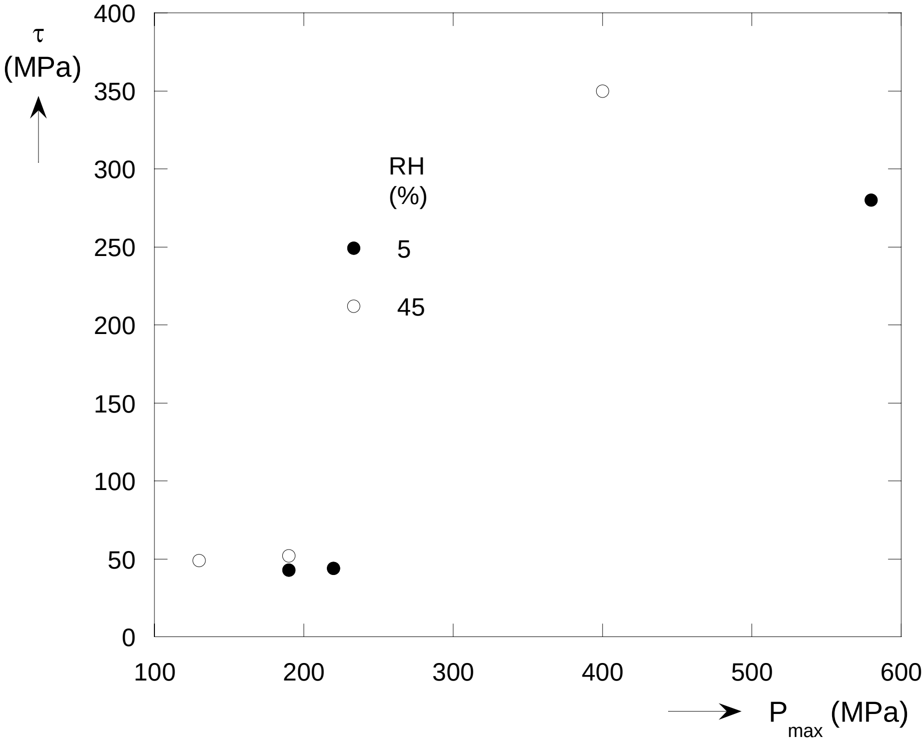

Figure 4.6 The variation of shear strength with the maximum normal pressure in both ambient and dry environments.

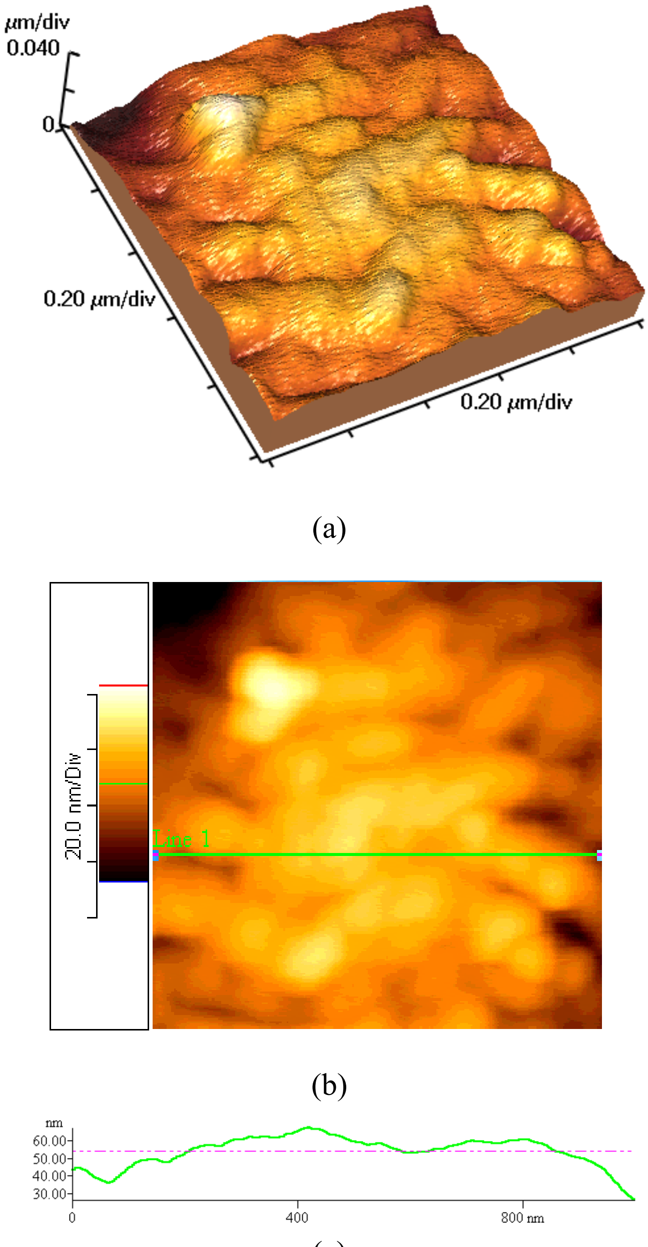

Figure 4.7 AFM images and line scan of the tip with a radius of 5.33μm after two scans under a normal load of 5μN. (a) Three dimensional topography, (b) a two dimensional image and (c) a line scan profile taken from “Line 1” in (b). The RMS roughness from the paraboloid was 5nm. The surface roughness is 0.3nm before the scanning.

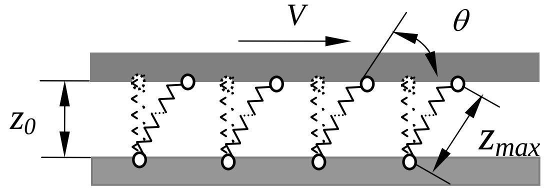

Figure 4.8 A schematic of the friction model. The springs with dashed lines represent the initial positions of attractive bonds to cause friction. The ones with solid lines show the positions of such bonds at rupture resulting from a quasi-static relative movement.

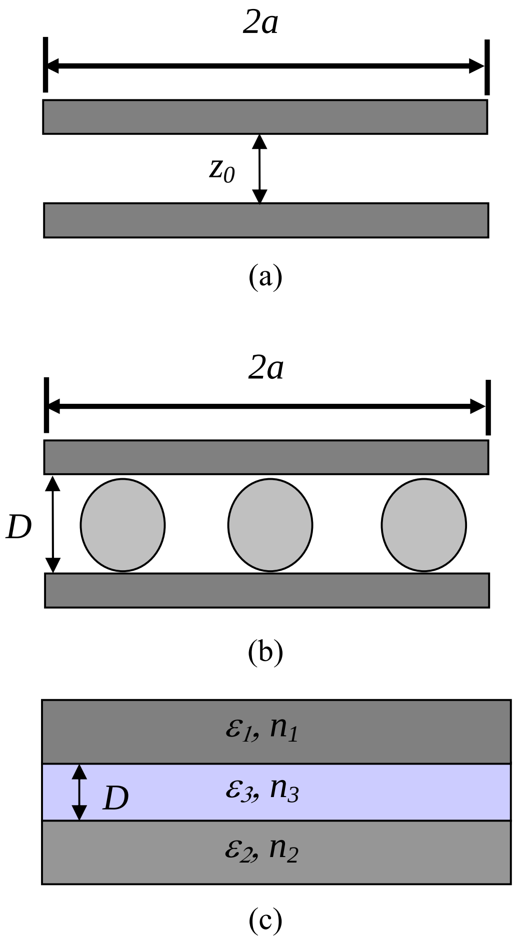

Figure 4.9 Illustrations of (a) intimate contact, (b) separated contact of one layer of interfacial molecules separated contact and (c) the continuum description of two sliding surfaces and interfacial medium for the Lifshitz theory, where ε_i and n_i represent the dielectric constant and refractive index of each medium. $\varepsilon_3 = n_3 = 1$ if there are no interfacial molecules.

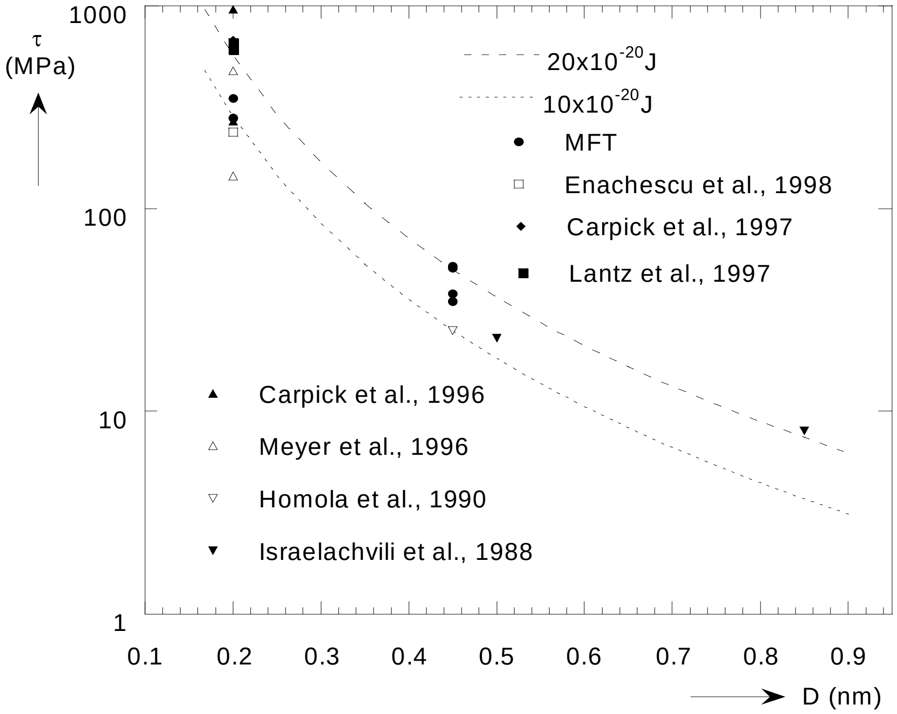

Figure 4.10 The variation of the shear strength obtained from current and both previous AFM and SFA experiments with separation between two sliding surfaces inside the contact zone.

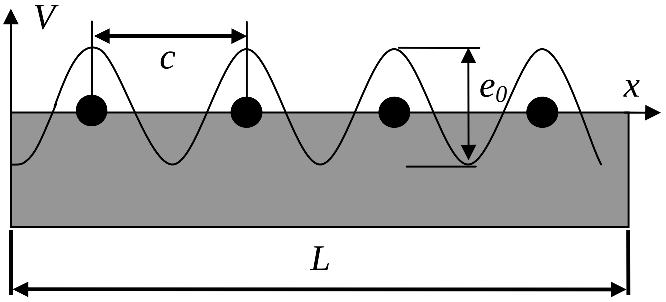

Figure 4.11 A schematic of a one-dimensional periodic surface potential field with amplitude e_0 and lattice constant c.

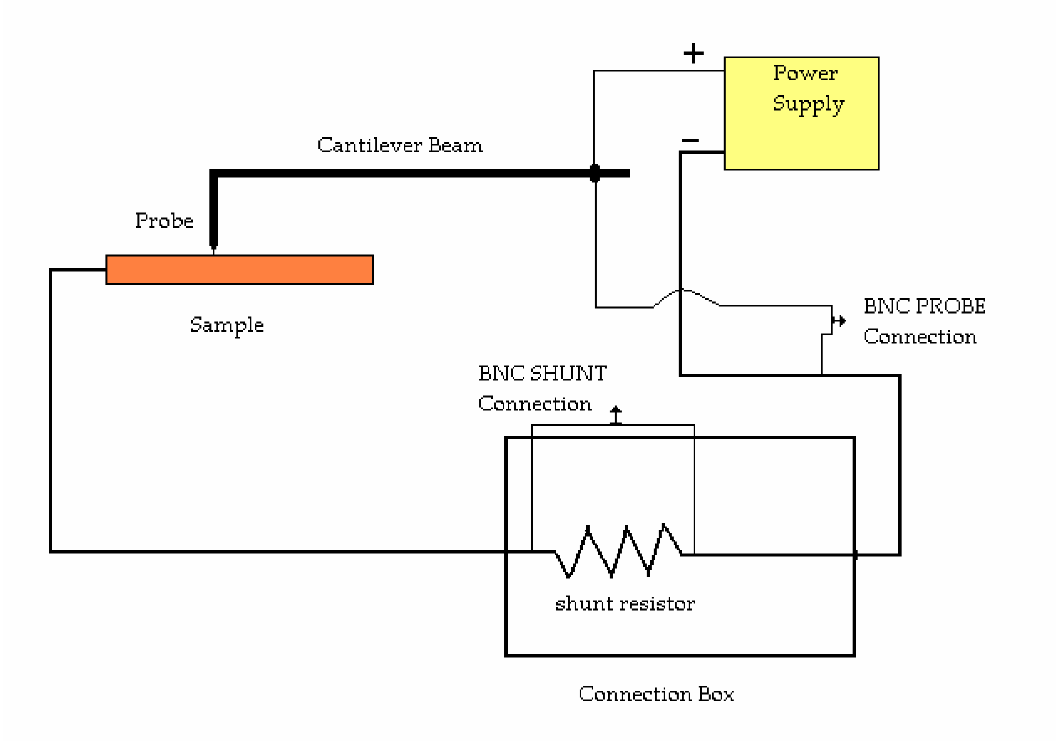

Figure 5.1 A schematic of circuit adjunct to the MFT.

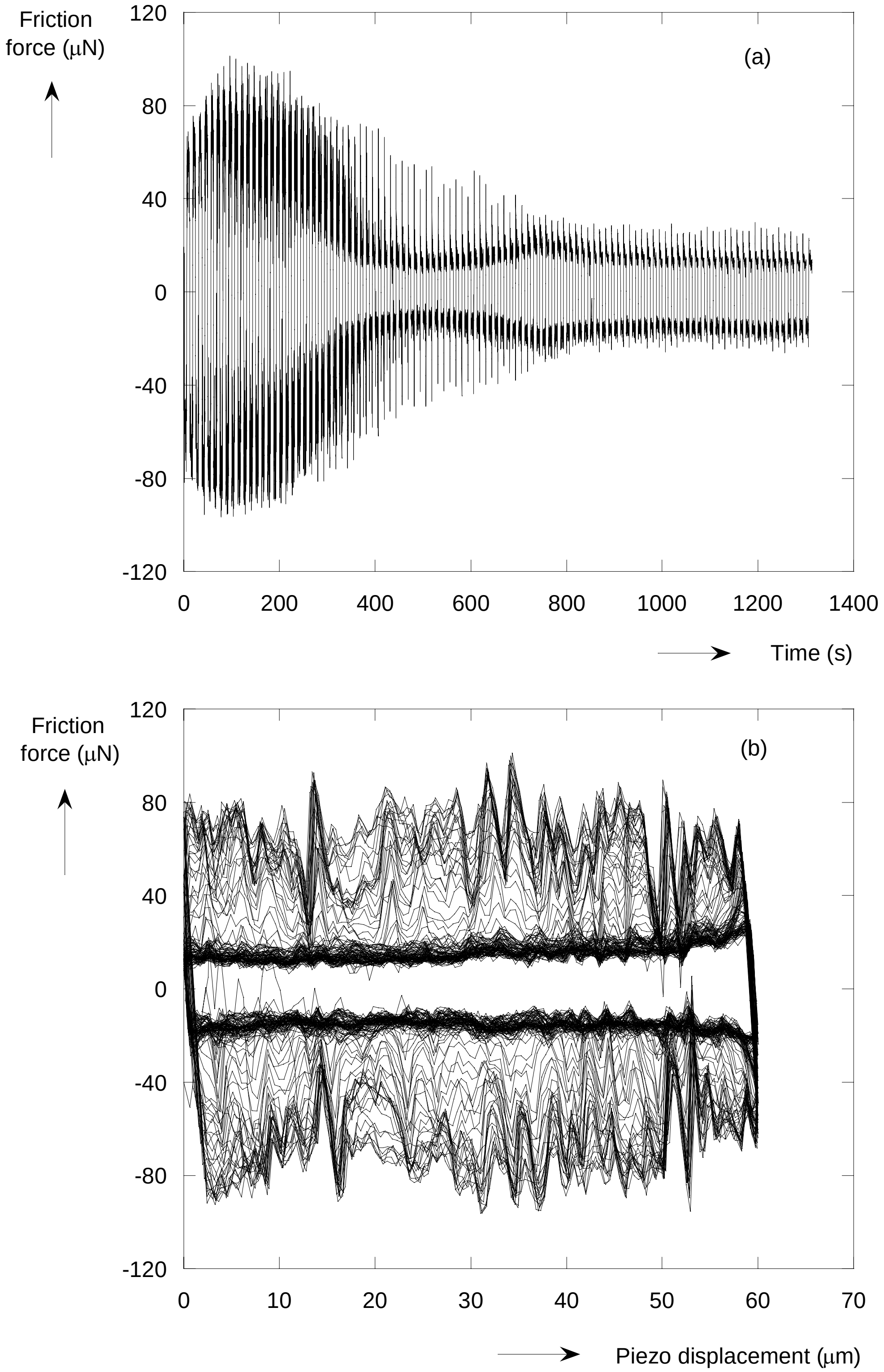

Figure 5.2 The variation of friction force with (a) time and (b) the lateral displacement of the piezo stage in 100 repeated scans without current. The normal force was about 30μN.

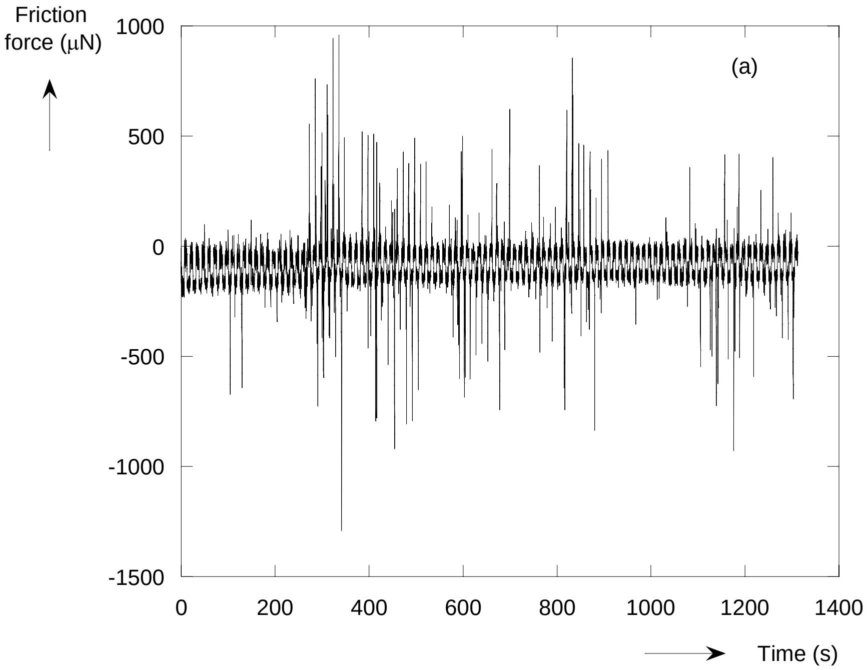
Friction force (μN)
1000
500
0
-500
-1000
-1500
(a)
0
200
400
600
800
1000
1200
1400
Time (s)

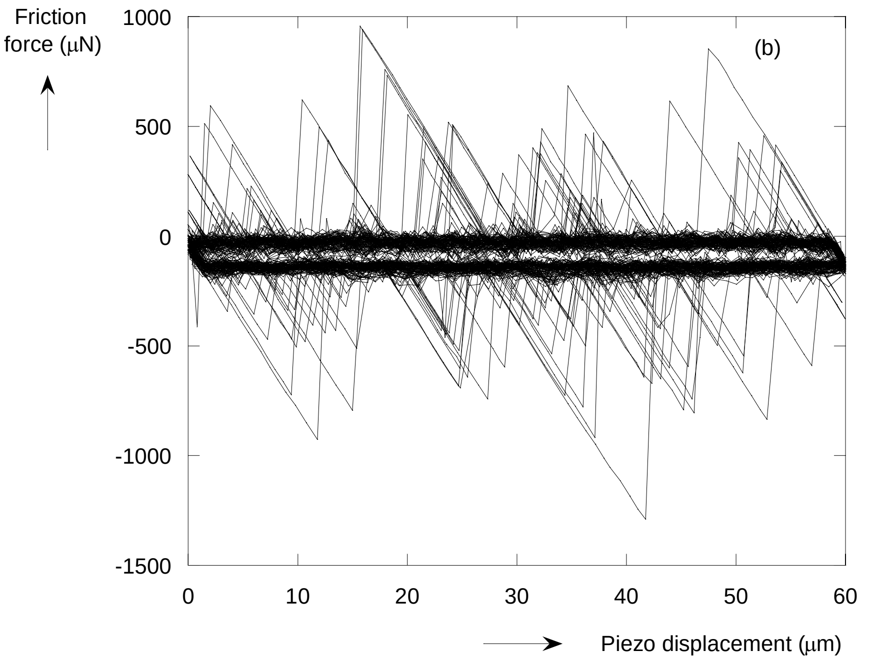
Friction force (μN)
1000
500
0
-500
-1000
-1500
(b)
0
10
20
30
40
50
60
Piezo displacement (μm)

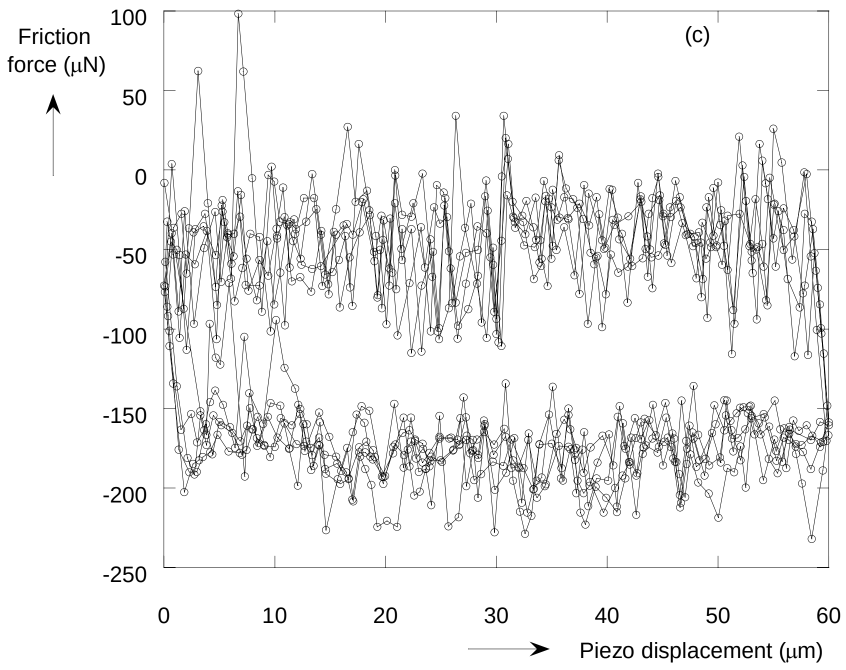

Friction
force (μN)
100
50
0
-50
-100
-150
-200
-250
(c)
0
10
20
30
40
50
60
Piezo displacement (μm)

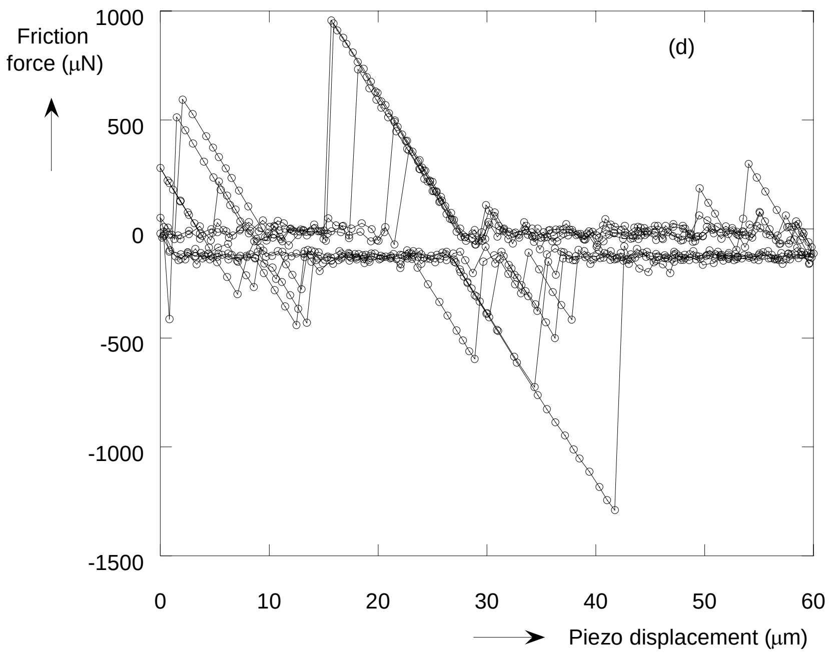

Friction
force (μN)
1000
500
0
-500
-1000
-1500
(d)
0
10
20
30
40
50
60
Piezo displacement (μm)

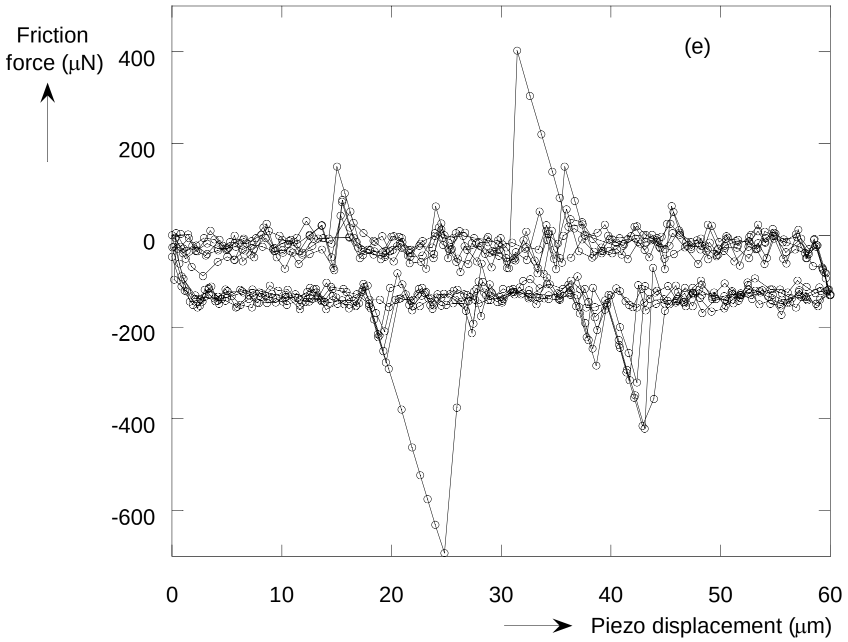

Figure 5.3 The variation of friction force with (a) time and (b) the lateral displacement of the piezo stage in 100 repeated scans with a current of 0.1A. The variation of friction force with the lateral displacement during scans of 1st to 5th, 26th to 30th, 96th to 100th are shown in (c), (d) and (e), respectively.

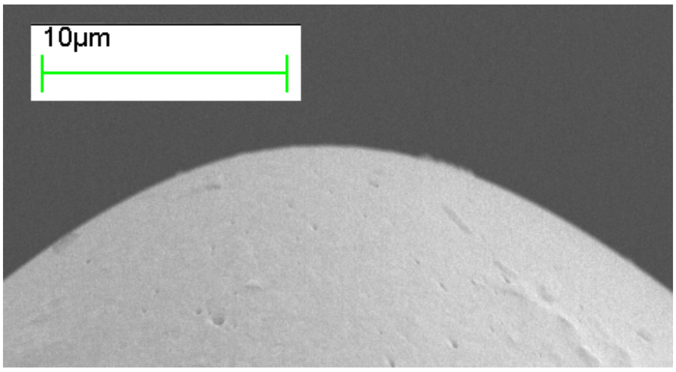

(a)

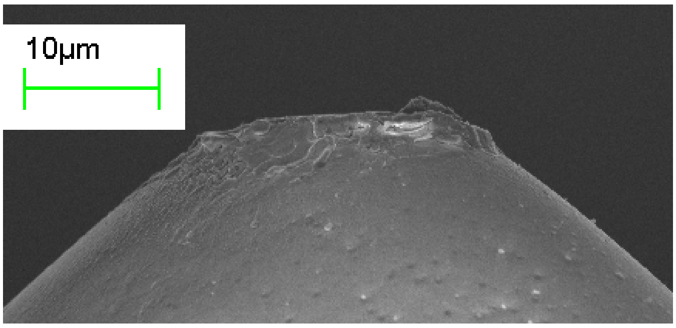

(b)

Figure 5.4 SEM pictures of the probe used in friction experiments with current (a) before and (b) after the scanning.

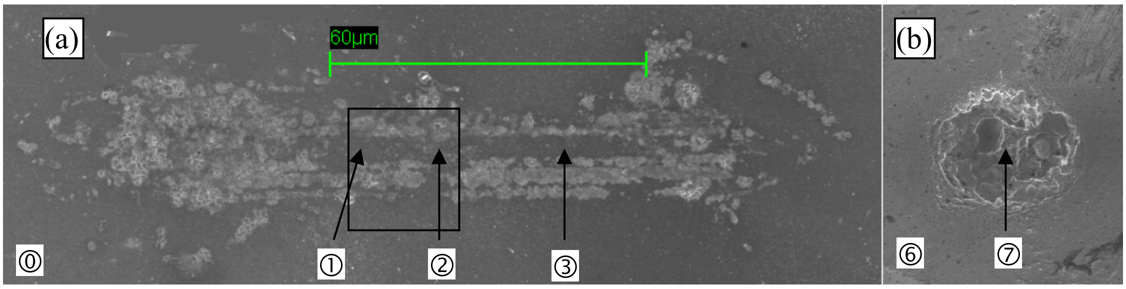

Figure 5.5 (a) A SEM image of the repeatedly scanned track and (b) a top view of the worn probe. They were taken at the same magnitude of magnification.

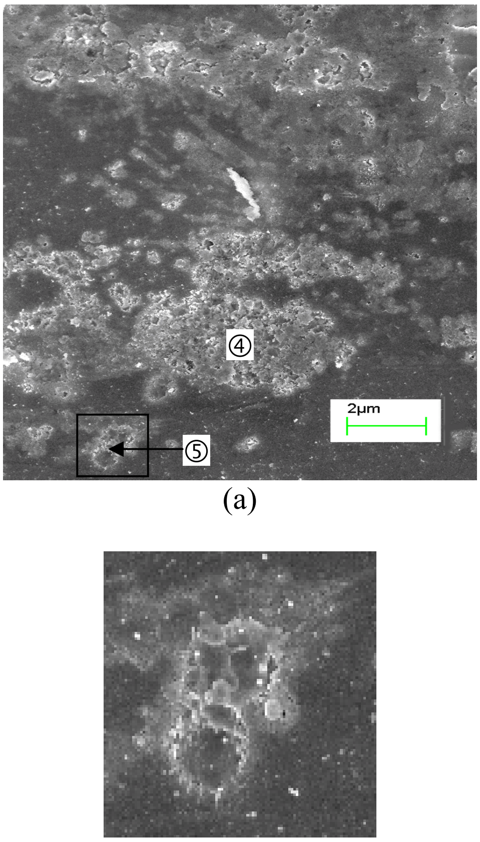

(a)

(b)

Figure 5.6 (a) The image at high magnification of the area approximately shown in the rectangle in Figure 5.5a and (b) a close-up of the circular feature shown inside the rectangle area in (a).

Figure 5.7 An image of polished and etched copper sample at 200×.

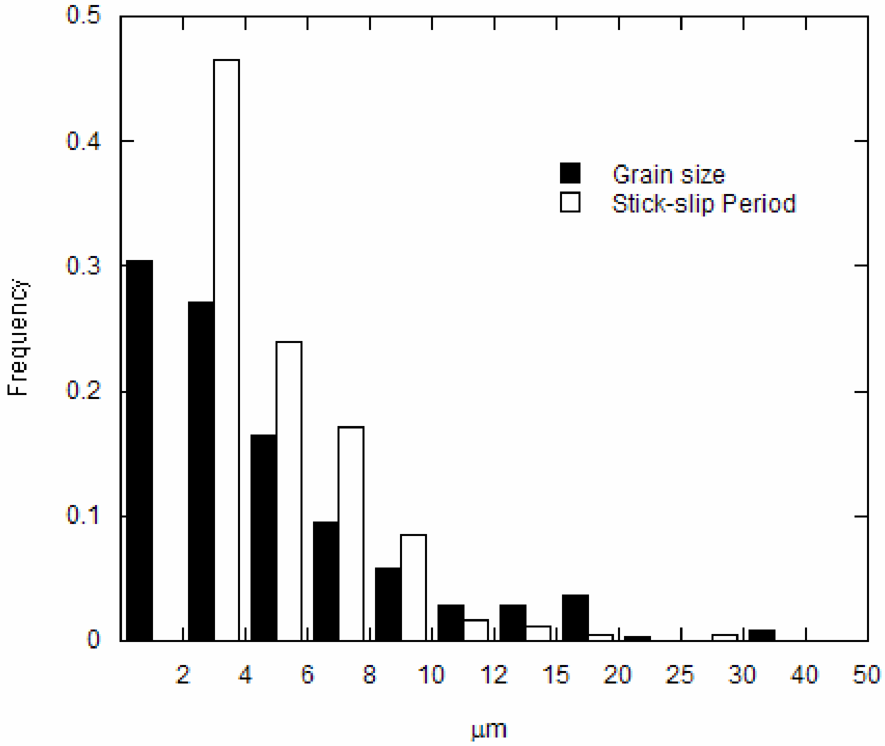

Figure 5.8 The histograms of the grain size and the stick-slip period.

Appendix A

Van der Waals Force

Adhesion is the origin of friction. As a matter of fact, adhesion originates from intermolecular forces. Intermolecular forces are generally classified into two categories: chemical forces (intramolecular forces) and physical forces (Israelachvili, 1992b). The former binds the atoms together within the molecule when two or more atoms come together to form a molecule. The latter interacts between unbonded discrete atoms and molecules and usually lacks the specificity, stoichiometry and directionality.

Cohesion is understood to be the interaction between molecules within a single body whereas adhesion is often defined as the interaction between two unlike contiguous bodies (phases) (Zimon, 1982) and can be regarded as a state of minimum energy that is attained when two solids are brought into contact (Scherge and Gorb, 2001). The classification between cohesion and adhesion is not fundamental. Cohesion can originate from chemical forces as well as physical forces. For example, cohesion for thermoplastic polymers is from van der Waals interaction determined by physical forces. Nevertheless, adhesion exclusively originates from physical forces. According to this classification, fracture is more related to cohesion and hence friction between two solid bodies depends more upon adhesion.

The Van der Waals force is regarded as the most common adhesion force. The contents in the following of this section refer to two books (Israelachvili, 1992b; Butt, 2006). There are three contributions: dipole to dipole (oriented); dipole to induced dipole (induced) and induced-dipole to induced-dipole (dispersion) to the total attractive van der Waals interaction between molecule A and molecule B

$$W_{AB} = -(C_{orient} + C_{induced} + C_{dispersion}) / d^6 = -C_{total} / d^6 \tag{A1}$$

where, C_{orient}, $C_{induced}$ and $C_{dispersion}$ represent the coefficients from three corresponding contributions: dipole-dipole, dipole-polarisable molecule and nonpolar molecule-nonpolar molecule interactions, respectively, C_{total} is the total coefficient and d is the separation. With the assumption of pairwise additivity, the net van der Waals energy per unit area between two infinite surfaces made up of molecules A and B is the sum of interactions with all the molecules in two bodies and expressed as (Israelachvili, 1992b)

$$w = -\frac{\pi^2 C_{total} \rho_A \rho_B}{12d^2} \tag{A2}$$

where ρ_A and ρ_B are the molecular densities for surface A and B, respectively. The conventional Hamaker constant (Hamaker, 1937) is defined as

$$A = \pi^2 C_{total} \rho_A \rho_B, \tag{A3}$$

which is independent of geometries of surface A and B. Thus, the normal adhesion pressure is

$$\sigma = \frac{\partial w}{\partial d} = \frac{A}{6d^3} \tag{A4}$$

Note that the coefficient C_{total} is roughly proportional to the square of the polarizability of molecule A and B, which in turn is roughly inversely proportional to the molecular densities and consequently the Hamaker constant A is roughly constant although it is a gross oversimplification. Nevertheless, the Hamaker constants of most condensed phases are found to lie in the range (0.4~4)×10^{-19}J (Israelachvili, 1992b).

However, the assumption of pairwise additivity ignores the influence of neighbouring atoms on the interaction between any pair of atoms. Furthmore, this additivity breaks down when two surfaces are separated by another medium. The problem of additivity is completely avoided in Lifshitz theory where the atomic structure is ignored and the forces between large bodies, now treated as continous media, are derived in terms of such bulk properties as their dielectric constants and refractive indices (Israelachvili, 1992b). It turns out that all the conclusions based on the assumption of additivity remain valid and the only thing that changes is the way the Hamaker contact is calculated. For a material 1 interacting with material 2 across a medium 3, the Hamaker constant is approximately (within ~5% accuracy) (Israelachvili, 1992b)

$$A = \frac{3}{4} k_B T \cdot \left(\frac{\varepsilon_1 - \varepsilon_3}{\varepsilon_1 + \varepsilon_3} \right) \cdot \left(\frac{\varepsilon_2 - \varepsilon_3}{\varepsilon_2 + \varepsilon_3} \right) + \frac{3h}{4\pi} \cdot \int_{\nu_1}^{\infty} \left(\frac{\varepsilon_1(i\nu) - \varepsilon_3(i\nu)}{\varepsilon_1(i\nu) + \varepsilon_3(i\nu)} \right) \cdot \left(\frac{\varepsilon_2(i\nu) - \varepsilon_3(i\nu)}{\varepsilon_2(i\nu) + \varepsilon_3(i\nu)} \right) d\nu \tag{A5}$$

where, k_B is the Boltzmann constant, T is the absolute temperature, h is Planck constant, ε_1, ε_2 and ε_3 are the static permittivities of the three media, $\varepsilon_1(i\nu)$, $\varepsilon_2(i\nu)$ and

$\varepsilon_3(i\nu)$ are the permittivities at imaginary frequencies $i\nu$ and $\nu_1 = 2\pi k_B T / h = 3.9\times10^{13}$ Hz at 300K.

Appendix B

Capillary Force

Provided that different adhesion mechanisms combine independently, the adhesion force F in the presence of an annulus of pure liquid (Fig. 3.1) may be written as (Fisher and Israelachvili, 1981)

$$F = F_{cap}(\Delta p) + F_{vdw}(d) + F_{ten}(\gamma_{LV}) + F_{others} \tag{B1}$$

where $F_{cap}(\Delta p)$ is the capillary force due to the Laplace pressure Δp; $F_{vdw}(d)$ is the force due to direct solid-solid adhesion or van der Waals interaction with the minimum separation d between surfaces; $F_{ten}(\gamma_{LV})$ is the force due to the liquid/vapor surface tension γ_{LV}; other interactions F_{others}, such as electrostatic (Schonenberger and Alvarado, 1990) and magnetic forces (Martin and Wickramasinghe, 1987) may be considered.

As shown in Fig. 3.1, r_1 and r_2 are approximately the two principal radii, θ is the solid/liquid contact angle, ϕ is the half of the angle corresponding to the liquid annulus arc and $s = 2r_m$ is a measure of the capillary force range. The pressure difference across the interface between the condensed liquid and vapor is given by the Young-Laplace equation (Adamson, 1990)

$$\Delta p = \gamma_{LV}\left(\frac{1}{r_1} + \frac{1}{r_2}\right) = \frac{\gamma_{LV}}{r_m}, \tag{B2}$$

where, r_m is the mean radius of the meniscus. Note that r_m is negative ($\Delta p < 0$). Furthermore the mean radius is given by the Kelvin equation (Adamson, 1990)

$$\frac{\gamma_{LV}}{r_m} = \frac{R_c T}{V} \ln \frac{p}{p_s}, \tag{B3}$$

where R_c is the universal gas constant, T is the absolute temperature, V is the molar volume and p and p_s are the equilibrium and saturation vapor pressures of the liquid, respectively.

In most cases of practical importance, when a capillary bridge has been formed but the surfaces are not in contact (Fig. 3.1a), $R >> r_2 >> r_1$ and θ and $\phi \approx 0$, making r_m approximately r_1 and simplifying the capillary force to

$$F_{cap}(\Delta p) = 4\pi R\gamma_{LV}. \tag{B4}$$

This equation also applies when the surfaces have made contact (Fig. 3.1b). This can be seen by noting that $2Rs = r_2^2 - a^2$ and $F_{cap}(\Delta p) = \Delta p\pi(r_2^2 - a^2) = 4\pi R\gamma_{LV}$.

The force due to the liquid/vapor surface tension is given by

$$F_{ten}(\gamma_{LV}) = 2\pi R\gamma_{LV}\sin\phi\sin(\theta+\phi) \approx 0. \tag{B5}$$

For a Derjaguin approximation (rigid bodies) the solid-solid interaction is given as

$$F_{vdw}(d) = \frac{AR}{6d^2} = 4\pi R\gamma_{SL}, \tag{B6}$$

where A is the Hamaker constant in a liquid and d is the minimum distance between the sphere and the surface. The ratio between $F_{cap}(\Delta p)$ and $F_{vdw}(d)$ is

$$\frac{F_{cap}(\Delta p)}{F_{vdw}(d)} = \frac{24\pi\gamma_{LV}d^2}{A}. \tag{B7}$$

Substituting γ_{LV}=72.5mJ/m^2, $A = 10^{-20}$J (Israelachvili, 1992b) (smaller in liquid than in vacuum or air) and $d = 0.3$nm (Horn et al., 1987) into Eq. (B7), the ratio is about 50. In fact γ_{LV} is much larger than γ_{SL}, so the capillary force is indeed dominant in humid environments where the Young-Laplace and Kelvin equations hold.

Bibliography

Adamson, A.W., 1990. Physical chemistry of surfaces. Wiley, New York.

Agrawal, D.C., Raj, R., 1989. Measurement of the ultimate shear-strength of a metal ceramic interface. Acta Metallurgica 37 (4), 1265-1270.

Agrawal, D.C., Raj, R., 1990. Ultimate shear strengths of copper silica and nickel silica interfaces. Materials Science and Engineering a-Structural Materials Properties Microstructure and Processing 126, 125-131.

Autumn, K., Sitti, M., Liang, Y.C.A., Peattie, A.M., Hansen, W.R., Sponberg, S., Kenny, T.W., Fearing, R., Israelachvili, J.N., Full, R.J., 2002. Evidence for van der waals adhesion in gecko setae. Proceedings of the National Academy of Sciences of the United States of America 99 (19), 12252-12256.

Barsoum, M., 1997. Fundamentals of ceramics. McGraw-Hill, New Youk.

Barthel, E., 1998. On the description of the adhesive contact of spheres with arbitrary interaction potentials. Journal of Colloid and Interface Science 200 (1), 7-18.

Bergström, L., 1997. Hamaker constants of inorganic materials. Advances in Colloid and Interface Science 70, 125-169.

Betzig, E., Finn, P.L., Weiner, J.S., 1992. Combined shear force and near-field scanning optical microscopy. Applied Physics Letters 60 (20), 2484-2486.

Binnig, G., Quate, C.F., Gerber, C., 1986. Atomic force microscope. Physical Review Letters 56 (9), 930-933.

Binning, G., Rohrer, H., Gerber, C., Weibel, E., 1982. Surface studies by scanning tunneling microscopy. Physical Review Letters 49 (1), 57-61.

Boucher, E.A., Kent, H.J., 1977. Capillary phenomena .3. Properties of rotationally symmetric fluid bodies with one asymptote-holms. Proceedings of the Royal Society of London Series a-Mathematical Physical and Engineering Sciences 356 (1684), 61-75.

Bourque, H., Leblanc, R.M., 1995. Electrochemical fabrication of scanning-tunneling-microscopy tips without an electronic shutoff control. Review of Scientific Instruments 66 (3), 2695-2697.

Bowden, F.P., Tabor, D., 1950. The friction and lubrication of solids. Oxford.

Bradley, R.S., 1932. The cohesive force between solid surfaces and the surface energy of solids. The Philosophical Magazine 13, 853-862.

Brenner, S.S., 1956. Tensile strength of whiskers. Journal of Applied Physics 27, 1484-1490.

Brown, L., Xu, D., Ravi-Chandar, K., Satapathy, S., 2007. Coefficient of friction measurement in the presence of high current density. IEEE Transactions on Magnetics 43 (1), 334-337.

Bryant, P.J., Kim, H.S., Zheng, Y.C., Yang, R., 1987. Technique for shaping scanning tunneling microscope tips. Review of Scientific Instruments 58 (6), 1115-1115.

Budakian, R., Putterman, S.J., 2002. Time scales for cold welding and the origins of stick-slip friction. Physical Review B 65 (23), 235429.

Burns, A.R., Houston, J.E., Carpick, R.W., Michalske, T.A., 1999. Molecular level friction as revealed with a novel scanning probe. Langmuir 15 (8), 2922-2930.

Butt, H.J., 2006. Physics and chemistry of interfaces. Wiley-VCH, Weinheim.

Butt, H.J., Wang, D.N., Hansma, P.K., Kuhlbrandt, W., 1991. Effect of surface-roughness of carbon support films on high-resolution electron-diffraction of 2-dimensional protein crystals. Ultramicroscopy 36 (4), 307-318.

Cain, R.G., Biggs, S., Page, N.W., 2000. Force calibration in lateral force microscopy. Journal of Colloid and Interface Science 227 (1), 55-65.

Carpick, R.W., Agrait, N., Ogletree, D.F., Salmeron, M., 1996. Variation of the interfacial shear strength and adhesion of a nanometer-sized contact. Langmuir 12 (13), 3334-3340.

Carpick, R.W., Ogletree, D.F., Salmeron, M., 1997. Lateral stiffness: A new nanomechanical measurement for the determination of shear strengths with friction force microscopy. Applied Physics Letters 70 (12), 1548-1550.

Carpick, R.W., Ogletree, D.F., Salmeron, M., 1999. A general equation for fitting contact area and friction vs load measurements. Journal of Colloid and Interface Science 211 (2), 395-400.

Carpick, R.W., Salmeron, M., 1997. Scratching the surface: Fundamental investigations of tribology with atomic force microscopy. Chemical Reviews 97 (4), 1163-1194.

Chen, Y.F., Wei, X., Huang, J.L., 1989. A simple new technique for preparing stm tips. Journal of Physics E-Scientific Instruments 22 (7), 455-457.

Chernyak, Y.B., Leonov, A.I., 1986. On the theory of the adhesive friction of elastomers. Wear 108 (2), 105-138.

Christenson, H.K., 1985. Capillary condensation in systems of immiscible liquids. Journal of Colloid and Interface Science 104 (1), 234-249.

Christenson, H.K., 1988. Adhesion between surfaces in undersaturated vapors - a reexamination of the influence of meniscus curvature and surface forces. Journal of Colloid and Interface Science 121 (1), 170-178.

Cieplak, M., Smith, E.D., Robbins, M.O., 1994. Molecular-origins of friction - the force on adsorbed layers. Science 265 (5176), 1209-1212.

Cleaver, J.A.S., Tyrrell, J.W.G., 2004. The infulence of relatvie humidity on particle adhesion- a review of previous work and the anomalous behavior of soda-lime glass. KONA 22, 9.

Cleveland, J.P., Manne, S., Bocek, D., Hansma, P.K., 1993. A nondestructive method for determining the spring constant of cantilevers for scanning force microscopy. Review of Scientific Instruments 64 (2), 403-405.

Crow, D.R., 1988. Principles and applications of electrochemistry. Chapman & Hall, New York.

Daly, C., Krim, J., 1996. Sliding friction of solid xenon monolayers and bilayers on ag(111). Physical Review Letters 76 (5), 803-806.

Derjaguin, B.V., Muller, V.M., Toporov, Y.P., 1975. Effect of contact deformations on adhesion of particles. Journal of Colloid and Interface Science 53 (2), 314-326.

Dorofeyev, I., Fuchs, H., Wenning, G., Gotsmann, B., 1999. Brownian motion of microscopic solids under the action of fluctuating electromagnetic fields. Physical Review Letters 83 (12), 2402-2405.

Dowson, D., 1979. History of tribology. Longman, London.

Drelich, J., Tormoen, G.W., Beach, E.R., 2004. Determination of solid surface tension from particle-substrate pull-off forces measured with the atomic force microscope. Journal of Colloid and Interface Science 280 (2), 484-497.

Drew, M., 1999. Surfaces, interfaces and colloids. Wiley, New York.

Dugdale, D.S., 1960. Yielding of steel sheets containing slits. Journal of the Mechanics and Physics of Solids 8, 100-104.

Edwards, G.J., Pearce, P.R., 1978. Comparison of ac and dc electrochemical etching techniques for fabrication of tungsten whiskers. Journal of Physics D-Applied Physics 11 (5), 761-764.

Enachescu, M., van den Oetelaar, R.J.A., Carpick, R.W., Ogletree, D.F., Flipse, C.F.J., Salmeron, M., 1998. Atomic force microscopy study of an ideally hard contact: The diamond(111) tungsten carbide interface. Physical Review Letters 81 (9), 1877-1880.

Enachescu, M., van den Oetelaar, R.J.A., Carpick, R.W., Ogletree, D.F., Flipse, C.F.J., Salmeron, M., 1999. Observation of proportionality between friction and contact area at the nanometer scale. Tribology Letters 7 (2-3), 73-78.

Filippov, A.E., Klafter, J., Urbakh, M., 2004. Friction through dynamical formation and rupture of molecular bonds. Physical Review Letters 92 (13), 135503-135501.

Fisher, L.R., Israelachvili, J.N., 1981. Direct measurement of the effect of meniscus forces on adhesion - study of the applicability of macroscopic thermodynamics to microscopic liquid interfaces. Colloids and Surfaces 3 (4), 303-319.

Fogden, A., White, L.R., 1990. Contact elasticity in the presence of capillary condensation .1. The nonadhesive hertz problem. Journal of Colloid and Interface Science 138 (2), 414-430.

Fotino, M., 1992. Nanotips by reverse electrochemical etching. Applied Physics Letters 60 (23), 2935-2937.

Fotino, M., 1993. Tip sharpening by normal and reverse electrochemical etching. Review of Scientific Instruments 64 (1), 159-167.

Freud, B.B., Freud, H.Z., 1930. A theory of the ring method for the determination of surface tension. Journal of the American Chemical Society 52, 1772-1782.

Frink, L.J.D., van Swol, F., 1998. Solvation forces between rough surfaces. Journal of Chemical Physics 108 (13), 5588-5598.

Frisbie, C.D., Rozsnyai, L.F., Noy, A., Wrighton, M.S., Lieber, C.M., 1994. Functional-group imaging by chemical force microscopy. Science 265 (5181), 2071-2074.

Gnecco, E., Bennewitz, R., Gyalog, T., Meyer, E., 2001. Friction experiments on the nanometer scale. Journal of Physics: Condensed Matter 13 (31), R619-R642.

Green, C.P., Lioe, H., Cleveland, J.P., Proksch, R., Mulvaney, P., Sader, J.E., 2004. Normal and torsional spring constants of atomic force microscope cantilevers. Review of Scientific Instruments 75 (6), 1988-1996.

Green, J.B.D., McDermott, M.T., Porter, M.D., Siperko, L.M., 1995. Nanometer-scale mapping of chemically distinct domains at well-defined organic interfaces using frictional force microscopy. Journal of Physical Chemistry 99 (27), 10960-10965.

Greenwood, J.A., 1997. Adhesion of elastic spheres. Proceedings of the Royal Society of London Series a-Mathematical Physical and Engineering Sciences 453 (1961), 1277-1297.

Greenwood, J.A., Johnson, K.L., 1998. An alternative to the maugis model of adhesion between elastic spheres. Journal of Physics D-Applied Physics 31 (22), 3279-3290.

Hamaker, H.C., 1937. The london-van der waals attraction between spherical particles. Physica 4, 1058-1072.

He, G., Muser, M.H., Robbins, M.O., 1999. Adsorbed layers and the origin of static friction. Science 284 (5420), 1650-1652.

He, G., Robbins, M.O., 2001. Simulations of the static friction due to adsorbed molecules. Physical Review B 6403 (3).

Hertz, H., 1882. On the contact of elastic solids. J. Reine Angew. Math. 92, 156-171.

Hirano, M., Shinjo, K., Kaneko, R., Murata, Y., 1991. Anisotropy of frictional forces in muscovite mica. Physical Review Letters 67 (19), 2642-2645.

Hirano, M., Shinjo, K., Kaneko, R., Murata, Y., 1997. Observation of superlubricity by scanning tunneling microscopy. Physical Review Letters 78 (8), 1448-1451.

Hirsch, P.B., Howie, A., Nicholson, R.B., Pashley, D.W., Whelan, M.J., 1965. Electron microscopy of thin crystals. Butterworths, London.

Homola, A.M., Israelachvili, J.N., Gee, M.L., McGuiggan, P.M., 1989. Measurements of and relation between the adhesion and friction of 2 surfaces separated by molecularly thin liquid-films. Journal of Tribology-Transactions of the Asme 111 (4), 675-682.

Homola, A.M., Israelachvili, J.N., McGuiggan, P.M., Gee, M.L., 1990. Fundamental experimental studies in tribology - the transition from interfacial friction of undamaged molecularly smooth surfaces to normal friction with wear. Wear 136 (1), 65-83.

Horn, R.G., Israelachvili, J.N., Pribac, F., 1987. Measurement of the deformation and adhesion of solids in contact. Journal of Colloid and Interface Science 115 (2), 480-492.

Hughes, B.D., White, L.R., 1979. Soft contact problems in linear elasticity. Quarterly Journal of Mechanics and Applied Mathematics 32 (NOV), 445-471.

Huh, C., Scriven, L.E., 1969. Shapes of axisymmetric fluid interfaces of unbounded extent. Journal of Colloid and Interface Science 30, 323-337.

Hull, D., Bacon, D.J., 2001. Introduction to dislocations. Butterworth-Heinemann, Oxford.

Hurtado, J.A., Kim, K.S., 1999a. Scale effects in friction of single-asperity contacts. I. From concurrent slip to single-dislocation-assisted slip. Proceedings of the Royal Society of London Series a-Mathematical Physical and Engineering Sciences 455 (1989), 3363-3384.

Hurtado, J.A., Kim, K.S., 1999b. Scale effects in friction of single-asperity contacts. Ii. Multiple-dislocation-cooperated slip. Proceedings of the Royal Society of London Series a-Mathematical Physical and Engineering Sciences 455 (1989), 3385-3400.

Ibe, J.P., Bey, P.P., Brandow, S.L., Brizzolara, R.A., Burnham, N.A., Dilella, D.P., Lee, K.P., Marrian, C.R.K., Colton, R.J., 1990. On the electrochemical etching of tips for scanning tunneling microscopy. Journal of Vacuum Science & Technology a-Vacuum Surfaces and Films 8 (4), 3570-3575.

Israelachvili, J., 1992a. Interfacial forces. Journal of Vacuum Science & Technology a-Vacuum Surfaces and Films 10 (5), 2961-2971.

Israelachvili, J., Tabor, D., 1972. The measurement of van der waals dispersion forces in the range 1.5 to 130 nm Proceedings of the Royal Society of London Series a-Mathematical Physical and Engineering Sciences 331, 19-38.

Israelachvili, J., Wennerstrom, H., 1996. Role of hydration and water structure in biological and colloidal interactions. Nature 379 (6562), 219-225.

Israelachvili, J.N., 1992b. Intermolecular and surface forces. Academic, New York.

Israelachvili, J.N., Adams, G.E., 1978. Measurement of forces between 2 mica surfaces in aqueous-electrolyte solutions in range 0-100 nm. Journal of the Chemical Society, Faraday Transactions 74, 975-1001.

Israelachvili, J.N., McGuiggan, P.M., 1988. Forces between surfaces in liquids. Science 241 (4867), 795-800.

Israelachvili, J.N., McGuiggan, P.M., Homola, A.M., 1988. Dynamic properties of molecularly thin liquid-films. Science 240 (4849), 189-191.

Israelachvili, J.N., Pashley, R.M., 1983. Molecular layering of water at surfaces and origin of repulsive hydration forces. Nature 306 (5940), 249-250.

Johnson, K.L., 1997. Adhesion and friction between a smooth elastic spherical asperity and a plane surface. Proceedings of the Royal Society of London Series a-Mathematical Physical and Engineering Sciences 453 (1956), 163-179.

Johnson, K.L., Greenwood, J.A., 1997. An adhesion map for the contact of elastic spheres. Journal of Colloid and Interface Science 192 (2), 326-333.

Johnson, K.L., Kendall, K., Roberts, A.D., 1971. Surface energy and the contact of elastic solids. Proceedings of the Royal Society of London Series a-Mathematical Physical and Engineering Sciences 324, 301-313.

Johnson, K.L., Woodhouse, J., 1998. Stick-slip motion in the atomic force microscope. Tribology Letters 5 (2-3), 155-160.

Jones, R., Pollock, H.M., Cleaver, J.A.S., Hodges, C.S., 2002. Adhesion forces between glass and silicon surfaces in air studied by afm: Effects of relative humidity, particle size, roughness, and surface treatment. Langmuir 18 (21), 8045-8055.

Joyce, S.A., Houston, J.E., 1991. A new force sensor incorporating force-feedback control for interfacial force microscopy. Review of Scientific Instruments 62 (3), 710-715.

Kar, A.K., Gangopadhyay, S., Mathur, B.K., 2000. A reverse electrochemical floating-layer technique of spm tip preparation. Measurement Science & Technology 11 (10), 1426-1431.

Kelsey, G.S., 1977. Anodic-oxidation of tungsten in aqueous base. Journal of the Electrochemical Society 124 (6), 814-819.

Kim, H.I., Boiadjiev, V., Houston, J.E., Zhu, X.Y., Kiely, J.D., 2001. Tribological properties of self-assembled monolayers on au, siox and si surfaces. Tribology Letters 10 (1-2), 97-101.

Kim, H.I., Houston, J.E., 2000. Separating mechanical and chemical contributions to molecular-level friction. Journal of the American Chemical Society 122 (48), 12045-12046.

Kim, K.S., McMeeking, R.M., Johnson, K.L., 1998. Adhesion, slip, cohesive zones and energy fluxes for elastic spheres in contact. Journal of the Mechanics and Physics of Solids 46 (2), 243-266.

Krim, J., 1996. Friction at the atomic scale. Scientific American 275 (4), 74-80.

Krim, J., Solina, D.H., Chiarello, R., 1991. Nanotribology of a kr monolayer - a quartz-crystal microbalance study of atomic-scale friction. Physical Review Letters 66 (2), 181-184.

Krim, J., Widom, A., 1988. Damping of a crystal-oscillator by an adsorbed monolayer and its relation to interfacial viscosity. Physical Review B 38 (17), 12184-12189.

Kuehn, S., Loring, R.F., Marohn, J.A., 2006. Dielectric fluctuations and the origins of noncontact friction. Physical Review Letters 96 (17), 156103.

Lantz, M.A., Oshea, S.J., Welland, M.E., Johnson, K.L., 1997. Atomic-force-microscope study of contact area and friction on nbse2. Physical Review B 55 (16), 10776-10785.

Lassner, E., Schubert, W., 1999. Tungsten: Properties, chemistry, technology of the element, alloys, and chemical compounds. Springer, New York.

Leite, F.L., Riul, A., Herrmann, P.S.P., 2003. Mapping of adhesion forces on soil minerals in air and water by atomic force spectroscopy (afs). Journal of Adhesion Science and Technology 17 (16), 2141-2156.

Levin, Y., 2000. Interfacial tension of electrolyte solutions. Journal of Chemical Physics 113 (21), 9722-9726.

Liechti, K.M., Schnapp, S.T., Swadener, J.G., 1997. Contact angle and contact mechanics of a glass/epoxy interface. International Journal of Fracture 86 (4), 361-374.

Liu, A.W., Hu, X.T., Liu, W.H., Ji, G.J., 1997. An improved control technique for the electrochemical fabrication of scanning tunneling microscopy microtips. Review of Scientific Instruments 68 (10), 3811-3813.

Lowengrub, M., Sneddon, I.M., 1965. The distribution of stress in the vicinity of an external crack in an infinite elastic solid. International Journal of Engineering Science 3, 451-460.

Maderson, P.F.A., 1964. Keratinized epidermal derivatives as an aid to climbing in gekkonid lizards. Nature 203, 780-781.

Malotky, D.L., Chaudhury, M.K., 2001. Investigation of capillary forces using atomic force microscopy. Langmuir 17 (25), 7823-7829.

Marti, O., Colchero, J., Mlynek, J., 1990. Combined scanning force and friction microscopy of mica. Nanotechnology 1 (2), 141-144.

Martin, Y., Wickramasinghe, H.K., 1987. Magnetic imaging by force microscopy with 1000-a resolution. Applied Physics Letters 50 (20), 1455-1457.

Mate, C.M., McClelland, G.M., Erlandsson, R., Chiang, S., 1987. Atomic-scale friction of a tungsten tip on a graphite surface. Physical Review Letters 59 (17), 1942-1945.

Matsuoka, H., Fukui, S., 2002. Nanomeniscus forces in undersaturated vapors: Observable limit of macroscopic characteristics. Langmuir 18 (18), 6796-6801.

Maugis, D., 1992. Adhesion of spheres - the jkr-dmt transition using a dugdale model. Journal of Colloid and Interface Science 150 (1), 243-269.

Maugis, D., Gauthiermanuel, B., 1994. Jkr-dmt transition in the presence of a liquid meniscus. Journal of Adhesion Science and Technology 8 (11), 1311-1322.

McNeil, L.E., Grimsditch, M., 1993. Elastic-moduli of muscovite mica. Journal of Physics-Condensed Matter 5 (11), 1681-1690.

Medyanik, S.N., Liu, W.K., Sung, I.H., Carpick, R.W., 2006. Predictions and observations of multiple slip modes in atomic-scale friction. Physical Review Letters 97 (13), 136106.

Melmed, A.J., 1991. The art and science and other aspects of making sharp tips. Journal of Vacuum Science & Technology B 9 (2), 601-608.

Meyer, E., Luthi, R., Howald, L., Bammerlin, M., Guggisberg, M., Guntherodt, H.J., 1996. Site-specific friction force spectroscopy. Journal of Vacuum Science & Technology B 14 (2), 1285-1288.

Meyer, G., Amer, N.M., 1988. Novel optical approach to atomic force microscopy. Applied Physics Letters 53 (12), 1045-1047.

Meyer, G., Amer, N.M., 1990. Simultaneous measurement of lateral and normal forces with an optical-beam-deflection atomic force microscope. Applied Physics Letters 57 (20), 2089-2091.

Miranda, P.B., Xu, L., Shen, Y.R., Salmeron, M., 1998. Icelike water monolayer adsorbed on mica at room temperature. Physical Review Letters 81 (26), 5876-5879.

Mohilner, D.M., Beck, T.R., 1979. Thermodynamic theory of electrocapillarity for solid metal-electrodes. Journal of Physical Chemistry 83 (9), 1160-1166.

Muller, E.W., Tsong, T.T., 1969. Field ion microscopy principles and applications. Elsevier, New York.

Müller, V.M., Derjaguin, B.V., Toporov, Y.P., 1983a. On 2 methods of calculation of the force of sticking of an elastic sphere to a rigid plane. Colloids and Surfaces 7 (3), 251-259.

Müller, V.M., Yushchenko, V.S., Derjaguin, B.V., 1980. On the influence of molecular forces on the deformation of an elastic sphere and its sticking to a rigid plane. Journal of Colloid and Interface Science 77 (1), 91-101.

Müller, V.M., Yushchenko, V.S., Derjaguin, B.V., 1983b. General theoretical consideration of the influence of surface forces on contact deformations and the reciprocal adhesion of elastic spherical-particles. Journal of Colloid and Interface Science 92 (1), 92-101.

Noy, A., 2006. Chemical force microscopy of chemical and biological interactions. Surface and Interface Analysis 38 (11), 1429-1441.

Noy, A., Vezenov, D.V., Lieber, C.M., 1997. Chemical force microscopy. Annual Review of Materials Science 27, 381-421.

Ogletree, D.F., Carpick, R.W., Salmeron, M., 1996. Calibration of frictional forces in atomic force microscopy. Review of Scientific Instruments 67 (9), 3298-3306.

Overney, R.M., Meyer, E., Frommer, J., Brodbeck, D., Luthi, R., Howald, L., Guntherodt, H.J., Fujihira, M., Takano, H., Gotoh, Y., 1992. Friction measurements on phase-separated thin-films with a modified atomic force microscope. Nature 359 (6391), 133-135.

Pashley, M.D., 1984. Further consideration of the dmt model for elastic contact. Colloids and Surfaces 12 (1-2), 69-77.

Pauling, L., 1960. The nature of the chemical bond Cornell University Press, Ithaca.

Petrovic, J.J., 2003. Mechanical properties of ice and snow. Journal of Materials Science 38 (1), 1-6.

Pietrement, O., Troyon, M., 2000. General equations describing elastic indentation depth and normal contact stiffness versus load. Journal of Colloid and Interface Science 226 (1), 166-171.

Putman, C.A.J., Igarashi, V., Kaneko, R., 1995. Single-asperity friction in friction force microscopy - the composite-tip model. Applied Physics Letters 66 (23), 3221-3223.

Roth, A., 1976. Vacuum technology. North-Holland, Amsterdam.

Rubio, G., Agrait, N., Vieira, S., 1996. Atomic-sized metallic contacts: Mechanical properties and electronic transport. Physical Review Letters 76 (13), 2302-2305.

Sader, J.E., Chon, J.W.M., Mulvaney, P., 1999. Calibration of rectangular atomic force microscope cantilevers. Review of Scientific Instruments 70 (10), 3967-3969.

Scherge, M., Gorb, S.N., 2001. Biological micro and nanotriboligy. Springer, Berlin.

Schonenberger, C., Alvarado, S.F., 1990. Observation of single charge-carriers by force microscopy. Physical Review Letters 65 (25), 3162-3164.

Schwarz, U.D., Allers, W., Gensterblum, G., Wiesendanger, R., 1995. Low-load friction behavior of epitaxial c-60 monolayers under hertzian contact. Physical Review B 52 (20), 14976-14984.

Senden, T.J., Ducker, W.A., 1994. Experimental-determination of spring constants in atomic-force microscopy. Langmuir 10 (4), 1003-1004.

Singer, I.L., Pollock, H.M., 1992. Fundamentals of friction: Macroscopic and microscopic processes. Kluwer, Dordrecht.

Slade, P.G., 1999. Electrical contacts. Marcel Dekker, New York.

Socoliuc, A., Bennewitz, R., Gnecco, E., Meyer, E., 2004. Transition from stick-slip to continuous sliding in atomic friction: Entering a new regime of ultralow friction. Physical Review Letters 92 (13), Art. No. 134301.

Spagnoli, C., Loos, K., Ulman, A., Cowman, M.K., 2003. Imaging structured water and bound polysaccharide on mica surface at ambient temperature. Journal of the American Chemical Society 125 (23), 7124-7128.

Stipe, B.C., Mamin, H.J., Stowe, T.D., Kenny, T.W., Rugar, D., 2001. Noncontact friction and force fluctuations between closely spaced bodies. Physical Review Letters 8709 (9), art. no.-096801.

Sun, W.X., Shen, Z.X., Cheong, F.C., Yu, G.Y., Lim, K.Y., Lin, J.Y., 2002. Preparation of cantilevered w tips for atomic force microscopy and apertureless near-field scanning optical microscopy. Review of Scientific Instruments 73 (8), 2942-2947.

Tabor, D., 1977. Surface forces and surface interactions. Journal of Colloid and Interface Science 58 (1), 2-13.

Tabor, D., Winterton, R.H.S., 1969. The direct measurement of normal and retarded van der waals forces. Proceedings of the Royal Society of London Series a-Mathematical Physical and Engineering Sciences 312, 435-450.

Tegart, W.J.M., 1956. The electrolytic and chemical polishing of metals in research and industry. Pergamon, New York.

Tilley, R.J.D., 2004. Understanding solids: The science of materials. Wiley, New York.

Timoshenko, S.P., Goodier, J.N., 1986. Theory of elasticity. McGraw-Hill, New York.

Tomassone, M.S., Sokoloff, J.B., Widom, A., Krim, J., 1997. Dominance of phonon friction for a xenon film an a silver (111) surface. Physical Review Letters 79 (24), 4798-4801.

Tomlinson, G.A., 1929. A molecular theory of friction. The Philosophical Magazine 7, 905-939.

Uchic, M.D., Dimiduk, D.M., Florando, J.N., Nix, W.D., 2004. Sample dimensions influence strength and crystal plasticity. Science 305 (5686), 986-989.

Visser, J., 1972. On hamaker constants: A comparison between hamaker constants and lifshitz - van der waals constants. Advances in Colloid and Interface Science 3, 331-335.

Wang, M., 2005. Nanoindentation of thin organic films and self-assembled monolayers. ASE/EM. The University of Texas at Austin, Austin.

Wang, M., Xu, D., Ravi-Chandar, K., Liechti, K.M., 2007. On the development of a mesoscale friction tester. Experimental Mechanics 47 (1), 123-131.

Warren, A., Nylund, A., Olefjord, I., 1996. Oxidation of tungsten and tungsten carbide in dry and humid atmospheres. International Journal of Refractory Metals & Hard Materials 14 (5-6), 345-353.

Watts, E.T., Krim, J., Widom, A., 1990. Experimental-observation of interfacial slippage at the boundary of molecularly thin-films with gold substrates. Physical Review B 41 (6), 3466-3472.

Xu, D., Liechti, K.M., Ravi-Chandar, K., 2007a. On the modified tabor parameter for the jkr-dmt transition in the presence of a liquid meniscus. Journal of Colloid and Interface Science, DOI: 10.1016/j.jcis.2007.1007.1048.

Xu, D., Ravi-Chandar, K., Liechti, K.M., 2007b. Mesoscale scanning probe tips with sub-nanometer rms roughness. Review of Scientific Instruments, 073707.

Yao, H.M., Gao, H.J., 2006. Optimal shapes for adhesive binding between two elastic bodies. Journal of Colloid and Interface Science 298 (2), 564-572.

Yu, H., Shrotriya, P., Wang, J., Kim, K.S., 2003. Dislocation nucleation and segregation in nano-scale contact of stepped surfaces. MRS Proceedings 795 (U7.9), U7.9.

Zamora, R.R.M., Sanchez, C.M., Freire, F.L., Prioli, R., 2004. Influence of capillary condensation of water in nanoscale friction. Physica Status Solidi a-Applied Research 201 (5), 850-856.

Zhang, R., Ivey, D.G., 1996. Preparation of sharp polycrystalline tungsten tips for scanning tunneling microscopy imaging. Journal of Vacuum Science & Technology B 14 (1), 1-10.

Zhong, W., Tomanek, D., 1990. 1st-principles theory of atomic-scale friction. Physical Review Letters 64 (25), 3054-3057.

Zimon, A.D., 1982. Adhesion of dust and powder. Consultants Bureau, New York.

Vita

Dewei Xu was born in Yidu, Hubei Province of China, on February 27, 1974, the son of Xinquan Xu and Jiazhen Xiang. After completing high school at No. 1 High School at Yidu in 1993, Dewei Xu entered Beijing University of Aeronautics and Astronautics (BUAA), China, where he received the degree of Bachelor in Aircraft Design in 1997. He pursued the doctor degree of philosophy in Aircraft Design/;Applied Mechanics at BUAA in the following three years. During this period, he became dissatisfied and resigned in 2000. Dewei Xu entered the Graduate School of The University of Texas at Austin in 2001 and he married to Mei Wu in 2003 who studied at BUAA during his graduate study.

Permanent address: 186 Qingjiang Road

Yidu, Hubei443300
China

This dissertation was typed by the author.